Eindhoven University of Technology

MASTER

Whispering gallery modes in nanowire solar cells

Nieuwdorp, Joep

Award date:
2021

Link to publication

EINDHOVEN UNIVERSITY OF TECHNOLOGY

MASTER THESIS

Whispering gallery modes in nanowire solar cells

Author:
J. NIEUWDORP

Supervisor:
dr. J. E. M. HAVERKORT
K. KORZUN, MSc

*A thesis submitted in fulfillment of the requirements
for the degree of Master of Science*

in the

Advanced Nanomaterials & Devices (AND) Group
of the Department of Applied Physics

TU/e

April 27, 2021

EINDHOVEN UNIVERSITY OF TECHNOLOGY

Abstract

Whispering gallery modes in nanowire solar cells

by J. NIEUWDORP

Optimization of the external radiative efficiency towards unity must be realized to obtain a high open-circuit voltage and reach the Shockley-Queisser limit of a solar cell. This optimization is achieved in two ways: by enhancing the internal radiative efficiency and by increasing the photon escape probability. Tapered nanowire structures host coupled whispering gallery modes and Fabry-Perot modes that show enhanced photoluminescent emission. Using finite-difference-time-domain simulations, these modes are characterized for a variety of straight and tapered nanowire geometries. The modes show high Q-factors (>1000) independent of NW length and locally enhance the spontaneous emission through their Purcell effect. Moreover, inversely tapered nanowires show an enhanced photon escape probability with respect to normally tapered nanowires. An experimental characterization of the photoluminescence of these structures remains inconclusive. Whispering gallery modes should be investigated further with an investigation of their behaviour in a single tapered nanowire or strictly at low temperatures. This thesis can be consulted for a fundamental understanding of the contribution of these modes to the increase of the external radiative efficiency in nanowire solar cells.

Acknowledgements

I remember that about a year ago, I was planning on spending a season at the University of Basel to fulfill my external traineeship under the supervision of prof. Ilaria Zardo. The consequences of a global pandemic demanded a change of plans, and looking back on the past year now, I am glad with the way it has turned out. Some of the brightest people I know have made it that way, and here I would like to thank them.

First and foremost, I would like to thank my daily supervisor, Ksenia. Your guidance, counsel and patience have been indispensable factors during my work. Always finding time to adress my inquiries, you have gone above and beyond to provide the supervision that I desired during my graduation project. I will never forget meeting you in person for the first time four months after we had started working together.

I would like to thank my other daily supervisor, dr. Jos Haverkort. Your infallible knowledge in the field of solar cells, photonics and (American) politics have impressed me since the day we started working together and our lively discussions (nearly) always left me feeling enlightened.

I would like to thank the rest of the photovoltaics project group, Emanuele, Ilya and Philemon. I'm very grateful to your contributions to weekly discussions and the overall help with the experimental work that I performed.

I would like to thank the rest of the AND group. The weekly meetings made me feel part of a vibrant community of young and promising physicists. Especially the weekly online social meetings on Friday made each AND group member feel like a friend rather than a colleague.

I would like to thank prof. dr. Erik Bakkers for allowing me to work on a graduation project in his group. Thanks to your quick and friendly responses that kickstarted this project, I could continue my studies smoothly and seamlessly. You always find a way to make me smile.

I would like to thank the defence committee members next to my supervisors, dr. Shuxia Tao and prof. dr. Andrea Fiore. Thank you for spending your valuable time to read and critically assess my graduation work and for participating in my defence.

Lastly, I would like to thank my girlfriend, friends and family for keeping me sane throughout the entire year. On occasion, I felt distressed and exhausted because of the combination of workload and the consequences of the global pandemic and it is you who kept me going and comforted me when needed. I am forever grateful to them, and the events of this year have clearly shown me their importance and significance to me.

Contents

List of Abbreviations

CMT	coupled mode theory
CW	continuous wave
DOS	density of states
EBL	electron-beam lithography
FDTD	finite-difference-time-domain
FF	fill factor
FP	Fabry-Perot
FSR	free spectral range
FWHM	full width at half-maximum
GaAs	gallium arsenide
GW	gigawatts
HE	hybrid electric
ICP	inductively coupled plasma
InP	indium phosphide
LDOS	local density of states
MOVPE	metalorganic vapour-phase epitaxy
NC	nanocone
NRIE	nitride reactive ion etching
NW	nanowire
PDMS	polydimethylsiloxane
PECVD	plasma-enhanced chemical vapour deposition
PL	photoluminescence
PML	perfectly matched layer
PMMA	polymethylmethacrylate
PSO	particle swarm optimization
PV	photovoltaic
SEM	scanning electron microscopy
Si	silicon
SRH	Shockley-Read-Hall
TE	transverse electric
TEM	transverse electromagnetic
TIR	total internal reflection
TM	transverse magnetic
WGM	whispering gallery mode

Chapter 1

Introduction

In this section, the motivation for this thesis is introduced and the underlying physical concepts and structures are explained. Then the contents of the chapters are briefly summarized.

1.1 Motivation for this research

Solar cells are indispensable in tackling the ever-increasing global energy demand. Between 1992 and 2018, the worldwide growth in photovoltaic (PV) technologies has been close to exponential, with promise to continue.[1] This is shown in figure 1.1 In 2018, the global cumulative installed PV capacity reached approximately 512 gigawatts (GW), of which 180 GW (35%) is gained from utility-scale plants, which amounts to approximately 3% of global electricity demand.[2] This percentage seems very small, but as we have learned from a year and a half battling a global pandemic, exponential growth is potent.[3]
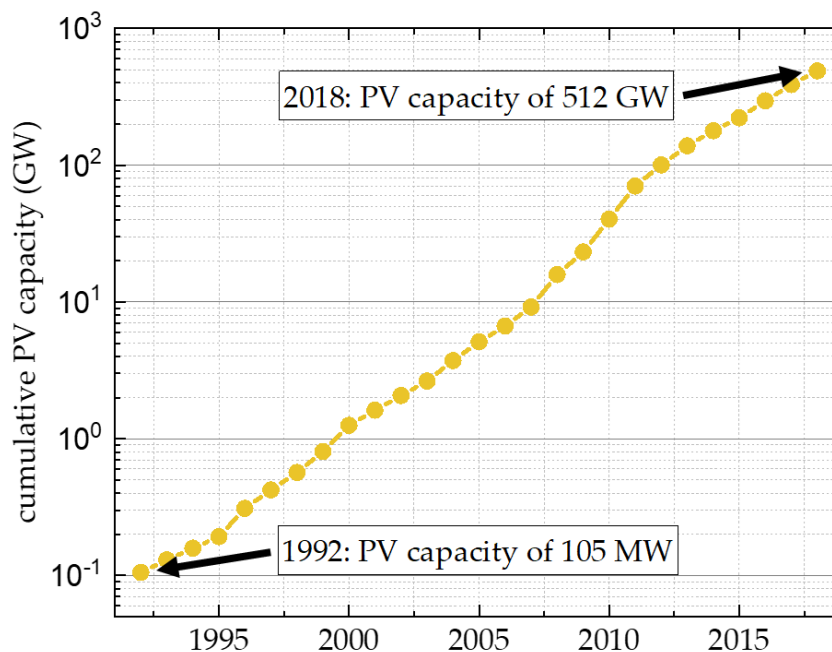

FIGURE 1.1: The worldwide cumulative PV capacity (measured in total amount of gigawatts, GW) from 1992 to 2018.[2]

Silicon solar cells have been the dominant driving force in photovoltaic technology for the past several decades due to the relative abundance and environmentally friendly nature of silicon.[4] In 2018, approximately 90% of solar cells were made from silicon, dominating the global PV market.[5] Unfortunately, the efficiency of the photovoltaic energy conversion from solar energy to electrical energy is limited by several thermodynamic processes, leading to a maximum power conversion efficiency of approximately 27% for these cells.[4–6] The maximum power conversion of a solar cell is closely related to its fill factor, short-circuit current and open-circuit voltage.[7] Although a great portion of research is focused on increasing the short-circuit current, the open-circuit voltage is often not discussed in detail.[8,9] In this thesis, we focus on optimizing the open-circuit voltage.

Both the concept of open-circuit voltage as well as the factors affecting the energy conversion efficiency have been explained in detail in a renowned paper by William Shockley and Hans Queisser in 1961.[10] Shockley and Queisser determined that a solar cell, assuming typical sunlight conditions, has a maximum power conversion efficiency of 33.7%. In this Shockley-Queisser limit, the solar cell is lossless and all solar radiation is converted into external radiation. To reach the Shockley-Queisser limit and achieve a high open-circuit voltage, the external radiative efficiency must be optimized.[9] Recently a lot of progress has been made in the field of nanowire solar cells which show promise for enhanced external radiative efficiencies.[9,11–13] Nanowire solar cells are a result of nanophotonic engineering on solar cells, enabling geometries that exhibit a multitude of photonic properties that are superior to their planar, bulk counterparts.[14–16]

In this thesis, we study the influence of whispering gallery modes on the external radiative efficiency. Whispering gallery modes are guided modes inside cylindrical or spherical resonators that propagate close to and along the structure walls.[17] They are modes which simultaneously exhibit a high Q-factor as well as a low mode volume V_m, featuring both significant temporal confinement as well as strong spatial confinement inside NWs. Our interest into these modes was sparked by a paper released by Schmitt *et al.*[18] and was further strengthened by research done by Yang *et al.*[13] Schmitt *et al.* report strongly enhanced photoluminescence from a tapered NW, which shows a 200-fold enhancement of band-to-band luminescence compared to a straight NW, which they claim is caused by leaky whispering gallery modes.[18] The modes are characterized by high Q-factors ($\approx$ 1300) and low mode volumes ($0.2 < (\lambda/n)^3 < 4$). The Purcell factor F_p of these modes, which is a measure for the enhancement of spontaneous emission and scales as $F_p \propto Q/V_m$, can explain the enhanced luminescence of these tapered structures with respect to their straight counterparts. This enhanced luminescence is an indication of an increase in the external radiative efficiency and is therefore interesting for photovoltaic applications.

On top of this, Seo *et al.* mention that negatively tapered nanowires (where the diameter increases with height) are even more suitable than positively tapered wires (where the diameter decreases with height) for a high emission from whispering gallery modes.[19] They mention that in these negatively tapered nanowires, the combined formation of a whispering gallery mode within the NW and a Fabry-Perot mode between this whispering gallery mode and the top facet is responsible for enhanced emission, shown in figure 1.2. This way, a high Q-factor whispering gallery mode causes a Purcell enhancement at a certain circumference, which results in a local enhanced spontaneous emission that travels to the top facet through a low Q-factor Fabry-Perot mode to be emitted from the top facet.
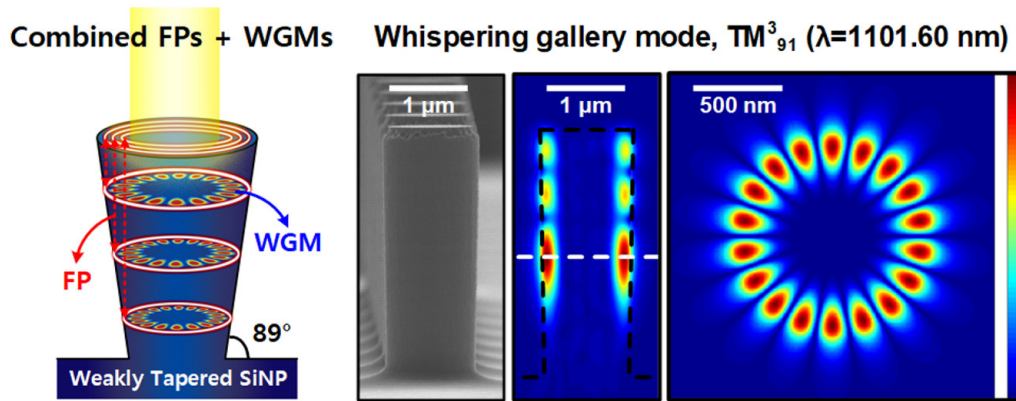
FIGURE 1.2: The combined mode formation between a whispering gallery mode and a Fabry-Perot mode. Next to that, a scanning electron microscope image of the negatively tapered nanowire, and simulated electric field distributions of the whispering gallery mode hosted in the structure.[19]

We perform finite-difference-time-domain simulations using Lumerical to characterize the behaviour of whispering gallery modes in nanowires. Many photonic properties such as the Q-factor, Purcell factor and the spontaneous emission factor β can be calculated using these simulations. Furthermore, we fabricate InP tapered nanowire arrays using a top-down etch approach for a characterization of the photoluminescence. Since it is not possible to produce negatively tapered nanowires with this method, the samples are covered in the transparent polymer PDMS to be extracted from the substrate. This PDMS transfer of the nanowires is a procedure well documented and well researched by Standing *et al.*[20] and has proven successful for the re-orientation of nanowire arrays in previous researches.[21–25]

1.2 Scope of this thesis

In this thesis, whispering gallery modes and their Purcell enhancement are studied to fundamentally understand the possibilities to enhance the external radiative efficiency of nanowire solar cells. This optimization of the enhanced radiative efficiency brings us one step closer to reaching, or even breaking, the Shockley-Queisser limit.

This thesis is composed of 6 chapters and 2 appendices. In Chapter 2, we introduce the theoretical background relevant to the work that is discussed in this thesis. In Chapter 3, the numerical and experimental methods that are used in this thesis are discussed. In Chapter 4, we investigate the results of the numerical simulations. In Chapter 5, the experimental results of the nanowire fabrication and photoluminescence measurements are discussed. In Chapter 6, the work is concluded and an outlook to future research is given. The two appendices describe in detail concepts and procedures that are used throughout this work.

Chapter 2

Theoretical background

In this section, an overview of the underlying theory of this thesis is given. The fundamental theory of ideal solar cells is shortly explained, after which we zoom in on the theory of realistic solar cells under open-circuit conditions. Next, the additional theory of nanowire solar cells is explained, and lastly, the concept of optical modes in these structures is described.

2.1 Fundamentals of the solar cell

A solar cell is a device that converts light energy into electrical energy in a photovoltaic energy conversion.[26] The energy conversion consists of the absorption of light (photons) producing electron-hole pairs in a semiconductor material followed by charge carrier separation. The absorption of light and production of electron-hole pairs is mainly determined by the semiconductor material properties, whereas the charge carrier separation is commonly accomplished by introducing a *p-n* junction in the material. A schematic overview of the composition of a solar cell and the photovoltaic processes is shown in figure 2.1.
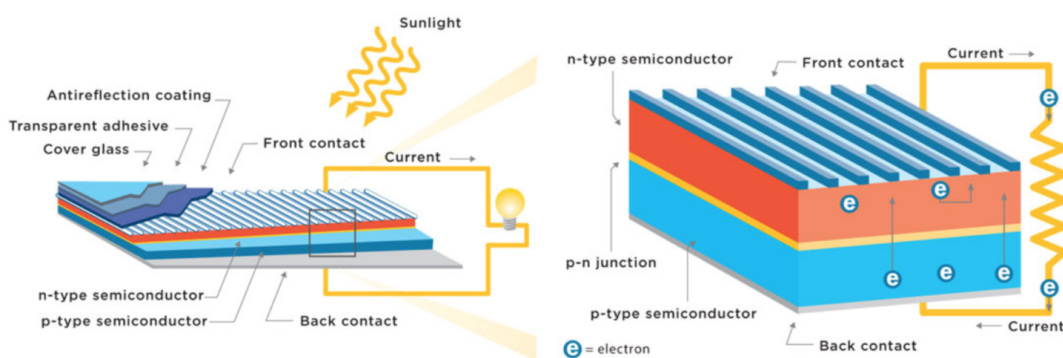

FIGURE 2.1: A solar cell consists of many layers, depicted on the left, each playing an important role in the energy conversion process. After the absorption of incident sunlight, electron-hole pairs are generated in the *p-n* junction, depicted on the right, which are then separated and guided to the contacts to produce a photocurrent.[27]

2.1.1 Semiconductor materials

Semiconductors are used for many applications in electronics and photonics because of their tunable material properties. For photovoltaic devices, the most important material properties are the bandgap properties (e.g. direct or indirect bandgap, bandgap energies and the resulting absorption coefficients) and the minority carrier diffusion length.[28,29]

In theory, both direct bandgap semiconductors (such as GaAs, InP and CdTe) as well as indirect bandgap semiconductors (such as Si, Ge and GaP) could be used in solar cells. Direct bandgap materials seem most appropriate because they exhibit strong optical transitions between the valence band and conduction band. These strong optical transitions ensure that photons have a high probability of being absorbed over a short distance. Direct bandgap solar cells therefore can be much thinner than indirect bandgap cells, saving material costs and space.

However, direct bandgap semiconductors like GaAs also have very short minority carrier diffusion lengths (ranging between 0.1 and 10 µm, depending on doping concentration).[30,31] This length is defined as the average distance a minority carrier can travel before recombining: for the p-type region and the n-type region the minority carriers are electrons and holes respectively. A short minority carrier diffusion length indicates that valuable charge carriers recombine over a short length, where their absorbed energy is lost. Silicon solar cells require a much thicker active layer to compensate for their low inherent absorption due to weak optical transitions but have large minority carrier diffusion lengths (ranging between 100 and 500 µm, depending on doping concentration).[32] This means that in silicon cells, charge carriers can cover a large distance without recombining. For the design of a solar cell, one must therefore take into account the ratio between the cell thickness and the minority carrier diffusion length.

2.1.2 Recombinations in semiconductors

Once a photon is absorbed by a semiconductor, an electron-hole pair is generated. For a solar cell, the carriers are ideally attracted to opposite ends of a *p-n* junction in order to harness the absorbed energy. However, they can also recombine before this happens, converting their energy in a number of ways. We distinguish two types of processes: radiative recombinations and nonradiative recombinations.

Electron-hole pair recombinations that emit a photon are called radiative recombinations. The process of recombination and emission of a photon is called photoluminescence (PL). In general, PL is a measure of radiative recombinations in a material.[33] Often, the electron-hole pair has dissipated energy between its creation and recombination so the re-emitted photon will have less energy than the photon that initially generated the electron-hole pair. Electron-hole pair recombinations that do not emit a photon are called nonradiative recombinations. Examples are Auger recombinations and recombinations at defects in the material such as surface recombinations and Shockley-Read-Hall (SRH) recombinations.[34] These involve processes where the electron-hole pair energy is transmitted to other charge carriers, defects or in the form of heat. A short overview with the most dominant recombinations is shown in figure 2.2. In indirect bandgap semiconductors, the probability of nonradiative recombination dominates that of radiative recombination by several orders of magnitude. In section 2.2.3 we will discuss the quantitative impact of radiative and nonradiative recombinations on the overall efficiency of a solar cell.
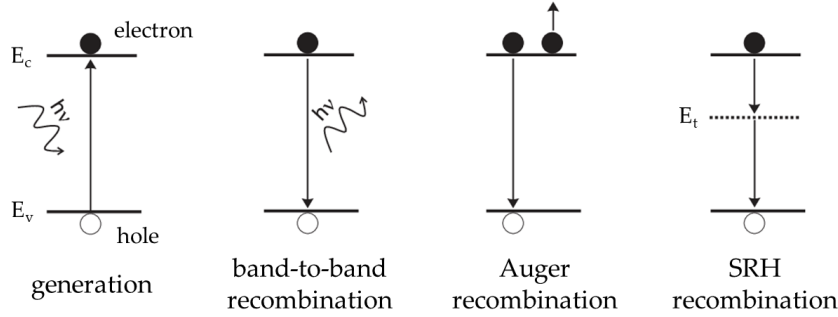
FIGURE 2.2: A schematic overview of an electron-hole pair gener-
ation and three types of recombinations: band-to-band (radiative),
Auger and Shockley-Read-Hall (nonradiative). E_c and E_v indicate the
conduction and valence bands and E_t is the energy of a trap state.

2.1.3 The ideal *p-n* junction solar cell

When light is incident on an ideal *p-n* junction without an external bias voltage,
each absorbed photon creates an electron and a hole. When these carriers diffuse to
the junction, the built-in electric field of the junction separates them at the energy
barrier. The separation of the carriers produces a forward voltage across the barrier:
forward, because the electric field of the photoexcited carriers is opposite to the built-
in field of the junction. The appearance of a forward voltage across an illuminated
p-n junction is called the photovoltaic effect.[33] Based on this effect, an illuminated
junction can deliver power to an external circuit. Large area *p-n* junctions of silicon
are already commonly used as solar panels to convert solar photons to electrical
energy.

The current generated by the photons, the photocurrent I_L, produces a voltage drop
across any resistive load connected to the *p-n* junction, which forward-biases the *p-n*
junction.[35] The resulting forward-bias voltage produces a forward-bias current I_F.
The net *p-n* junction current, in the reverse-biased direction, is

$$I = I_L - I_F = I_L - I_S \left[\exp \left(\frac{eV}{kT} \right) - 1 \right], \tag{2.1}$$

where the ideal diode equation has been used: V is the forward-bias voltage and I_S is
the dark saturation current. The ideal diode equation is plotted in figure 2.3. As the
diode becomes forward biased, the magnitude of the electric field in the space charge
region decreases but does not go to zero or change direction. The photocurrent I_L
is always in the reverse-biased direction and therefore the net solar cell current I is
always in the reverse-biased direction.

Two limiting cases are of interest which ultimately define a solar cell's performance
(which will be justified in section 2.1.4). The first one is the short-circuit condition,
which occurs when the resistance of the connected resistive load $R = 0$ so that $V = 0$.
The current in this case is referred to as the short-circuit current, where
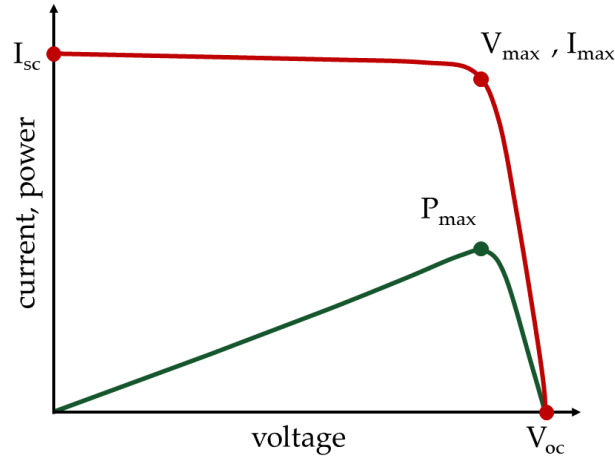
$$I = I_{sc} = I_L. \tag{2.2}$$

FIGURE 2.3: The characteristic IV-curve of an ideal *p-n* junction solar
cell in red. In green, the electrical power generated by the solar cell
as a function of its voltage. The open-circuit voltage V_{oc}, short-circuit
current I_{sc} and maximum power parameters are indicated.

The second limiting case is the open-circuit condition and occurs when the connected resistive load $R \to \infty$ so that $I = 0$. The net current is zero and the photogenerated voltage is the open-circuit voltage. The photocurrent I_L is exactly balanced by the forward-biased junction current, so we have

$$I = 0 = I_L - I_S \left[\exp \left(\frac{eV}{kT} \right) - 1 \right]. \tag{2.3}$$

We can then determine the open-circuit voltage V_{oc} as

$$V_{oc} = V_t \ln \left(1 + \frac{I_L}{I_S} \right), \tag{2.4}$$

where $V_t = \frac{kT}{e}$ is the thermal voltage (approximately $25.9 \, \text{mV}$ at $300 \, \text{K}$). Keep in mind that equation 2.4 is derived from the ideal diode equation rather than from a realistic solar cell junction with additional losses and recombination processes. We will find more elaborate expressions for the open-circuit voltage V_{oc} in section 2.2. In that section, the external radiative efficiency η_{ext}^{PL} will be introduced, which indicates how dominant radiative recombinations are in the solar cell.

It is instructive to note that for a lossless cell where radiative recombinations are dominant, the cell is said to be in the radiative limit and the dark saturation current I_S is determined strictly by the cell's black body recombination current.[9] The black body radiation from a solar cell at room temperature (300 K) accounts for 7% of the available incoming energy but cannot be captured by the cell.[10] Any inefficiencies and losses in the cell increase the cell temperature when it is placed in sunlight. As the temperature of the cells increases, the amount of black body radiation increases with it until an equilibrium is reached. The efficiency is ultimately limited by an equilibrium temperature, where cells operate at lower efficiencies than at their room temperature. This is the first indication that it is important to optimize the fraction of radiative recombinations with respect to nonradiative recombinations in the cell.

2.1.4 Power conversion efficiency

When a current is generated inside the solar cell, any resistive load can be attached to it to receive power. The power delivered to the load is

$$P = I \cdot V = I_L \cdot V - I_S \left[\exp \left(\frac{eV}{kT} \right) - 1 \right] \cdot V. \tag{2.5}$$

We may find the current and voltage which will deliver the maximum power P_{max} to the resistive load by setting the derivative to zero, or $dP/dV = 0$. Using equation 2.5, we find

$$\frac{dP}{dV} = 0 = I_L - I_S \left[\exp \left(\frac{eV_{max}}{kT} \right) - 1 \right] - I_S V_{max} \frac{e}{kT} \exp \left(\frac{eV_{max}}{kT} \right), \tag{2.6}$$

where V_{max} is the voltage at P_{max}. Equation 2.6 can be rewritten in the form

$$\left(1 + \frac{V_{max}}{V_t} \right) \exp \left(\frac{V_{max}}{V_t} \right) = 1 + \frac{I_L}{I_S}. \tag{2.7}$$

The value of V_{max} is determined by trial and error, which is then used to find I_{max}. Figure 2.3 shows the maximum power point as P_{max}. The power conversion efficiency η of a solar cell is defined as the ratio of output electrical power to incident optical power. For the maximum power output we can write

$$\eta = \frac{P_{max}}{P_{in}} \cdot 100\% = \frac{I_{max} \cdot V_{max}}{P_{in}} \cdot 100\% = FF \cdot \frac{I_{sc} \cdot V_{oc}}{P_{in}} \cdot 100\%, \tag{2.8}$$

where we introduce the fill factor (FF), defined as

$$FF = \frac{I_{max} \cdot V_{max}}{I_{sc} \cdot V_{oc}}. \tag{2.9}$$

The FF is a measure of the realizable power from a solar cell. Typically, the FF of a solar cell is between 0.7 and 0.85.[6,7] As we can see from figure 2.3, the maximum possible current and the maximum possible voltage in the solar cell are I_{sc} and V_{oc} respectively. We can see from equation 2.8 that the power conversion efficiency of a cell is proportional to the short-circuit current I_{sc} and open-circuit voltage V_{oc} of that cell for a given FF. Therefore, even though a solar cell operates neither at I_{sc} nor at V_{oc} under working conditions, those two quantities properly define the cell's values P_{max} and η.[26,36] It is important to mention that a cell in the radiative limit has the highest maximum power P_{max}.

The conventional *p-n* junction solar cell has a single semiconductor bandgap energy E_g. When the cell is exposed to the solar spectrum, a photon with energy less than E_g will not affect on the electrical output power of the solar cell. On the other hand, a photon with energy greater than E_g will contribute to the solar cell output power, but the fraction of photon energy that is greater than E_g will eventually only be dissipated as heat. Due to the shape of the solar spectrum, a silicon *p-n* junction solar cell has a maximum conversion efficiency η of approximately 32%.[4,10] Non-ideal factors will typically lower the conversion efficiency.[6] These losses are accounted for in the model of a real solar cell, which is treated in the next section.

2.2   Real solar cells at open-circuit voltage

A solar cell with the highest power conversion efficiency is desirable, as the energy extraction per unit area of the solar cell is then optimal. From equation 2.8, we may conclude that an increase in the product of the short-circuit current I_{sc} and the open-circuit voltage V_{oc} results in a higher maximum output power P_{max} (considering the FF remains the same).[26] Most of the literature concerning the pursuit for a higher maximum output power is focused on increasing the short-circuit current I_{sc} while not discussing the open-circuit voltage V_{oc} in much detail. Often, there is a trade-off to be made between those two parameters; increasing the one generally decreases the other.[37] This thesis mainly concerns the optimization of the solar cell operating at the open-circuit voltage.

2.2.1   The ideality factor

In the derivation of the simple diode equation (equation 2.1), the assumption is made that all recombinations occur via band-to-band transitions or via traps in the bulk areas from the device (i.e. not explicitly in the *p-n* junction). However, in a real solar cell, the recombination processes are not limited only by minority carriers.[38] Deriving the ideal diode equation by considering the number of carriers needed during single recombination processes yields

$$I = I_L - I_F = I_L - I_S \left[\exp\left(\frac{eV}{nkT} \right) - 1 \right], \tag{2.10}$$

where *n* is the ideality factor. It is an important parameter that can be used to decide whether a *p-n* junction device heavily or poorly resembles the ideal case.[39] For the ideal diode $n = 1$,[38,40] but if other recombination processes dominate such as recombinations in the depletion region[41–43] or Auger recombinations,[44] $n \neq 1$ because multiple charge carriers are involved in a single recombination. If we determine the open-circuit voltage V_{oc} using this correction we obtain

$$V_{oc} = \frac{nkT}{e} \ln\left(1 + \frac{I_L}{I_S} \right). \tag{2.11}$$

If we compare this to equation 2.4, it seems as if the V_{oc} for a non-ideal diode is higher than the V_{oc} of an ideal diode. However, this is not the case because the ideality factor *n* also increases the dark saturation current I_S. The net effect is a combination of the increase in voltage for increasing *n* and the decrease in voltage for increasing I_S. Typically, I_S is the more significant factor and the result is a reduction in the open-circuit voltage V_{oc}.[39]

As an alternative to account for multiple recombination processes in the solar cell, researchers have used a three-diode model to describe its behaviour.[45–48] The model, which is visualised in figure 2.4, contains three separate diodes with distinct ideality factors n_1, n_2 and n_3, and adds a series resistance R_s and shunt resistance R_{sh} to the ideal diode model. The resulting expression for the current provided to a load is

$$I = I_L - I_{S1}\left[\exp\left(\frac{e(V + I \cdot R_s)}{n_1 kT}\right) - 1\right] - I_{S2}\left[\exp\left(\frac{e(V + I \cdot R_s)}{n_2 kT}\right) - 1\right]$$
$$- I_{S3}\left[\exp\left(\frac{e(V + I \cdot R_s)}{n_3 kT}\right) - 1\right] - \frac{V + I \cdot R_s}{R_{sh}}, \quad (2.12)$$

where I_{S1}, I_{S2} and I_{S3} are the dark saturation currents of the three diodes (in the opposite direction of the diode currents I_1, I_2 and I_3). Each of the three diodes corresponds to one recombination process. For example, diode 1 represents the current due to diffusion and recombination in the quasi-neutral regions of the emitter and bulk parts with $n_1 = 1$, diode 2 represents the current due to recombination in the depletion region with $n_2 = 2$ and diode 3 is different for each research purpose. Usually it is attributed to recombinations in defect regions and grain sites,[46–48] but some researchers leave it open to interpretation.[45] All of them agree that a two-diode model, which had been proposed before, showed to be insufficient in describing the solar cell recombination behaviour properly.
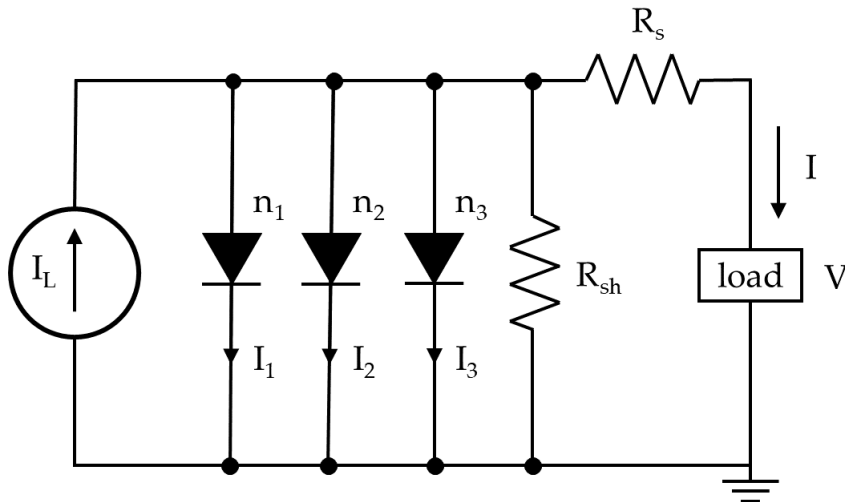
FIGURE 2.4: The three-diode model for a solar cell. Under illumination, the solar cell generates a photocurrent I_L which powers a load. All recombination processes are accounted for using three separate diodes with distinct ideality factors.

Estimation of all of the parameters of equation 2.12 is required for modeling the performance of the photovoltaic system. Since this is an equation with 9 unknown parameters which would require tremendous computing power using ordinary analytical methods, an inventive method called Particle Swarm Optimization (PSO) is used to solve it.[49] Khanna *et al.* explain this method well:[46] "PSO simulates the behaviour of a flock of birds. When a flock of birds searches for food, no bird knows where the food is, but all the birds know the distance to the food. Initially, all the birds move with random velocities and positions, but after a while, based on their own flying experience and the experience of the other birds, all the birds follow the bird that is nearest to the food." Performing a PSO requires a well-defined set of initial conditions and boundary values to work well.

A proposal for the three-diode model could be to assign the third diode to purely radiative recombinations with ideality factor $n_3 = 1$. The other two diodes could account for SRH recombination in the quasi-neutral regions with n_1 and for SRH recombination in the depletion region with n_2. Then, in the radiative limit, the two diodes that account for nonradiative recombinations will vanish, and only the diode with ideality factor $n_3 = 1$ will remain. In that case, as mentioned before, the dark saturation current I_{S3} is determined strictly by the cell's black body recombination current, minimizing losses.[9]

2.2.2 Fundamental limits to the power conversion efficiency

As mentioned in section 2.1.3 a solar cell produces a zero net current at the open-circuit voltage V_{oc}. If we consider a solar cell that hosts radiative recombination processes only, this means that every photoexcited electron-hole pair must eventually recombine to emit a photon again (as discussed in section 2.1.2). This process is well studied and can be understood by considering the detailed balance limit of a solar cell which was developed by Shockley and Queisser.[10,50] They defined a limit where the maximum theoretical power conversion efficiency of a single *p-n* junction solar cell – and with it, the maximum open-circuit voltage V_{oc} – is obtained, where the only loss mechanism is radiative recombination. This is called the Shockley-Queisser limit, and it states that a solar cell, assuming typical sunlight conditions, has a maximum power conversion efficiency of 33.7%.

This efficiency is the result of several physical processes whose losses can hardly be avoided. The first loss is due to solar photons with a photon energy below the semiconductor bandgap. They cannot be absorbed and do not contribute to the generation of electron-hole pairs. The second loss is a thermalization loss of photoinduced carriers by photons with a photon energy above the bandgap. The excess energy they submit to the material can only be converted into heat. A third loss is a result of the Carnot efficiency. The surface of the Sun (6000 K) and the surface of the solar cell (300 K) have different temperatures which induce this thermodynamic loss. Fourth, the semiconductor material tends to lose energy through the emission of photons at the maximum power point of the solar cell. In figure 2.5, the losses are visualized as a function of the semiconductor material bandgap.

One loss has not been discussed yet, because it is a physical process we may be able to control. It is the étendue loss, or light entropy loss. At the Shockley-Queisser limit, the solar cell is converting a nearly parallel beam of photons (assuming direct solar radiation) into a randomized emission pattern (across a 4π solid angle) when it is operating at open-circuit conditions. The entropic increase in the directivity of the photons causes a voltage loss,[52] which could be avoided by sending all emitted photons back towards the sun in an equally narrow collimated beam. If this is realized, the so-called ultimate limit is approached. The light propagation in an ultimate limit cell should be strictly reversible within the spectral region of the emission spectrum, thereby avoiding any increase in photon entropy. The open-circuit voltages at the Shockley-Queisser limit V_{oc}^{SQ} and at the ultimate limit V_{oc}^{ultimate} are related by

$$V_{oc}^{rad} = V_{oc}^{\text{ultimate}} - \left| \frac{kT}{e} \ln\left(\frac{\varepsilon_{\text{in}}}{\varepsilon_{\text{out}}}\right) \right|, \qquad (2.13)$$
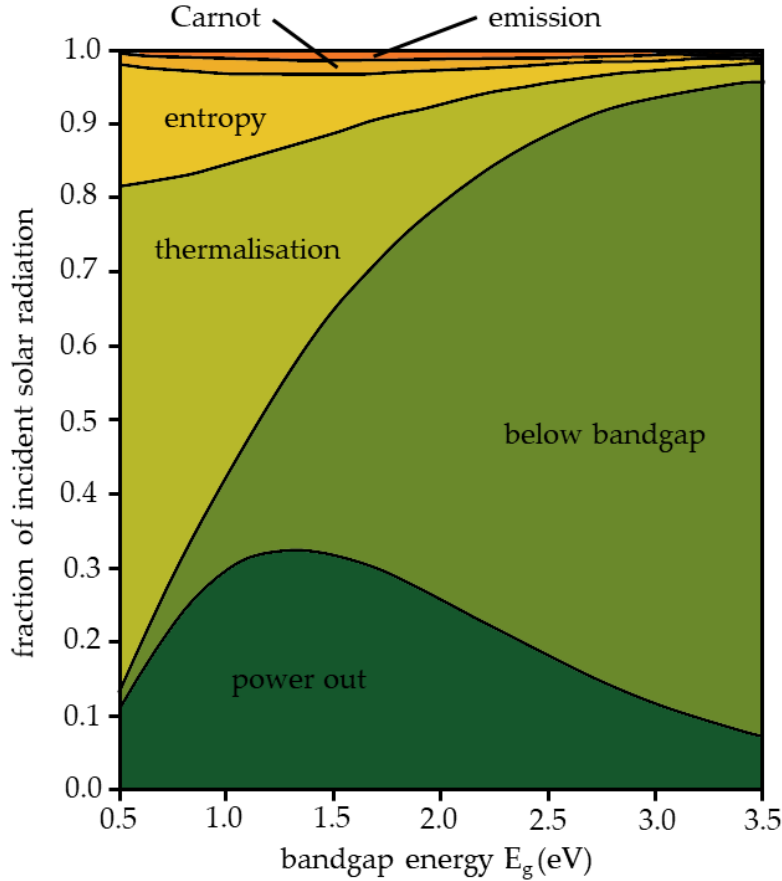
FIGURE 2.5: The fraction of incident solar radiation that will maximally be converted into outcoupled electrical power. All incident solar radiation is accounted for, illustrating why different intrinsic loss mechanisms lead to a fundamental limiting efficiency.[51]

where the open-circuit voltage at the radiative limit $V_{oc}^{rad} = V_{oc}^{SQ}$ for a lossless cell and where the fraction $\varepsilon_{in}/\varepsilon_{out}$ is the ratio between input and output étendues; for the Schockley-Queisser limit $\varepsilon_{in} = 6.85 \cdot 10^{-5}$ and $\varepsilon_{out} = 4\pi$.[9] The ultimate limit allows a power conversion efficiency of maximally 46.7%. In the ultimate limit, these two étendues are equal: a perfectly collimated beam with a finite spectral range is re-emitted with the exact same étendue within that same spectral range and there is no net gain in entropy in this process.[10]

2.2.3 The external radiative efficiency

In the previous section, we considered a solar cell that only hosts radiative recombination processes. A real, non-ideal solar cell unfortunately also hosts nonradiative processes, which generate heat. The ratio between the rates of external radiative recombination processes and the sum of external radiative and all nonradiative recombination processes is called the external radiative efficiency. It is given by[29]

$$\eta_{ext}^{PL} = \frac{R_{ext}}{R_{ext} + R_{nonrad}}. \tag{2.14}$$

The external radiative efficiency η_{ext}^{PL} is a direct figure of merit for the ability of a solar cell to approach the radiative limit V_{oc}^{rad}. The nonradiative recombination processes reduce the external radiative efficiency and through it, the maximum value of the open-circuit voltage V_{oc}.[53] A second loss term is added to equation 2.13, yielding[54]

$$V_{oc} = V_{oc}^{\text{ultimate}} - \left| \frac{kT}{e} \ln\left(\frac{\varepsilon_{\text{in}}}{\varepsilon_{\text{out}}}\right) \right| - \left| \frac{kT}{e} \ln(\eta_{ext}^{PL}) \right| = V_{oc}^{rad} - \left| \frac{kT}{e} \ln(\eta_{ext}^{PL}) \right|. \qquad (2.15)$$

If nonradiative recombination processes are nearly absent, $R_{nonrad} \approx 0$, we find $\eta_{ext}^{PL} \approx 1$, resulting in the open-circuit voltage that approaches the radiative limit. Therefore, the radiative limit can be approached by optimization of η_{ext}^{PL} towards unity.[9] The external radiative efficiency η_{ext}^{PL} can be separated into two parts. It is dependant on the internal radiative efficiency η_{int}^{PL}, which gives the fraction of internal recombination events that is radiative (similarly to equation 2.14), and the averaged photon escape probability $\overline{P_{esc}}$, which is the probability that an internally emitted photon escapes the solar cell. The relation between these variables is governed by[55]

$$\eta_{ext}^{PL} = \frac{\eta_{int}^{PL}\overline{P_{esc}}}{1 - \eta_{int}^{PL}(1 - \overline{P_{esc}})}, \qquad (2.16)$$

where $(1 - \overline{P_{esc}})$ is the averaged probability that an internally emitted photon never escapes the solar cell and is eventually absorbed. For low values of η_{int}^{PL} we can approximate using[56]

$$\eta_{ext}^{PL} \approx \eta_{int}^{PL}\overline{P_{esc}} = \frac{R_{rad}}{R_{rad} + R_{nonrad}}\overline{P_{esc}}, \qquad (2.17)$$

where R_{rad} and R_{nonrad} are all internal radiative and nonradiative recombination processes respectively. It becomes clear that in order to optimize the external radiative efficiency, two parameters need to be optimized. On the one hand, we need to optimize the radiative recombination rate R_{rad} with respect to the nonradiative recombination rate R_{nonrad}. This is mentioned throughout this chapter because when the radiative recombination rate is dominant, the saturation current I_S of the solar cell is minimal which optimizes the open-circuit voltage V_{oc}. On the other hand, we need to optimize the averaged photon escape probability $\overline{P_{esc}}$ (as visualized in figure 2.6). Counterintuitively, maximizing the rate and probability at which the solar cell *emits* photons in open-circuit conditions results in a higher maximum output power.[29,57] This thesis studies the application of nanowires to pursue these goals.

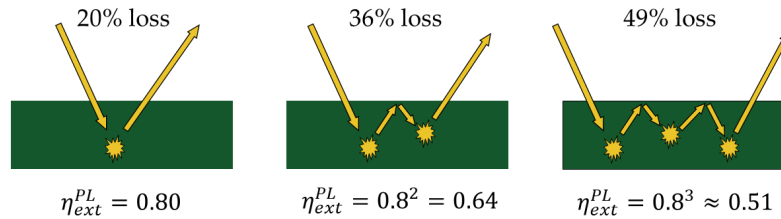$$\eta_{ext}^{PL} = 0.80 \qquad \eta_{ext}^{PL} = 0.8^2 = 0.64 \qquad \eta_{ext}^{PL} = 0.8^3 \approx 0.51$$

FIGURE 2.6: Scheme indicating the necessity of a high photon escape probability. For a cell with $\eta_{int}^{PL} = 0.80$, each internal reflection and re-absorption-re-emission event adds to a loss to η_{ext}^{PL}.[9]

2.3 Fundamentals of the nanowire solar cell

The nanowire (NW) solar cell is a direct result of the application of nanophotonic engineering on solar cells. Instead of a planar surface, NW solar cells contain an active layer of semiconductor NWs at the top surface. Before we investigate what alterations NWs impose with respect to planar solar cell characteristics, it is important to understand the physical significance of NWs in general.[14]

Firstly, the diameter puts the radial dimension of these structures at or below the characteristic length scale of fundamental solid-state phenomena: the wavelength of light in the visible spectrum, charge carrier diffusion lengths and others.[15,16] Many physical properties of semiconductors are altered within these wires too. The two-dimensional confinement of optical modes gives NWs unique properties that are typically not observed in their corresponding bulk material.

Second, the NW geometries allow for strain relaxation or application in the radial direction, which offers a wide range of options in choosing lattice-mismatched materials for heterostructures[58,59] or even in the tuning of bandgap energies.[60–62] This combination opens up a large pallet of material combinations and bandgaps that efficiently match the spectrum of incident light in the active region of a NW array.

Third, the wide range of parameters that can be altered relatively easily provides an even wider range of technological applications. The one unconstrained dimension can direct the transport of charge carriers and photons. This control over energy transport through nanophotonic engineering makes NWs ideal structures for the design and development of advanced solid-state devices. Moreover, NW lengthscales generally allow the use of both bottom-up and top-down fabrication processes. As a result, NWs provide a complete platform for researchers to study transport phenomena. The general NW array setup and its most significant design parameters are shown in figure 2.7. Especially the ratio between the diameter and length D/L can be chosen as a design parameter for a NW array.[11,19,25,56,63–67]
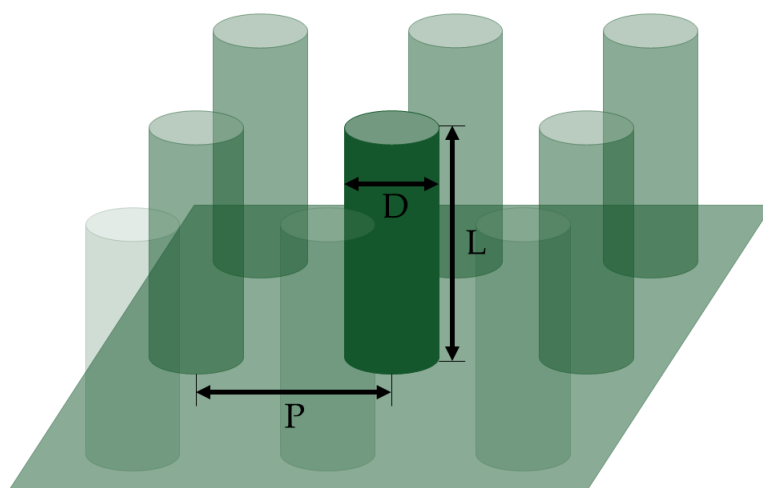

FIGURE 2.7: Overview of a square NW array, defined by the NW diameter D, NW length L and intermittent NW distance, or pitch, P.

2.3.1   Benefits of the nanowire solar cell

Currently, the highest recorded power conversion efficiencies for planar single junction solar cells are 29.1% $\pm$ 0.6% (thin film GaAs),[68] 26.7% $\pm$ 0.5% (crystalline Si)[69] and 24.2% $\pm$ 0.5% (crystalline InP)[70] whereas the record for a nanowire solar cell is 17.8% (InP).[71] However, NW solar cells have several advantages over planar solar cells that could put them on top regarding these efficiencies. In this section, a summary of the most potent advantages of the NW geometries is given. Ultimately, through the optimization of these advantages, the radiative limit could be reached for NW solar cells.

Reduced reflection

Solar cells need to absorb light across a broad spectral region that coincides as much as possible with the solar spectrum. There are two categories of absorption losses in real solar cells: reflection losses and transmission losses. For planar solar cells, it is difficult to reduce the surface reflection. Any reflection at an interface arises from a difference in refractive index between the two media at the interface, where the reflectivity R under normal incidence is given by[36]

$$R = \left(\frac{n_1 - n_2}{n_1 + n_2} \right)^2, \tag{2.18}$$

where n_1 and n_2 are the refractive indices of the two media at the interface. Most inorganic semiconductor materials will reflect between 10% and 50% of sunlight because of their high refractive indices compared to air.[8] One common way to reduce reflection is the introduction of an anti-reflection coating. Ideally, the refractive index of the coating is the geometric mean of the refractive indices of the semiconductor material and air, i.e. the square root of their product.[72,73] However, this solution is optimized for a single wavelength at normal incidence which disregards the rest of the spectrum, resulting in considerable reflection losses across most of the spectrum anyway. Multiple layers of anti-reflection coatings may broaden the spectral range that reaches the solar cell, but ideally, you would have a coating with a continuously graded refractive index.[74] A continuous grading allows for the least amount of reflection because at each increment in the coating, the change in refractive index is smooth instead of stepwise.

A NW solar cell introduces an artificial change in the refractive index through a concept called the effective medium approach for the refractive index.[8,75] Using this approach, the NW layer and its surrounding medium are simplified into a single layer with a weighted refractive index, as visualized in figure 2.8. Accordingly, this layer exhibits an effective refractive index that is in between that of the NW material and the surrounding medium. As previously mentioned and by inspection of equation 2.18 this is desirable, especially if the change in refractive index is continuously gradual. For that reason, tapered NWs (nanocones, NCs) could be even more suitable for reducing the reflection losses, because they alter this effective index gradually in the vertical direction.[8] For both NWs and NCs across a range of semiconductor materials, numerous studies have reported great decreases in the reflection with respect to planar surfaces.[11,65–67,75,76]
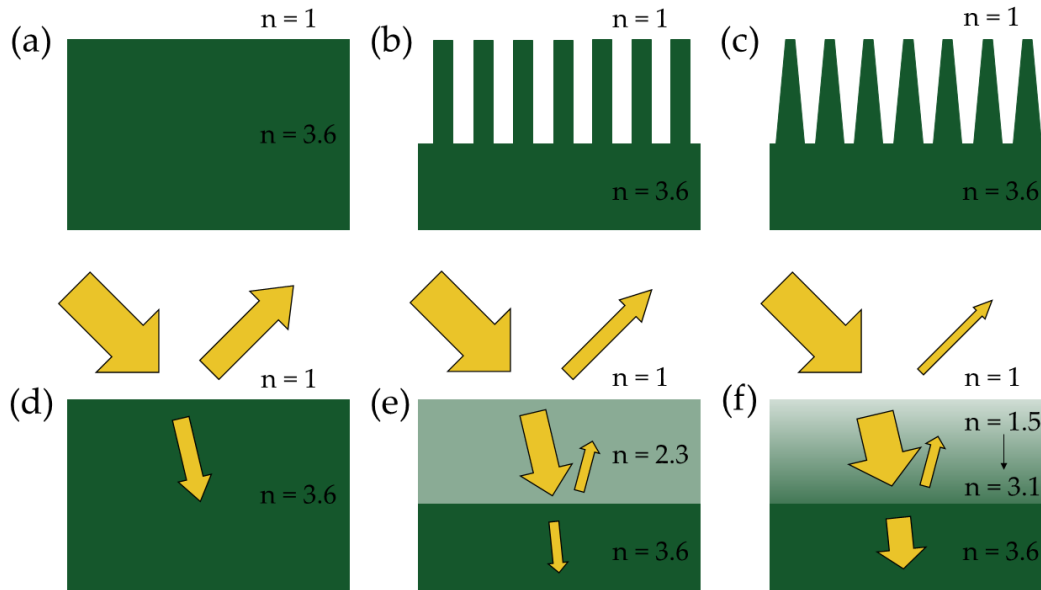
FIGURE 2.8: Visualisation of the effective medium approach for the refractive index for different cells with a material refractive index $n = 3.6$ in air $n = 1$. (a), (b) and (c) are cross-sections of a planar cell, NW cell and NC cell respectively. (d), (e) and (f) visualize their effective refractive index profiles and reflections from incident light.

Light trapping

Absorption losses are also caused by transmission losses. These losses occur for cells that are either too thin to interact with incoming light or cells that do not apply sufficient light trapping to quench all the incoming photons. The application of light trapping has been covered in many studies[12,53,77,78] and mainly constitutes an enhancement of the photon path length inside the active region of the solar cell. This implies that light bounces back and forth within the cell many times, indicating light confinement.

Using a statistical ray optics approach, the maximum light trapping absorption enhancement is defined by thermodynamics to be $4n^2$, where n is the refractive index of the material.[79] The only assumptions made in that approach are that the medium does not absorb light and that the light is propagating in random directions inside the structure. Those two assumptions however consider a random array of NWs; a periodic NW array should be able to exceed this limit using optical resonances along the NW diameter to enhance the absorption.[12,80,81] Photons are trapped in these resonant modes until they are absorbed. One resonant mode common for cylindrical structures and at the point of interest in this thesis will be elaborated upon in section 2.4.2.

Reduced active volume

One of the unique interactions of light with NWs is called the optical antenna effect. This effect can be analysed following an approach originally taken by Gustav Mie.[82] Because NW dimensions are on the order of the wavelength of the incident light, models based on geometrical optics no longer describe their scattering properties correctly. Mie initially found solutions to Maxwell's equations concerning light scattering from subwavelength particles, and over the years more elaborate models have been developed.[83,84] These models predict that certain NW geometries display an optically resonant response (similar to an antenna), enhancing their absorption.[12,85] The models described that as a consequence of the optical antenna effect, NWs exhibit absorption cross-sections that are larger than their geometrical cross-sections.[86,87]

An array of NWs can be designed in such a way that the absorption cross-sections of individual NWs are overlapping, which is depicted in figure 2.9. In that case, the NW solar cell would feature light absorption probability similar to a planar solar cell covering an identical area while the active volume of the NW solar cell is 5-10 times as small.[81] Besides saving material costs in this way, the reduced active volume results in a lower number of nonradiative recombinations internally in the volume. According to equation 2.17 this improves the internal radiative efficiency η_{int}^{PL} and through it, the maximum open-circuit voltage V_{oc}.

not enough overlap   good overlap   too much overlap
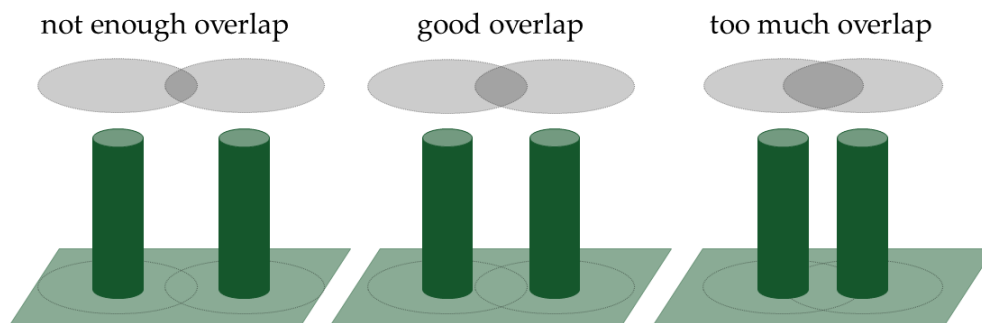
FIGURE 2.9: Schematic overview of NWs on a substrate with their absorption cross-sections in grey. If the wires are too far apart, they do not cover an absorption area equal to a planar cell of equivalent area. If the wires are too close, the beneficial reduction in active volume of NWs is too small.

Better outcoupling of light

For a real solar cell, it is important that the photon escape probability P_{esc} is as high as possible to obtain a large open-circuit voltage V_{oc}, which we have seen directly from equations 2.16 and 2.17. An internally emitted photon can either escape the solar cell or remain in the solar cell to be reabsorbed again, losing energy in the form of heat in the process or engaging in other nonradiative recombination processes. This has already been visualised in figure 2.6, which shows a process called photon recycling.[88] For any material with a less-than-unity internal radiative efficiency η_{int}^{PL}, the re-absorption and re-emission of photons is disadvantageous and adds to a loss in the external radiative efficiency η_{ext}^{PL}. A high photon escape probability P_{esc} limits these losses.

In a planar cell with no anti-reflection coating, photoluminescence generally occurs isotropically. A large fraction of the emitted photons is totally internally reflected, resulting in an angle averaged photon escape probability $\overline{P_{esc}}$ which is proportional to the solid angle of the escape cone, which is equal to $\frac{1}{4n^2} \approx 2\%$ for planar InP, where n is the index of refraction.[56] From this we learn that photons do not easily escape a planar solar cell for most semiconductor materials. Moreover, comparing this escape probability, which scales as $\frac{1}{4n^2}$, with the aforementioned light trapping absorption enhancement, which scales as $4n^2$, is very insightful. It highlights that light trapping and photon extraction are often complementary: they emphasize each others qualities.[57] Photons with energies close to the bandgap energy need to be trapped as best as possible to be absorbed with high probability, while on the other hand, they need to be released as best as possible to be emitted with high probability.

The photon escape probability of a NW solar cell relies on the subtle outcoupling of the photons at the facets of the wires; the subtle expansion of the mode into the environment.[85,89] This concept can be understood best by considering a tapered nanowire, as investigated experimentally by Friedler *et al.*[85] Figure 2.10 summarizes their main results. Figure 2.10 (a) shows the facet reflection and transmission properties as a function of the normalized wire diameter D/λ. $T(\theta = \pi/2)$ represents the total fraction that is scattered upward. The transmission $T(\theta)$ is shown as a function of θ in figure 2.10 (b) for several values of D/λ. An interesting outcome of these calculations is that, as they decrease the diameter, the transmission dramatically increases (figure 2.10 (a)) and the beam divergence decreases (figure 2.10 (b)). This dual property is very important for engineering inverse tapers that efficiently couple light by adiabatically tapering the nanowire to a small diameter supporting a mode mostly in air. In such a structure, the effective refractive index gradually decreases, which minimizes back-reflections and reduces the beam divergence in air.
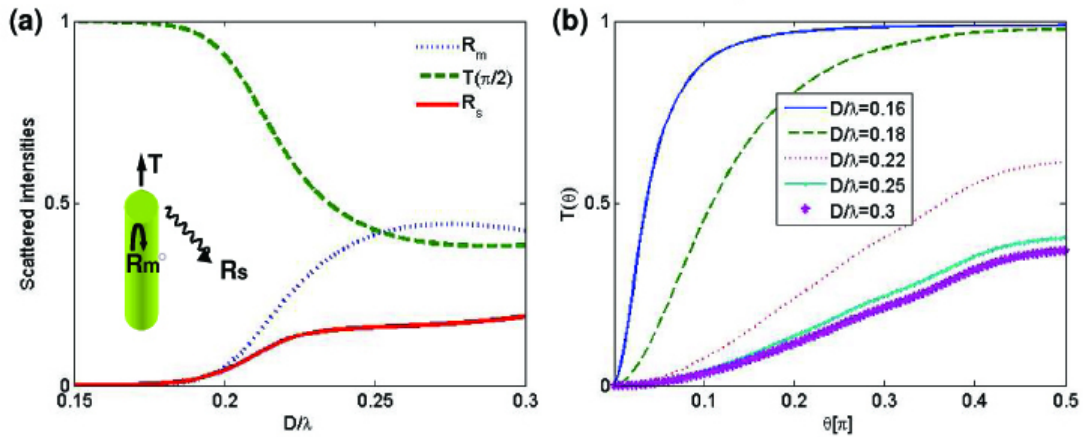
FIGURE 2.10: Optical properties of cleaved facets. (a) Dotted-blue curve: modal reflectivity R_m. Dashed-green curve: transmission $T(\theta)$ of the fundamental HE_{11} mode for a collection with a numerical aperture of 1. Solid-red curve: intensity R_s reflected into the radiation modes. All the coefficients are shown as a function of the normalized wire diameter D/λ. (b) $T(\theta)$ (in units of π) for different values of D/λ.[85]

In conclusion, their study showed that for a gradually tapered NW it is possible to adiabatically expand the fundamental HE_{11} mode of the NW into the surrounding air with a maximal efficiency of 95%. The adiabatic expansion in this context means that the fundamental mode is expanded gently out of the structure because of a slow variation of the mode effective refractive index as it propagates. This efficiency beats the restricted light outcoupling of planar solar cells by a large margin. Other studies suggest that a NW array could eventually increase the open-circuit voltage V_{oc} as a direct result of a high photon escape probability P_{esc},[25,56] although so far it has not been proven experimentally yet.

2.4   Optical modes in nanowires

Now that we know why NW solar cells should be investigated, it is necessary to introduce the theory of optical modes. In wave optics, the concept of modes is fundamental to understanding the behaviour of photons and it is well suited to describe most optical phenomena such as emission, absorption, coherence, propagation and dispersion.[90] Optical modes are solutions for the propagation of light in dielectric structures, where the number of photons in an optical mode describes the transport of energy through that mode.

Conceptually, modes are defined only by the properties of coherence and orthogonality: they are orthogonal solutions – eigenstates – of the wave equation and do not interfere with each other. Only the photons within one and the same mode with identical polarizations are coherent and are able to interfere. As a result, there should be no dissipation or exchange of energy between different modes. However, in most real systems there are perturbations such as impurities in the material that enable energy transfer between different modes. This interaction is called mode coupling, which is described by coupled mode theory (CMT), and it is important for applications in nanophotonics.

2.4.1   Waveguide modes

Unbound electromagnetic waves in free space or in an isotropic dielectric material can be described as a superposition of plane waves; they can be described by radiation modes where both the electric field and the magnetic field are perpendicular to the direction of propagation. These modes are called transverse electromagnetic (TEM) modes because they have both transverse electric and transverse magnetic fields.

However, when electromagnetic waves propagate through a waveguide (any anisotropic dielectric material), a physical structure imposes boundary conditions to the waves and they can no longer be described as a superposition of plane waves; rather, as a superposition of transverse modes. Unlike radiation modes, these guided modes can have electric or magnetic field components in the direction of propagation and are classified by that property. Waveguide modes can consist of transverse electric (TE) modes, transverse magnetic (TM) modes, hybrid electric (HE) modes, and the TEM modes mentioned earlier. TE and TM modes have magnetic and electric field components in the direction of propagation respectively, HE modes have both. The naming convention of Schmitt *et al.* to address different orders of modes for circular waveguides is adopted,[18] which is visualised in figure 2.11. The lowest order modes are called fundamental modes.
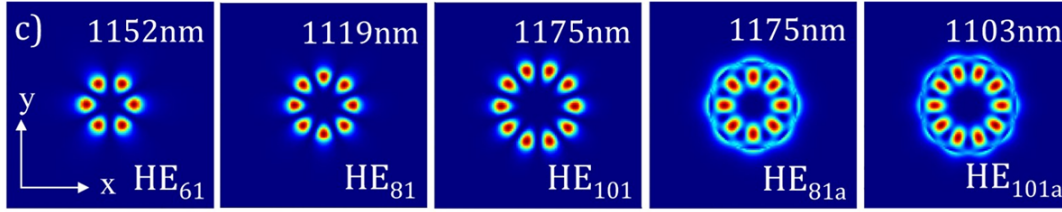
FIGURE 2.11: Characteristic (*x-y*)-cross-sections of the energy density for several cylindrical waveguide modes propagating through the waveguide. The naming of the modes is of the form HE$_{mn}$, where *m* and *n* correspond to the amount of nodes in the azimuthal and radial direction respectively.[18]

Inside a waveguide, photons propagate through optical modes which are characterized by their effective refractive index n_{eff}. The effective refractive index is best understood through comparison with the refractive index of a medium *n*. For plane waves in homogeneous transparent media, the refractive index *n* is used to quantify the increase of the vacuum wavenumber k_0 caused by the medium. The resulting wavenumber *k* is *n* times larger and the wavelength λ is *n* times smaller than it would be in vacuum. The effective refractive index n_{eff} has the analogous meaning for light propagation in a waveguide: we define the propagation constant β for some wavelength as the effective index n_{eff} times the vacuum wavenumber k_0:[91]

$$\beta = n_{\text{eff}} \, k_0 = n_{\text{eff}} \, \frac{2\pi}{\lambda_0}. \tag{2.19}$$

The propagation constant is the component of the waveguide's wavenumber *k* that is in the direction of propagation of the light, where $k = k_0 \, (n_{\text{bulk}}/n_{env})$ and n_{bulk} and n_{env} are the refractive indices of the waveguide and the environment respectively. The transverse component of the wavenumber is defined as κ, which is visualised geometrically in figure 2.12. Using the definition of *k*, we can also write

$$n_{\text{eff}} = \frac{\beta}{k_0} = \frac{\beta}{k} \, \frac{n_{\text{bulk}}}{n_{env}}. \tag{2.20}$$
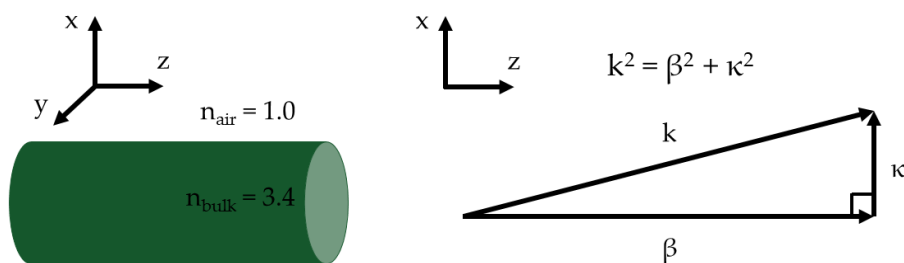

FIGURE 2.12: A geometrical representation of the propagation constant β and wavenumber *k* in a waveguide. For this waveguide, the environment is air ($n_{env} = 1$) and the material index of refraction $n = 3.4$ is typical for semiconductors around their bandgap energy.[92] κ is the transverse component of *k* w.r.t. the direction of propagation.

For a mode where the transverse component of the wavenumber κ is zero, we find from figure 2.12 that $\beta = k$ and from equation 2.20 that $n_{\text{eff}} = n_{\text{bulk}}/n_{env}$: the mode is completely confined in the waveguide because its propagation constant is aligned with its direction of propagation. Assuming that $n_{\text{bulk}} > n_{env}$, we say that a mode is leaky when $n_{\text{eff}} \leq n_{env}$. A leaky mode (also called tunneling mode) is a mode that is partly guided in a waveguide but simultaneously exhibits considerable propagation losses to the environment.[91] Unfortunately, the concept of leaky modes involves a number of mathematical subtleties, the understanding of which requires a detailed and careful study.[93,94] Even though leaky modes are not part of a complete orthogonal system of modes in a waveguide, they can still carry a respectable amount of a waveguide's optical power. Leaky modes can be quite useful both for qualitatively understanding the characteristics of certain waveguides and for doing light propagation simulations.[91]

From the energy densities and the definition of β it is possible to calculate the available guided modes for any given structure, resonator or cavity.[91] The quality of such a resonator, a cavity or of a single mode can be described by the dimensionless parameter Q, called the quality factor. This Q-factor can be defined in two ways: via energy storage or via resonance width. On the one hand, the Q-factor is the ratio between the energy stored and the energy dissipated per wave cycle. This intuitively means that a higher quality factor describes a cavity which confines energy better, or a mode which is confined stronger. It is calculated using[13,95]

$$Q = 2\pi \cdot \frac{\text{Energy stored}}{\text{Energy lost per optical cycle}} = \frac{2\pi\nu_0}{\kappa} = \frac{\omega_0}{\kappa} = \omega_0 \tau_{ph}. \qquad (2.21)$$

where ν_0 is the resonance frequency, ω_0 is the resonance angular frequency, κ is the resonance linewidth and $\tau_{ph} = \kappa^{-1}$ is the cavity/photon lifetime. Therefore, high Q-factor modes have narrow linewidths and long photon lifetimes (for a mode with $\nu_0 = 325$ THz and $Q = 10^3$, $\kappa = 2$ Thz and $\tau_{ph} = 490$ fs). Analogously, the Q-factor can directly be defined as the ratio of the resonance frequency ν_0 and the full width at half-maximum (FWHM) bandwidth $\delta\nu$ of the resonance frequency:

$$Q = \frac{\nu_0}{\delta\nu}. \qquad (2.22)$$

Generally speaking, there are four configurations that can trap photons efficiently, each relying on different confinement methods:[13] Fabry-Perot cavities, whispering gallery mode cavities, distributed feedback cavities and photonic crystal defect cavities (see figure 2.13). The Q-factor of such cavities allows comparison between these methods and gives a reliable parameter for improved light confinement.

Next to the quality factor, there is a different property of waveguide modes that allows for direct comparison between the setups visualised in figure 2.13. The mode volume V_m is the effective volume that a guided mode occupies, which is not necessarily equal to the cavity volume V. It is calculated using[96]

$$V_m = \frac{\int_V \epsilon(r)|E(r)|^2 \mathrm{d}V}{\max(\epsilon(r)|E(r)|^2)}, \qquad (2.23)$$
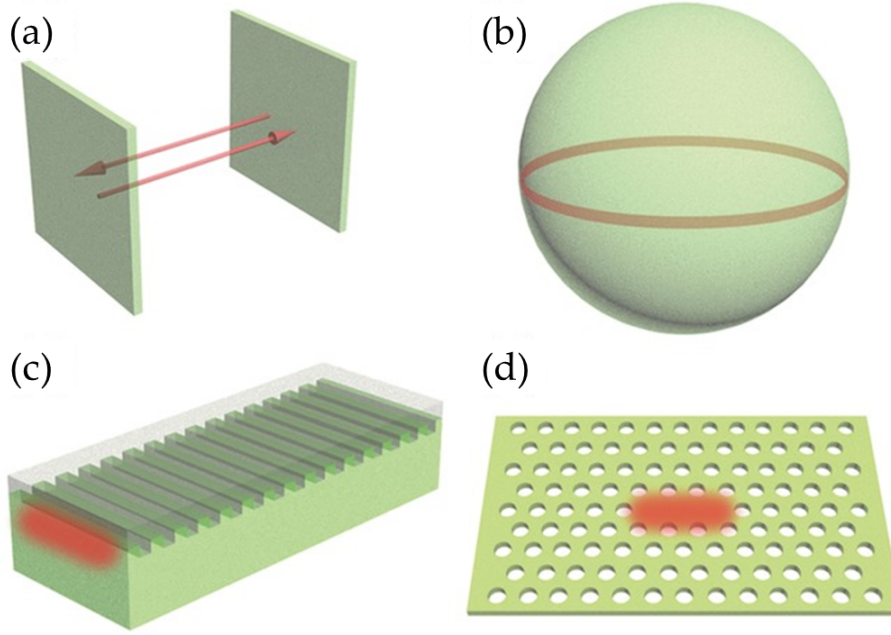
FIGURE 2.13: Microcavity configurations using different confinement methods, showing the confinement region in red. (a) Fabry–Perot cavity. (b) Whispering gallery mode cavity. (c) Distributed feedback cavity. (d) Photonic crystal defect cavity.[13]

where $\epsilon(r)$ is the dielectric constant, $|E(r)|$ is the electric field strength and V is the volume encompassing the resonant cavity. Whereas the Q-factor quantifies the *temporal* confinement of light, the mode volume V_m quantifies the *spatial* confinement of light. Cavities that simultaneously confine light for a long time and within a small volume are known to exhibit enhanced spontaneous emission.[85,97–99] This phenomenon is called the Purcell effect, or Purcell enhancement, and it is defined by the Purcell factor F_p. It is dependant on the ratio between the Q-factor of a mode and the mode volume V_m, and is explicitly defined as

$$F_p = \frac{3}{4\pi^2} \frac{Q}{V_m} \left(\frac{\lambda_0}{n_{\text{eff}}} \right)^3, \tag{2.24}$$

where λ_0 is the wavelength of the mode in vacuum and n_{eff} is the effective refractive index of the mode. Specifically, the Purcell factor is a measure of the enhancement of the spontaneous emission rate in a cavity/resonator compared to the emission rate in a bulk medium.[97] Enhanced spontaneous emission could indicate an increase in radiative (band-to-band) recombinations in the material, but this still requires further investigation.[18,100] As mentioned throughout this chapter, in the radiative limit, an optimized open-circuit voltage V_{oc} can be obtained. Therefore, the Purcell enhancement could be of interest to photovoltaic applications, especially in the pursuit for higher external radiative efficiencies of solar cells in open-circuit conditions.[9]

2.4.2 Whispering gallery modes

The guided mode of special interest in this thesis is called the whispering gallery mode (WGM). WGMs can be used for a variety of applications such as lasing and wavelength tuning,[101–105] biosensing[95,106,107] and optical coupling.[108,109] This is mainly because WGMs exhibit high Q-factors and low mode volumes,[98] and with it, a high Purcell factor (equation 2.24). Since the Purcell enhancement of WGMs could indicate higher radiative efficiencies, they are worth being investigated more in this regard.

WGMs have been proposed more than a century ago when Lord Rayleigh published a paper during the study of the acoustic wave propagation phenomena in the dome of St Paul's Cathedral in London.[17] Close to the wall of the dome, one could hear the whispers of anyone standing anywhere else near the wall of the dome, regardless of the distance between them. Lord Rayleigh attributed this to the ability of acoustic waves to stick to the walls and propagate along them. As it turns out, this wave-like property also holds in the optical domain: WGMs can also occur in optical cavities with a closed concave surface, similar to the dome of a cathedral.[106]

closed loop after one round-trip   mismatch after one round-trip
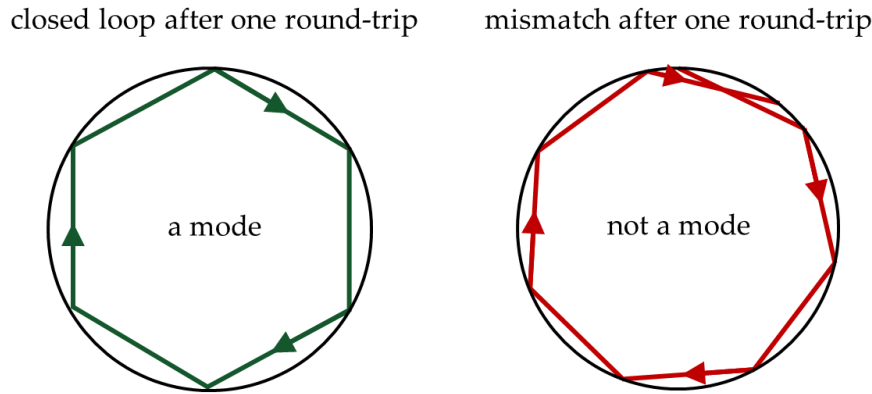
FIGURE 2.14: Mode structure using the ray optics formalism. The green line illustrates a beam whose optical path creates a closed loop after one round trip and is therefore able to resonate in the cavity. The red line illustrates a beam which does not satisfy the resonance criterium.

Optical WGMs can be best understood by combining the concepts of total internal reflection (TIR) and constructive interference (as visualized in figure 2.14). Total internal reflection occurs inside materials that have a larger refractive index than their environment: semiconductors exhibit this phenomenon because they generally have refractive indices higher than air or polymer materials they are embedded in. As the light reflects azimuthally in a nanowire, it may self-interfere after travelling one round. It will constructively interfere and form a WGM if light satisfies the equation[13]

$$m\lambda_0 = 2\pi R n_{\text{eff}}, \tag{2.25}$$

where m is the angular mode number, λ_0 is the wavelength of the light in vacuum, R is the radius of the nanowire and n_{eff} is the effective refractive index of the mode. While equation 2.25 gives a fundamental understanding of the WGMs, it needs to be

further explored with a correction term to accurately deduce the separate resonant wavelengths for TE and TM modes. Lam *et al.*[110] developed the framework to do so, using numerical approximations. The resonant wavelengths can be found as a function of the cavity radius R, cavity refractive index n_1, environment refractive index n_2, radial mode number r and angular mode number m using[13, 104–106, 110]

$$\lambda^{-1}(R, n_1, n_r, r, v) = \frac{1}{2\pi R n_1}\left[v + 2^{-\frac{1}{3}}\alpha(r)v^{\frac{1}{3}} - \frac{P}{\sqrt{n_r^2 - 1}}\right.$$
$$\left. + \frac{3}{10}2^{-\frac{2}{3}}\alpha^2(r)v^{-\frac{1}{3}} - 2^{-\frac{1}{3}}P(n_r^2 - \frac{2}{3}P^2)\frac{\alpha(r)v^{-\frac{2}{3}}}{(n_r^2 - 1)^{\frac{3}{2}}}\right], \quad (2.26)$$

where $n_r = \frac{n_1}{n_2}$ is the fraction of the refractive indices, $\alpha(r)$ is the Airy function solution for any radial mode number r, $P = n_r$ for purely TE modes and $P = n_r^{-1}$ for purely TM modes, and $v = m + \frac{1}{2}$. We can simplify this equation by considering that the environment material is air ($n_2 = 1, n_r = n_1$) and we are only interested in fundamental modes ($r = 1$) since those are the modes most frequently observed in experiments. For fundamental modes, the Airy function $\alpha(r) = 2.338$, yielding

$$\lambda^{-1}(R, n_1, m) = \frac{1}{2\pi R n_1}\left[m + \frac{1}{2} + 1.856(m + \frac{1}{2})^{\frac{1}{3}} - \frac{P}{\sqrt{n_1^2 - 1}}\right.$$
$$\left. + 1.033(m + \frac{1}{2})^{-\frac{1}{3}} - 1.856P(n_1^2 - \frac{2}{3}P^2)\frac{(m + \frac{1}{2})^{-\frac{2}{3}}}{(n_1^2 - 1)^{\frac{3}{2}}}\right]. \quad (2.27)$$

This equation can be used to accurately verify the resonant wavelengths of different angular order WGMs in a structure with varying radius. It is instructive to realize that for large $m \gg 1$, the terms $(m + \frac{1}{2})^{-1/3}$ and $(m + \frac{1}{2})^{-2/3}$ become negligible and the expression further simplifies to[13]

$$\lambda(R, n_1, m) = \frac{2\pi R n_1}{m + \frac{1}{2} + 1.856m^{\frac{1}{3}} - \frac{P}{\sqrt{n_1^2 - 1}}}. \quad (2.28)$$

Comparing equation 2.28 with equation 2.25, we see that both the angular mode number m and the refractive index n_1 have a stronger impact on the resonant wavelength than only the combination of TIR and constructive interference predict. Since $n_1 > 1$ is a prerequisite for TIR to confine the light, $n_1 \cdot (n_1^2 - 1)^{-1/2}$ is larger than $n_1^{-1} \cdot (n_1^2 - 1)^{-1/2}$. Therefore, for the same angular mode number m, TE modes resonate at longer wavelengths than TM modes.

2.4.3 Optical modes in tapered nanowires

The introduction of a taper (gradual change of the radius along the center axis) in a straight NW structure drastically changes its photonic behaviour. Most importantly, the NC (nanocone) geometry allows for significant modification of the local density of states (LDOS) inside the structure, which describes the availability of band-to-band transitions of photons at a specific position, orientation and wavelength.[64,111] The increase in the LDOS is exemplified by the Purcell enhancement of the structure, which on its turn is associated with an overall increase in the radiative efficiency of the structure in several researches.[64,100,112] For example, Hofmann *et al.* claim a greater than 3000 times enhancement of the spontaneous emission rate in a cylindrical AlGaAs resonator through significant modification of the LDOS.[64] They find that this is possible even with a cavity with modest Q-factors (< 50) as long as the mode volume V_m is sufficiently small (of the order $10^{-4} \left(\lambda/n \right)^3$). Referring to earlier research by Lau *et al.*,[113] Hofmann *et al.* mention that through achieving high Purcell enhancements by confining the active region in a subwavelength cavity, one can access a regime in which spontaneous emission rates exceed stimulated emission rates, potentially enabling modulation speeds much faster than lasers.[64]

Moreover, the emitted light from NCs shows enhanced directivity from both experimental data and far-field projection simulations.[18,63,85,89] If we look back at figure 2.10 (b), we see that Friedler *et al.* measured a decrease in beam divergence for these structures,[85] depending on the diameter of the tapered NW. In a similar research on NW tapering, Gregersen *et al.* find that the introduction of a small tapering angle to nanowires with already divergent output beams reduces the beam divergence and increases their transmission.[89] Their results are shown in figure 2.15. Similar to Friedler *et al.*, they find that through the adiabatic expansion of the guided mode in the tapering, an increase in the photon escape probability and the photon collection efficiency are realized.
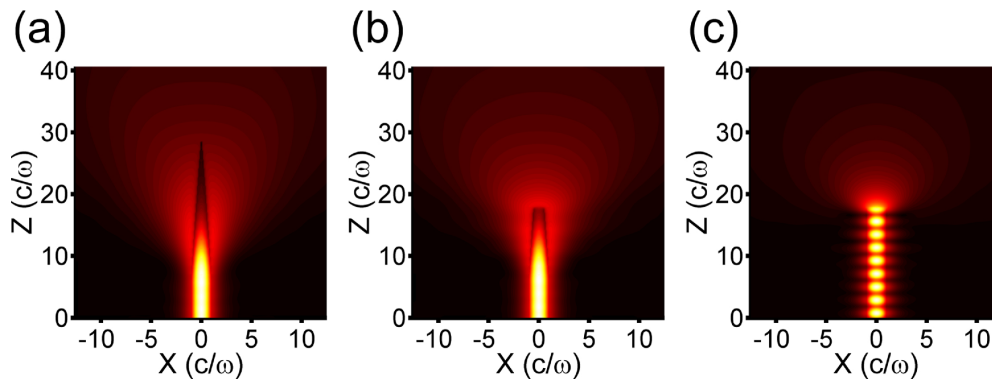
FIGURE 2.15: Electric field profile for NWs with a conical taper (a), a truncated taper (b) and without taper (c). The tapering angle is $5°$. Note that for both tapered structures, the emitted E-field intensity is higher than without a taper.

Light is not very well confined at the boundary between a straight nanowire and its substrate because they are often the same material (or have a small refractive index difference nonetheless) causing the transmission at this interface to be high.[36] In general, photons leak into the substrate and recombine there because of an abundantly high photonic density of states (DOS) in the substrate.[9] In a tapered NW however, photons may become trapped by a combined mode formation of a WGM

and a Fabry-Perot (FP) mode.[19,114] The WGM may act as the bottom facet of a vertical FP mode, illustrated in figure 2.16. The availability of combined WGM and FP modes amounts to an increase in the LDOS inside the NC, which is exemplified by their local Purcell enhancement. This Purcell enhancement could then be associated with an overall increase in the radiative efficiency,[64,100,112] but this still remains to be experimentally verified.[18]
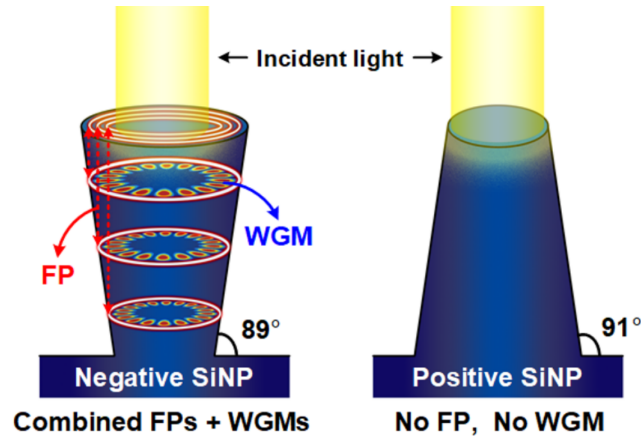
FIGURE 2.16: Schematic overview of mode formations in negatively tapered and positively tapered silicon NCs.[19]

Whereas the shape of a NC suggests that a continuous distribution of WGMs should be available along the height of the structure, Schmitt *et al.*[18] point out that only for a handful of those modes, the simultaneous condition of a FP mode between the WGMs and the top facet is met. In figure 2.17, the results of their modal analysis are visualised. Light is only trapped at discrete wavelengths in these coupled modes and the PL emission spectra of these structures show distinct peaks. This feature opens the door to many applications: one noteworthy application is a Si-based laser with narrow bandwidth and high free spectral range (FSR).[19,115,116]
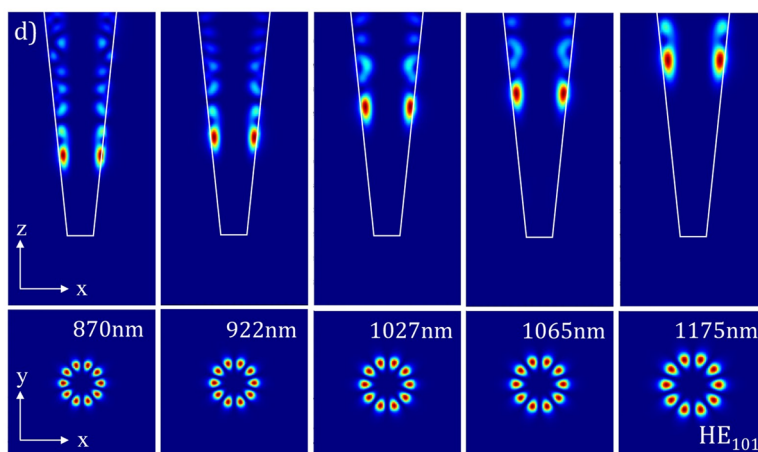
FIGURE 2.17: Characteristic (*x-z*)- and (*x-y*)-cross-sections of the energy density for HE_{101} WGMs hosted at five discrete heights inside an inverse NC. The white lines in the top figures indicate the silicon NC boundaries. The HE_{101} mode couples with different FP modes at distinct wavelengths, indicated in the bottom figures.[18]

In two papers by Schmitt *et al.* following up their initial observations,[115,116] the researchers point out that using their concept of discrete wavelength spacing, tapered silicon structures may be a key step toward fully integrated on-chip silicon photonics. Instead of an inversely tapered cone, they fabricated an inversely tapered half-ellipsoidal structure. Ultimately, they have managed to produce an emission spectrum with narrow linewidths ($\Delta\lambda = 0.33$ nm) and spectral power densities up to 8 mWcm^{-2}nm^{-1}.

Another research team took a different route. Seo *et al.* followed up the observations of Schmitt *et al.* with the fabrication of a similar silicon resonator with a weaker tapering,[19] which has been shown in figure 2.16. This inversely tapered structure still allows coupling into modes with high Q-factors and low modal volumes V_m, but also shows a FSR of nearly 85 nm at a resonant wavelength of 1102 nm. Moreover, they point out that these lasing parameters are tunable through the NC diameter and tapering angle, extending the prospects of this structure geometry.

A consideration for negatively tapered (inverse) NC arrays is their increased top reflection with respect to positively tapered (normal) NC arrays because of a larger top diameter.[117] The amount of light that enters an inverse NC – and with it, the amount of light that is absorbed – can therefore be higher than for a normal NC. Moreover, a paradox seems to arise at the top facet of an inverse NC: it should equally contribute to the formation of a FP mode and the adiabatic expansion of the optical modes to the environment. The confinement of the mode is only required for gaining a high Q-factor, and through it, a high Purcell factor of the mode as to increase the spontaneous emission rate. A successful expansion of the mode on the other hand demands a low reflectivity at the top facet. Therefore an answer to this problem could be that the WGM has a high Q-factor, while the coupled FP mode has a low Q factor. This seems to be the case in figure 2.17, where the photons are well confined in the radial direction and are free to propagate towards and through the top facet.[18] This needs to be confirmed with simulations or experiments.

Chapter 3

Methods

In this section, an overview of the numerical and experimental methods is given. First, the software and numerical method used for the simulations are introduced. Then, the general nanowire fabrication process is explained. Next, the technique used to transfer the nanowires from their substrate is introduced. Lastly, the experimental setup used to investigate the nanowires and measure their PL is shown.

3.1 Finite-difference-time-domain simulations

For systems whose mathematical models are too complex to provide analytical solutions, such as systems that exhibit nonlinear optical effects with complex dielectric structures, numerical simulations are required to study their behaviour. These simulations provide essential insight and can verify results from experimental data.

3.1.1 Fundamentals of finite-difference-time-domain simulations

All simulations for this thesis were performed with the finite-difference-time-domain (FDTD) solver by Ansys Lumerical. The FDTD method is a versatile modeling technique that solves Maxwell's equations on a finite and discrete grid 3D-environment.[118–120] It is a time-domain technique, so it lends itself for both intuitive and insightful simulations. For example, when a broadband pulse (such as a Gaussian pulse or an electric dipole) is used as a source, then the response of the system can be obtained over a wide range of frequencies with a single simulation. This is useful in applications where resonant frequencies are not exactly known, or anytime a broadband result is desired. Moreover, since FDTD calculates the E- and H-fields everywhere in the computational domain as they evolve in time, animated displays of the electromagnetic field movement through the model can easily be obtained.

The FDTD solver calculates the Maxwell curl equations for non-magnetic materials which are given by

$$\frac{\partial \vec{D}}{\partial t} = \nabla \times \vec{H},$$
$$\vec{D}(\omega) = \varepsilon_0 \varepsilon_r(\omega) \vec{E}(\omega),$$
$$\frac{\partial \vec{H}}{\partial t} = -\frac{1}{\mu_o} \nabla \times \vec{E},$$

where $\vec{H}$, $\vec{E}$ and $\vec{D}$ are the magnetic, electric and displacement fields respectively and $\epsilon_r(\omega)$ is the complex dielectric constant. Using Cartesian coordinates, Maxwell's equations have six electromagnetic field components: E_x, E_y, E_z and H_x, H_y, and H_z. The FDTD method solves these equations on a discrete spatial and temporal grid, where each field component is solved at a slightly different location within the grid cell (called the Yee cell),[121] as shown in figure 3.1. Data collected from the FDTD solver is automatically interpolated to the origin of each grid point.
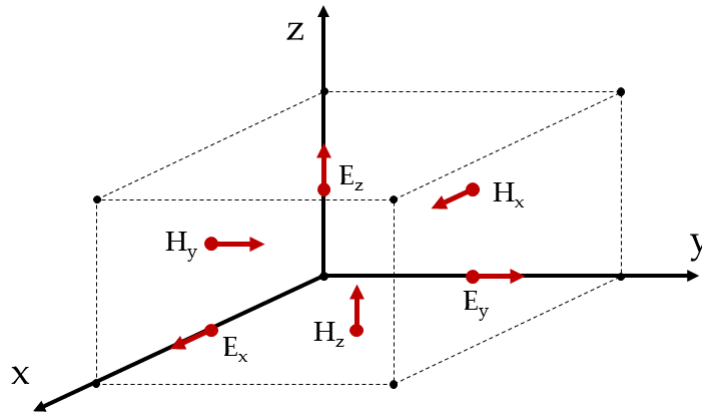

FIGURE 3.1: Lumerical calculates E- and H-fields in a grid using the Yee cell: a rectangular unit cell where each E-field vector component is located midway between a pair of H-field vector components.[121]

The structure geometries and material properties can be easily altered within the computational domain, enabling the simulation of any complex geometry and its response to a variety of electromagnetic sources. The source center frequency or wavelength and the bandwidth determine the material fits inside the simulation region. In Appendix A, a few considerations about the material fits are summarized.

Next to that, the FDTD solver supports a range of boundary conditions, such as perfectly matched layer (PML), periodic, Bloch and metal. By default, boundary conditions are set to PML. In essence, a PML is an effective absorbing layer with material properties derived from a coordinate transform from real to complex co-ordinates. Practically, it effectively provides outgoing boundary conditions within a finite simulation volume. In this way, the divergence of the normalization is removed by converting the radiative losses to the outside region into absorptive losses within the simulation volume.[99] PML boundaries ideally absorb all incident energy, but as a consequence of using finite difference approximations to discretize the PML equations, there is some room for numerical instabilities.

For periodic structures, such as a NW array, the periodic or Bloch boundary conditions can be used. They can only be used in conjunction with plane wave sources, as any other source will be mirrored at these boundaries and will interfere with itself, resulting in inaccurate simulations. Periodic boundaries simply copy the fields at one edge of the simulation region and re-inject them at the other edge, resulting in quick simulations. Bloch boundaries are very similar, but while copying the fields from one edge to the other they also apply a phase correction to the fields. Therefore, Bloch boundaries are suitable for plane waves at any injection angle whereas periodic boundaries only work for a perpendicular injection angle (e.g. with wave propagation parallel to the boundaries).

3.1.2 Limiting simulation duration

There are a couple of things to take into account before starting a simulation using Lumerical. Before running a large amount of simulations, it is important to minimize the duration of each simulation. The simulation region is defined by many properties of the FDTD-object, but most important for its duration are the spatial dimensions, mesh settings, simulation time and boundary conditions.[118,120]

The spatial dimensions span the simulation region and the mesh size determines the number of points at which the E- and H-fields are evaluated. The default mesh setting is 'auto non-uniform', which requires the least amount of computation power. In this setting, the size of the mesh cells varies as a function of position throughout the simulation region, depending on wavelength and material index.[118] Such a mesh can make FDTD calculations more accurate, while requiring less memory and less computation time than a comparable uniform mesh. The mesh accuracy ranges from 1 to 8, which corresponds to at least 6 mesh points per wavelength (1), 10 points per wavelength (2)... up to 34 points per wavelength (8). Therefore simulations with shorter wavelengths require more computation power and time. The mesh size greatly affects the simulation duration: if it is halved, the simulation duration increases with a factor 16. This is because the number of points in the simulation region and therefore the amount of calculations increases with a factor $2^3 = 8$ while the time step dt also increases, with a factor 2.[118]

The simulation time is the amount of time that passes before the simulation is ultimately stopped. Normally, shutoff conditions are set for cases where the simulation has converged before reaching the end of the simulation time (by default, if less than 10^{-5} times the injected energy is remaining inside the simulation region) or cases where the simulation has diverged (if more than 10^5 times the injected energy is present in the simulation region). Most diverging simulations are caused by instabilities in the time step dt or through the faulty interaction between dispersive media and PML boundaries. In general, the simulation time must be long enough to reach the auto-shutoff level if there are PML boundaries and/or absorbing materials involved.[118] The exceptions are high Q cavity and bandstructure calculations, where reliable results can be obtained without reaching the auto-shutoff.

Lastly, boundary conditions can be advantageous to the simulation duration too. Standard PML boundary conditions are used by default, but as described above, this sometimes leads to diverging simulations (for example, when simulating a silver mirror extended into the PML boundaries which has a large real and imaginary part of the electric permittivity). In those cases, stabilized PML settings were chosen, sacrificing simulation duration for stability. Periodic boundary conditions are used whenever simulating a periodic structure, unless the angle of incidence of the plane waves is changed: then, Bloch boundary conditions are necessary.[118]

The simulations for this report have mostly been run outside of the regular FDTD environment, to limit computation power. It involves the generation of many .fsp files (FDTD simulation project files) using .lsf scripts (Lumerical script files), using Windows batch files to run and analyze the FDTD simulations, and exporting their data to graphing tools.

3.1.3   Calculation methods of photonic parameters

Lumerical FDTD contains built-in tools and analysis groups to calculate many of the photonic parameters that are mentioned in section 2.4.1. A small summary of the parameters that are calculated in this thesis and an interpretation of their physical meaning are given here.

The mode effective index n_{eff}

FDTD calculates the effective mode indices n_{eff} according to theory found by Chapman and Hall,[91] with the help of a mode expansion monitor. This monitor combines a mode profile and index profile of a cross-section and then calculates the mode effective refractive index n_{eff} as

$$n_{\text{eff}} = \frac{\mu_0}{c} \cdot \frac{\int n^2 (\vec{E} \times \vec{H}^*) \cdot \hat{z} \, \mathrm{d}A}{\int n^2 |\vec{E}|^2 \, \mathrm{d}A}, \tag{3.1}$$

where n is the refractive index of the waveguide, E is the electric field strength, H^* is the conjugated magnetic field strength and $\hat{z}$ is the unit vector perpendicular to the cross-section. In essence, it determines the $\hat{z}$-component of the time-averaged Poynting vector through the cross-section and divides it by the total intensity of light inside the mode.[91] Since for the calculation of n_{eff}, only a mode expansion monitor is required, it is not necessary to run a simulation beforehand which makes it an easy calculation. For modal analysis of structures only, the tool Lumerical MODE is recommended over Lumerical FDTD.

The spontaneous emission factor β

An important parameter to characterize the coupling and emission of waveguide modes is the spontaneous emission factor β. The β-factor is equal to the fraction of the photons that are emitted into any given mode, compared to the total emission into all available modes in the structure and its surroundings, including radiation modes.[85,122] Therefore it is sometimes referred to as the coupling efficiency or coupling ideality.[18,63,102,108,123] By tracking the β-factor for different NW geometries, the optimal setup can be determined for emission into WGMs. Note that in this report, the β-factor is always referred to with the symbol β whereas the propagation constant of a mode is always reffered to with the symbol β as to not confuse the two.

The β-factor is determined by calculating the transmission of energy through a mode of the NW some distance from the source. In Lumerical, a frequency domain field and power monitor can be coupled with a mode expansion monitor to calculate the transmission power of each mode separately. For a given radius, the transmission power of each mode should then be averaged over all positions and orientations of the emitting dipole within the nanowire. This averaging is required because spontaneous emission can occur nearly everywhere within the nanowire at open-circuit conditions because of charge carrier diffusion.[122]

The mode volume V_m

Lumerical FDTD contains a collection of analysis groups to calculate more compound parameters such as the mode volume V_m and the Q-factor. These calculations require a simulation run first. By default, the mode volume V_m is calculated using

$$V_m = \frac{\left(\int_V H^2 \, dV \right)^2}{\int_V H^4 \, dV}, \tag{3.2}$$

where H is the magnetic field strength and V is the cavity volume. This expression only requires the magnetic field strengths inside the cavity and is therefore computationally easier than the definition provided in Chapter 2, which also requires an index monitor. We instead use this latter, more accurate definition:

$$V_m = \frac{\int_V \varepsilon(r)|E(r)|^2 \, dV}{\max(\varepsilon(r)|E(r)|^2)}. \tag{3.3}$$

The quality factor Q

Another analysis group is used for Q-factor calculations. Lumerical considers two classes of cavities for Q factor calculations, low Q cavities and high Q cavities. A cavity is considered a low Q cavity if the electromagnetic fields completely decay from the simulation region in a timespan that can be simulated reasonably by FDTD, shown in figure 3.2 (a). In this case, the Q-factor is calculated from the Fourier transform of the field and by identifying the resonance frequencies and determining the FWHM of the resonant peaks. Therefore, it uses equation 2.22:

$$Q = \frac{\nu_0}{\delta\nu}. \tag{3.4}$$

A cavity is considered a high Q cavity if the electromagnetic fields do not completely decay from the simulation region in a computationally reasonable timespan, visualised in figure 3.2 (b). If this is the case, the Q-factor cannot be determined from the Fourier transform of the frequency spectrum because the FWHM $\delta\nu$ of the resonances are limited by the simulation time t_{sim} by $\delta\nu = t_{\text{sim}}^{-1}$.[118] The Q-factor is instead determined from the slope of the envelope of the decaying signal. First, equivalently to equation 3.4, we have

$$Q = \frac{\omega_0}{\delta\omega}, \tag{3.5}$$

where we now take the angular frequencies $\omega_0 = 2\pi\nu_0$. To obtain a value for the FWHM $\delta\omega$, we consider the time domain signal of the resonance, which is described by

$$E(t) = \exp\left(-\alpha t + i\omega_r t\right) u(t), \tag{3.6}$$

where α is the decay constant, ω_r is the resonance angular frequency and $u(t)$ is the signal which decays exponentially. The Fourier transform of $E(t)$ yields

$$|E(\omega)|^2 = \frac{1}{\alpha^2 + (\omega - \omega_r)^2}, \tag{3.7}$$

which shows the resonance peaks in the frequency domain. The maximum value of $|E(\omega)|^2$ is obtained when $\omega = \omega_r$: $|E(\omega_r)|^2 = \alpha^{-2}$. From this equation, we can also determine the frequencies for which $|E(\omega)|^2$ is half the maximum value:

$$\frac{1}{\alpha^2 + (\omega - \omega_r)^2} = \frac{1}{2\alpha^2}, \tag{3.8}$$

which is solved for $\omega_+ = \omega_0 + \alpha$ and $\omega_- = \omega_0 - \alpha$. Therefore, the FWHM $\delta\omega$ is equal to $\omega_+ - \omega_- = 2\alpha$. Substituting this value into equation 3.5 and solving for α yields

$$\alpha = \frac{\omega_0}{2Q}. \tag{3.9}$$

We know that the time domain signal of the resonance decays exponentially, so if we take its logartihm, we obtain a linear function for the signal envelope. We can then relate the slope of the decay to Q. Substituting equation 3.9 into equation 3.6, taking the absolute value and taking the logarithm we obtain

$$\log_{10}(|E(t)|) = \frac{-\omega_0 t}{2Q} \log_{10}(e) = at, \tag{3.10}$$

where a is the slope of the logarithm of the envelope of the time signal. Solving for Q yields

$$Q = \frac{-\omega_0 \log_{10}(e)}{2a}, \tag{3.11}$$

which is the expression Lumerical uses to calculate the Q-factor of high Q cavities. Lastly, the Purcell factor F_P is calculated automatically for each dipole source after a simulation is run. It is calculated as

$$F_P = \frac{\text{dipolepower}(\nu)}{\text{sourcepower}(\nu)}, \tag{3.12}$$

where dipolepower(ν) and sourcepower(ν) are functions that return the power radiated into the system. Specifically, the function sourcepower(ν) returns the optical power injected into the simulation region by any source that is not a dipole (plane wave, Gaussian, mode, etc.) and is determined by

$$\text{sourcepower}(\nu) = \frac{1}{2} \int \text{Re}\left(P(\nu)_{\text{source}}\right) \, dS, \tag{3.13}$$

where $P(\nu)_{\text{source}}$ is the Poynting vector determined from the E- and H-fields injected by the source and dS spans the injection plane. The sourcepower of a dipole can be calculated by the same equation, but it will not be equal to the actual radiated power into the system. A dipole's power is highly dependant on the surrounding

structure since the reflections from any interface will interfere with the fields injected by the dipole.[119] The function dipolepower(ν) compensates for these reflections and calculates the actual radiated power of a dipole. We have already seen in Chapter 2 that the emission rate is proportional to the LDOS, which is proportional to the power emitted by a source.[63,64,112] Therefore, equation 3.12 reveals that given a certain setup, certain dipole locations will result in enhanced emission with respect to a homogeneous environment: mapping the LDOS landscape of the structure.[119]

In figure 3.2, examples of the temporal evolution of the electric field intensities inside a low Q and high Q cavity are shown. Both show a compound time signal indicating multiple resonances, but they clearly have an exponentially decaying envelope function. Note that because of the significant difference in the time-axis, the Q-factors of these two cavity examples must be calculated in different ways.
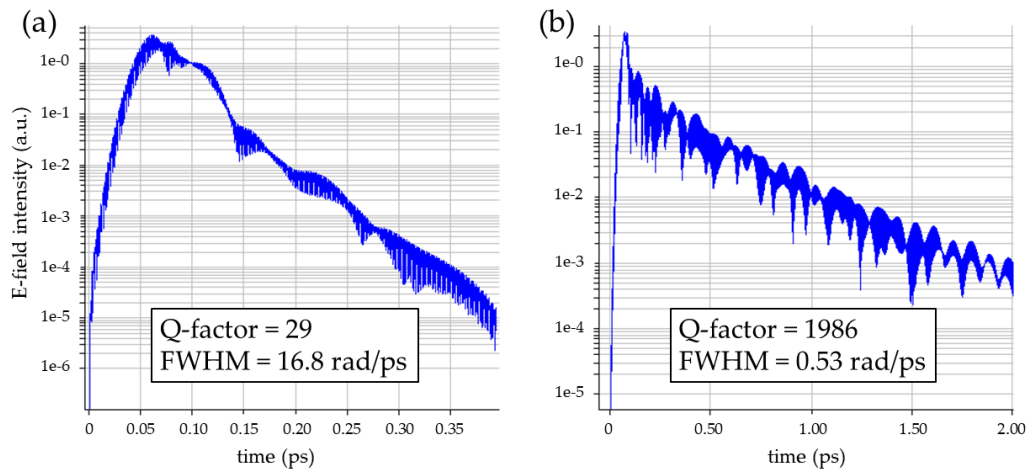

FIGURE 3.2: Electric field intensity measured over time in a low Q cavity (a) and a high Q cavity (b) for cavities with similar resonance frequencies. (a) The source is injected within the first 100 fs, but then the E-field quickly decays before reaching the shut-off limit (1e-5) around 400 fs. (b) The source is again injected in the first 100 fs but the E-field is contained for much longer. Even after 2000 fs, 1e-3 of the initial field strength persists.

The photon escape probability P_{esc}

For semiconductor materials with a low internal radiative efficiency η_{int}^{PL}, it is crucial to have a high photon escape probability P_{esc} such that non-radiative recombinations are kept to a minimum.[122] The process of re-absorption and re-emission, often called photon recycling,[88] can be beneficial to increase the amount of photons that are emitted into a defined escape cone, as long as photons are dominantly recombining radiatively. The internal radiative efficiency η_{int}^{PL} of our InP samples is estimated to be 10^{-3}, so the photon escape probability should be optimized to unity.

To model the emission from radiative recombinations inside a structure, the optical transition of an electron-hole pair can be modeled as dipole emission.[92] We assume that the structure does not show an inherent polarization anisotropy, indicating that any polarization dependance in the structure is the result of diffraction effects.[124] Moreover, we make use of a principle called the Lorentz reciprocity, which is extensively deliberated upon in Appendix B. In short, the emission of an unpolarized

dipole emitter is straightforward to calculate for a single NW or a finite NW array, but is troublesome to calculate for emission patterns from an infinite (or otherwise very large) array. Periodic boundary conditions cause a coherent repetition of the dipole emitters, which interfere with each other and would result in inaccurate simulations.[125] Lorentz reciprocity enables the calculation of the directivity of dipole emission within an infinite NW array. Consequently, the emission from electron-hole pair recombinations inside an infinite periodic structure can be analyzed and decomposed into upward (escaping) and downward (losing to substrate) directed emission, which indicates the photon escape probability P_{esc}. The simulation setup is shown in figure 3.3.
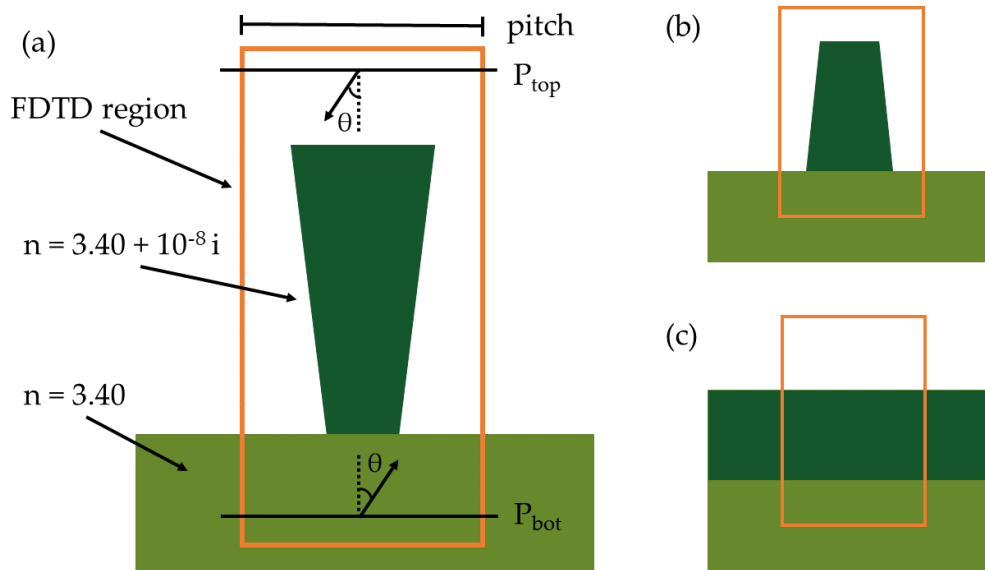

FIGURE 3.3: Schematic overview of the simulation setup to extract the photon escape probability P_{esc}. (a) An FDTD region with PML boundaries in the z-direction and Bloch boundaries in the x- and y-directions is used, where the x- and y-spans are the NC pitch. The NC is given a very small imaginary part, which is explained in Appendix B. Plane waves with polar angle θ and azimuth angle ϕ are injected either from the top or the bottom to obtain P_{top} and P_{bot}. The same procedure is done for a normal NC (b) and for a planar sample (c).

For an optimization of the photon escape probability, it is important to discuss whether P_{top} or $P_{\text{top}}/(P_{\text{top}} + P_{\text{bot}})$ should be optimized.[92] Note that the values of the parameters P_{top} and P_{bot} may be normalized to P_{bulk}, the emission to the top/bottom from a dipole in the bulk material. If the internal radiative efficiency η_{int}^{PL} is low, the total recombination rate is dominated by non-radiative recombinations. Then, the emission into the top hemisphere is proportional to P_{top} and only P_{top} should be optimized. If instead η_{int}^{PL} is close to unity, the total recombination rate is dominated by radiative recombinations. Then, $(P_{\text{top}} + P_{\text{bot}})$ is proportional to the total recombination rate and $P_{\text{top}}/(P_{\text{top}} + P_{\text{bot}})$ should be optimized. To summarize, as the internal radiative efficiency η_{int}^{PL} increases from low values to unity, it becomes less important to optimize the total emission towards the top hemisphere and more important to optimize the fraction of total emitted photons emitted towards the top hemisphere.

3.2 Nanowire fabrication process

The InP NW samples are produced using a top-down etch approach. A summary of the fabrication process is given in this section and visualized in figure 3.4. Either an undoped or a p-doped (using Zn as the dopant material) InP wafer is used as the basis. Optionally, a *p-n* junction is grown on the p-doped wafer with metalorganic vapour-phase epitaxy (MOVPE). On top of that, a SiN_x mask with a thickness of around 400 nm is deposited using plasma-enhanced chemical vapour deposition (PECVD). On top of the mask, a negative resist (ma-N 2403) is deposited and the wafer is spun for a homogeneous resist distribution. A negative resist is chosen because it hardens where it is exposed to an electron beam; desired patterns and features are imprinted into the resist using electron-beam lithography (EBL).
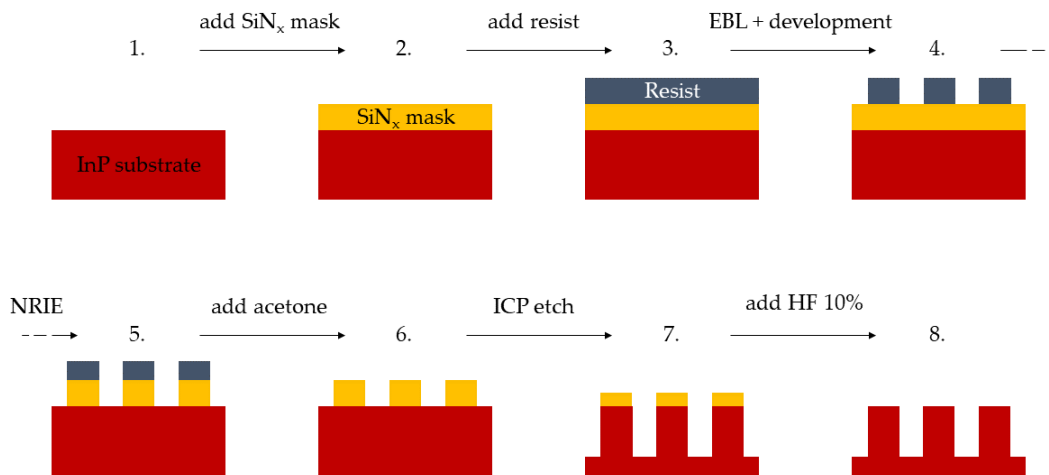

FIGURE 3.4: Schematic overview of the top-down nanowire fabrication process. Each step indicates a significant change to the configuration of the separate layers.

With EBL, a periodic array of circles is drawn into the resist. Next, the wafer is developed, where the unexposed resist is washed away using a chemical developer (ma-D 525/S) and it is rinsed afterward using water. The pattern of the resist is transferred to the SiN_x mask using nitrogen reactive ion etching (NRIE). This process is continued until all the exposed mask material is etched away, and then the leftover resist is removed with acetone. Now the nanowires are etched from the InP substrate using a Sentech inductively coupled plasma (ICP) technique with a CH_4/H_2 plasma. Any of the leftover mask is then removed using a 10% HF solution, leaving only the InP substrate with the NW array.

As a final step, a digital etch process is performed to reduce the surface roughness of the sample. With the Sentech ICP technique, an O_2 plasma oxidizes about 10 nm of the exposed surface of the sample. The oxide layer is removed with an acid and may be exposed to the O_2 plasma again to further decrease the NW size. After the digital etching step, the NW array is ready to be processed further. It is important to note that depending on the NW length and pitch, the final NWs are never exactly straight. Rather, during the etching process, they develop a slight positive tapering angle of 2.4° on average. This tapering angle occurs naturally during the top-down etching approach during the NRIE process with the negative resist and is influenced by the NW pitch and length.[126]

3.3   PDMS for nanowire transfer

As pointed out in the previous section, the development of a tapering angle occurs naturally in the fabrication process of the NW arrays. Ultimately, we are interested in measuring the difference between positively tapered and negatively tapered NWs. However, NWs with a negative tapering angle can not be produced with the combination of a top-down approach and a negative resist.[126] Instead, transparent polymers can be used to separate the wires from their substrate and change their orientation. This procedure has been performed with success before using the polymer polydimethylsiloxane (PDMS).[21–25] PDMS can be deposited on a sample in a liquid phase, occupying the space between the wires and adhering to the surface of the NW array. When cured it is solid yet flexible, and it can be easily removed from the substrate with the NWs inside (see figure 3.5). It is an excellent polymer for the purposes of this thesis because – once cured - PDMS has sturdy mechanical properties and a very constant refractive index across the entire solar spectrum.[127] Moreover, the NWs can be put on a mirror, enhancing their absorption and emission.[24,25]

FIGURE 3.5: A fully cured layer of PDMS. It is transparent and by the refraction of my finger, the refractive index $n = 1.4$ becomes apparent.

The NWs are embedded in a layer of PDMS based on a recipe presented by Standing *et al.*[20] The PDMS layer effectively consists of two separate layers with a different base-to-cure weight ratio. The first layer has a base-to-cure ratio of 10:4 which is obtained by preparing 5.0 g of elastomer base and 2.0 g of elastomer cure in a beaker and diluted with 4.6 g of hexane. These quantities are chosen to obtain the optimal viscosity of the PDMS for penetrating between the nanowires, reaching a 65% dilution of hexane. The solution is stirred until a homogeneous liquid is acquired, after which it is ready for deposition. The PDMS is deposited on the sample, which is then placed inside a vacuum desiccator at a low vacuum (10^{-2} Torr) for 25 minutes alongside a beaker of hexane. The hexane beaker is employed to reduce the evaporation of hexane from the PDMS. The sample is removed from the desiccator and spun at 1000 rpm for 60 s to obtain a layer thickness of 60 μm. After spinning, the sample is put back into the vacuum desiccator, this time without a beaker of hexane, at a low vacuum (10^{-2} Torr) for approximately 2 days until the PDMS has fully cured.

For the second layer, another PDMS mixture is produced that functions as a thicker layer for easier removal of the nanowires from the substrate. The base:cure weight ratio for the second layer is 10:1, therefore 5.0 g of elastomer base and 0.5 g of elastomer cure are put in a beaker. It is not further diluted with hexane. The solution is again stirred until a homogeneous substance is acquired, and is deposited onto the sample (left picture in figure 3.6). The sample is placed inside the desiccator without a beaker of hexane at a low vacuum (10^{-2} Torr) for 25 minutes. The sample is then spun once again at 1000 rpm for 1 minute to obtain a second layer thickness of approximately 60 μm. After spinning, the sample is cured in an oven at 150 °C for 10 minutes to fully cure the PDMS (right picture in figure 3.6). The nanowires embedded in the PDMS are removed from the substrate by using a razor blade. The removed nanowires are placed on a silver mirror in order to reflect the light emitted from the bottom of the nanowire back to the top, enhancing the nanowire's emission from the top by reducing the solid angle of emission. Then they are ready to be measured using the optical setup.
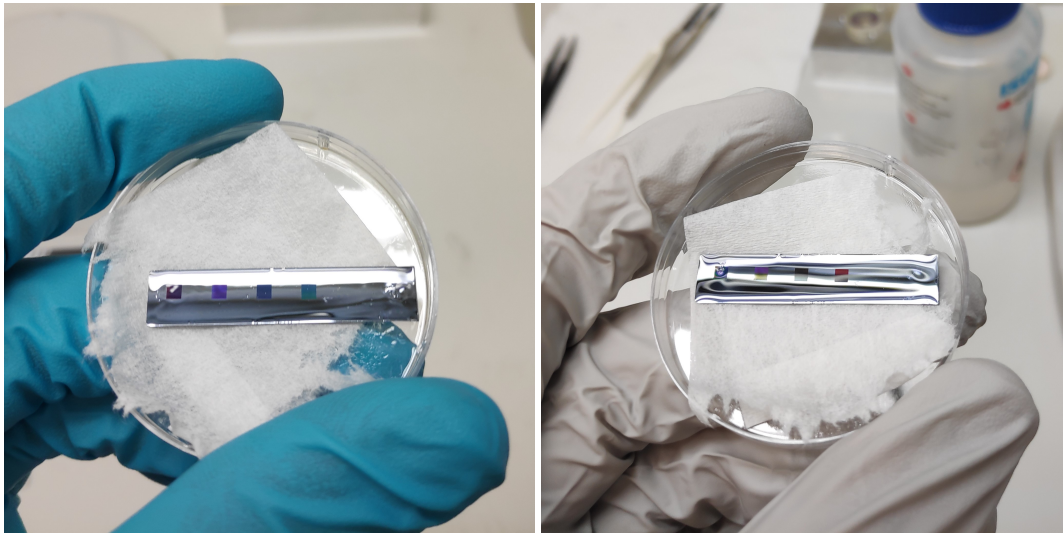

FIGURE 3.6: Photographs of a sample with four fields of NWs covered in PDMS before (left) and after (right) curing. In the right image, the PDMS has fully hardened and can be removed using a razor blade, removing the embedded NWs from the substrate.

3.4   Optical setup

The optical setup consists of a number of optical components, visualised in figure 3.7. The excitation source in this setup is a continuous wave (CW) laser with a wavelength $\lambda = 532$ nm. The laser light is guided through optical power filters to an objective, where the light is focused on the sample holder. The sample holder stands upright, and any sample can be mounted to it using adhesive tape. The sample holder can move in the (x,y)-plane and the objective can be moved in the z-direction, giving full control to focus anywhere on the sample. If the laser light is focused on an InP NW array, light is emitted through photoluminescence, which is caught by the objective again and guided towards a monochromator/spectrograph (Princeton Instruments Acton Advanced SP2500A). Right before the entrance of the monochromator, a laser filter prevents any laser light from entering the device. The monochromator directs the PL emission onto a diffraction grating, which spatially separates all incoming wavelengths. It then directs the light towards a CCD, where the PL spectrum is obtained. The CCD is a Princeton Instruments PIXIS 2KB back il-luminated CCD with eXcelon technology. A number of different blazed gratings can be chosen from inside the spectrometer (60 g/mm, 600 g/mm and 1200 g/mm) to make the trade-off between bandwidth and resolution of the signal. All experiments are performed at room temperature.

The yellow optical path in figure 3.7 is used to align the sample. The beamsplitter and mirrors affected only by this optical path can be removed before PL measure-ments take place. Moreover, the power filters can be removed and adjusted and by monitoring the power meter, a range of optical excitation powers can be obtained.
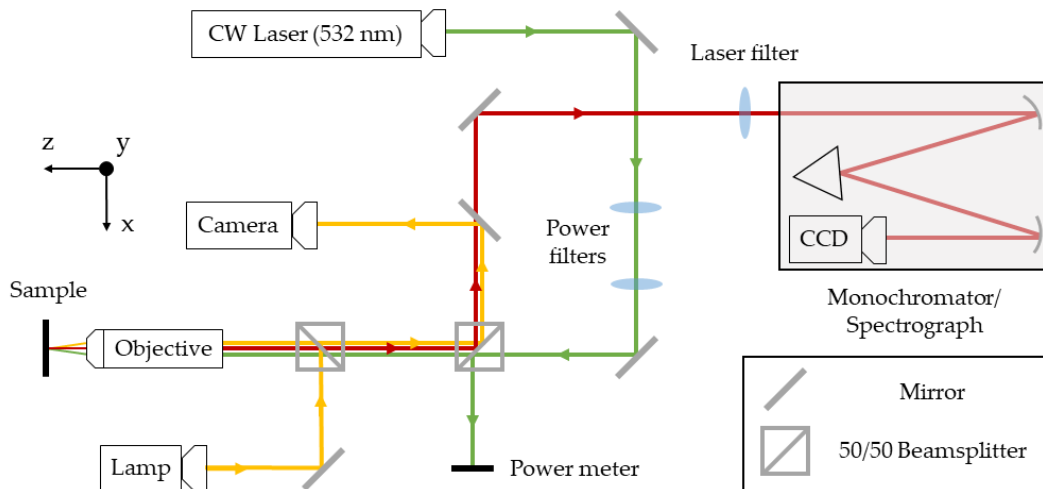

FIGURE 3.7: An overview of the experimental optical setup. The op-tical paths of the excitation laser and PL emission are given in green and red respectively. The yellow optical path is used for optical align-ment and sample focussing. The objective can be moved strictly in the z-direction and the sample can be moved in the x- and y-directions.

Chapter 4

Numerical simulations

In this section, an overview of the numerical simulations carried out for this thesis is given. The mode effective refractive index is calculated and discussed. Then, the role of whispering gallery modes in the structures is studied. Lastly, the photon escape probability of these structures is analyzed and discussed.

In this thesis, the structures of interest are based on NW arrays which optimize their benefits over planar structures, summarized in the previous chapter. We want to investigate the relation between the Purcell enhancement of tapered NW configurations and the external radiative efficiency of those configurations. Since we expect WGMs to play an important role in the Purcell enhancement, it is best to start this investigation by simulating the behaviour of WGMs in NW structures.

4.1 The mode effective refractive index

A general NW array can be generated inside the FDTD solver environment, and looks like the structure presented in figure 4.1. It is possible to calculate the available modes in this structure using the mode expansion monitors. A mode expansion monitor is a 2D-object that spans across a region of interest in the 3D-structure. It obtains a refractive index profile of this cross-section and is able to calculate the electric and magnetic fields of all available modes for any given wavelength accordingly. The strength of these mode expansion monitors lies in their ability to track modes of interest during simulations, keeping track of the energy coupled into or from them over time. For arbitrary settings of the NW dimensions and wavelengths, the mode expansion monitor reveals the WGMs in NWs, as is shown in figure 4.2.
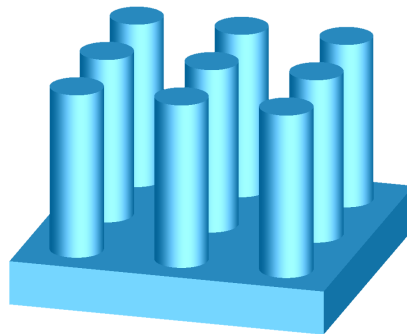
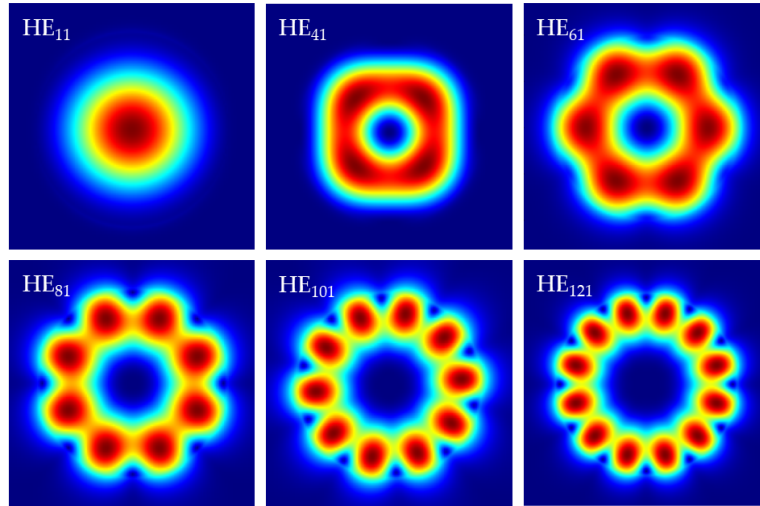FIGURE 4.1: A square NW array in the FDTD solver environment.

FIGURE 4.2: The cross-sectional energy densities of the fundamental mode HE_{11} and the five lowest angular order fundamental WGMs inside a NW.

The cross-sectional energy densities of these modes share a lot of information. The fundamental HE_{11} mode has a peak energy density at the core of the NW, as expected. For the other modes in figure 4.2 it is clear that they have a near zero energy density at the core of the NW, instead storing their energy in a torus-shape close to the circumference of the NW. This reaffirms that the underlying principle of these modes is a combination of TIR along the cylindrical walls and constructive interference, and that they are indeed WGMs. It is also clear that they can be categorized by their radial and angular mode numbers, where we have adopted the naming convention used in the paper by Schmitt *et al.*[18] We observe that for higher angular order modes, the light is confined more strictly from the center of the NW.

Equation 2.25 predicts that each WGM resonance has an associated effective refractive index n_{eff} for a given wavelength and NW radius, so it is instructive to track the values of n_{eff} for a single wavelength for all WGMs as the radius changes. Therefore we performed simulations for InP NWs at the bandgap wavelength $\lambda_0 = 922$ nm. For these simulations, the regular material database values of InP have been overwritten to suppress the imaginary part of the complex electric permittivity. This is done because we are not interested in the losses of the modes, which is justified in Appendix A. In short, in the weakly absorbing region this suppression of the imaginary part will still return a realistic description of the emissive properties. The effective refractive index as a function of NW radius is presented in figure 4.3.

Light cannot be coupled into WGMs for any radius $r < 159$ nm. This is similar to findings by Brongersma *et al.* who mention that light cannot be coupled into the fundamental HE_{11} mode if the NW radius is too small.[12] For $r \geq 159$ nm the first WGM – the HE_{41} mode – becomes available for light to be coupled into the NW structure. As the radius increases further, higher order WGMs like the HE_{61} and HE_{81} modes become available incrementally. We also see that for a given radius and wavelength, no two WGMs have the same n_{eff}. This means that for a given radius and wavelength, each WGM propagates with a different propagation constant β, as is explained in section 2.4.1. This is expected, as each mode is a unique solution to Maxwell's equations inside a waveguide and is completely characterized by their
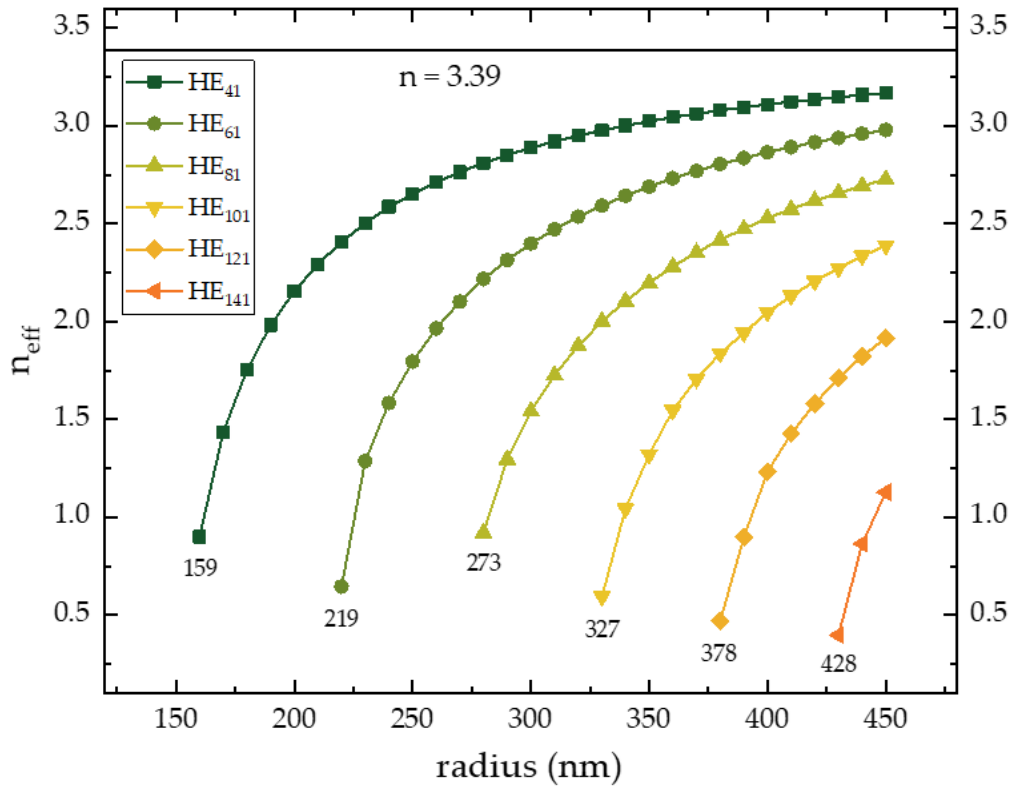
FIGURE 4.3: The effective mode index n_{eff} of various WGMs as a function of NW radius r inside lossless InP NWs. Beneath each curve, the minimal radius for the availability of the corresponding mode is given.

propagation constant β.[91] The lowest order modes have the highest propagation constants β, which means their wavevector k is more nearly parallel to the direction of propagation in the waveguide. As such, the effective refractive index is a measure of confinement of the modes.

At the minimal radius points of each mode, $n_{\text{eff}} \approx 1$, which means the mode is not completely guided within the structure and has partly expanded into the environment: it is technically a leaky mode (explained in section 2.4.1). This is observed for silicon NWs by Namassivayane *et al.* who notice that the mode energy is partly confined outside of the structure boundaries near these minimal radius points, which they refer to as the cut-off condition.[128] Conversely, as the NW radius increases, the effective refractive index of each mode approaches the refractive index of InP at $\lambda_0 = 922$ nm, $n = 3.39$. This asymptotic behaviour is reported in the same paper by Namassivayane *et al.*[128] They observe that for an increasing radius, an increasing portion of the optical power of the modes is well confined inside the NW structure which expresses itself in effective indices close to the material's refractive index.

In a similar paper on silicon NWs by Seo *et al.*,[19] the authors express that a low n_{eff} results in a low mode coupling to the substrate – at the bottom facet of the NW structure. This is desirable, because a low mode coupling to the substrate results in fewer losses through recombinations in the substrate.[9] This phenomenon is explained through equation 2.18, where the low mode coupling can be attributed to a

high reflectivity at the bottom facet because of a large difference between the substrate material refractive index and the mode effective index. In order to successfully expand photons to the environment at the top facet, n_{eff} should be smaller at the top than at the bottom. This poses a challenge for straight NW structures: we see from figure 4.3 that n_{eff} is equal throughout a NW for a fixed radius r whereas ideally, n_{eff} changes gradually for each mode between the bottom and top facet. A tapered NW could solve this issue by introducing a smooth transition of the mode effective indices.[18,56,85]

Since it is not directly apparent which values for n_{eff} are optimal for the emission from WGMs, it is instructive to investigate what other researchers have found. In the paper by Schmitt *et al.*,[18] there is no direct statement of the effective refractive indices of their emitting modes, but there is a way to calculate them. We reiterate equation 2.25:

$$m\lambda_0 = 2\pi R n_{\text{eff}} \tag{4.1}$$

which is the expression from the fundamental understanding of a WGM using TIR and constructive interference. We can rewrite this expression to

$$C = \frac{m}{n_{\text{eff}}} \cdot \lambda_0 \tag{4.2}$$

where $C = 2\pi R$ is the circumference the WGM resides at. In their paper, Schmitt *et al.* have plotted the circumference C as a function of resonance wavelength λ_0 for experimental data of emitting WGMs, visualised in figure 4.4 (a).[18] The equations governing the dotted lines are not specified in the paper, which makes it instructive to compare them to equation 4.2. With the use of this equation, a linear fit through the points is made. Each slope of those fits equals m/n_{eff} and since the angular mode numbers m of the WGMs are known – equal to 3, 4 and 5 for HE_{61}, HE_{81} and HE_{101} respectively – their effective indices n_{eff} are calculated from the slopes. This is visualised in figure 4.4 (b).

The effective indices of the three WGMs of interest are determined to be equal to 2.04, 2.20 and 2.29 for the HE_{61}, HE_{81} and HE_{101} modes respectively. These values are all close to the geometric mean of the refractive index of the semiconductor material (≈ 3.6 for Si between 850-1250 nm) and the environment ($= 1$ for air). This can be understood by the theory behind leaky modes.[63,93] Whereas the WGMs are still mostly guided inside the NC for $n_{\text{eff}} = 1.9 - 2.3$, part of their energy is confined outside the NC structure, and the other part is eventually emitted to the environment at the top facet by virtue of the photon escape probability P_{esc}.[55] However, we notice from figure 4.4 that the linear fits in figure 4.4 (b) do not quite fit the data points correctly, whereas the dotted lines in figure 4.4 (a) do. It is apparent that the straight line fits by definition go through the origin – the point $(C, \lambda) = (0, 0)$ – whereas the dotted line fits have an offset that causes them not to go through the origin. This offset would indicate that the model that only considers TIR and constructive interference is incomplete. This behaviour requires further investigation in a future research. One could start by using the model of a WGM based on spherical harmonics,[110] which has been introduced in Chapter 2, to predict the behaviour of optimal WGM emission. For now we will assume the effective index n_{eff} to ideally be in the range $1.9 - 2.3$ for emitting WGMs.
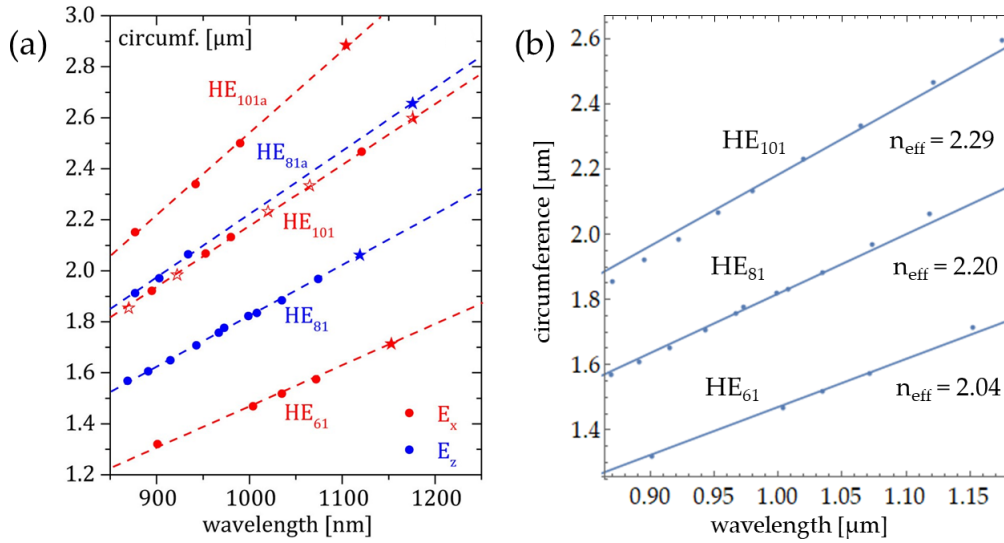
FIGURE 4.4: Experimental data by Schmitt *et al.* of PL emission from WGMs from negatively tapered silicon NCs.[18] (a) Data presented in their paper which indicates the relation between resonant wavelengths and the circumferences inside the NC structure they reside at. (b) Linear fits to the data of HE_{61}, HE_{81} and HE_{101} using equation 4.2, where the slope = m/n_{eff}.

4.2 Emission from whispering gallery modes

Next to the mode effective index, an important parameter to characterize the coupling and emission of waveguide modes is the spontaneous emission factor β. The β-factor is determined by calculating the transmission of energy through a mode of the NW some distance from the source. Because of computational restrictions, we chose to evaluate as much random dipole positions and orientations as possible, instead of a structured set of orientations of the emitting dipole, to best approach the β-factor. For an infinitely long straight InP NW with radius r, random dipole locations across the cross-section of the NW are chosen. On each location, three simulations are performed where a dipole is placed with an emission wavelength $\lambda = 920$ nm with a polarization in one of three perpendicular orientations. This is done for r in the range of 150-400 and the results are shown in figure 4.5.

From figure 4.5, we see that the highest emission of randomly oriented dipoles at any NW radius is into the fundamental mode, as expected.[108,123] As a general trend, the β-factor decreases as a function of r, because the injected dipole energy is divided over an increasing number of guided and leaky modes that are available in the NW. The very low values of the β-factor around the minimal radius points of the WGMs are attributed to the fact that over the distance between the dipole and the monitors, much of the energy in these WGMs is lost because of a low mode effective index n_{eff}. The energy is most probably coupled into other modes with a higher mode effective index. We observe a sharp increase in the β-factor for increasing radii which is attributed to a similar sharp increase in n_{eff} visible in figure 4.3, and then a drop-off of each WGM similar to the decrease in β of the fundamental mode. This again is caused by an increasing number of available modes.
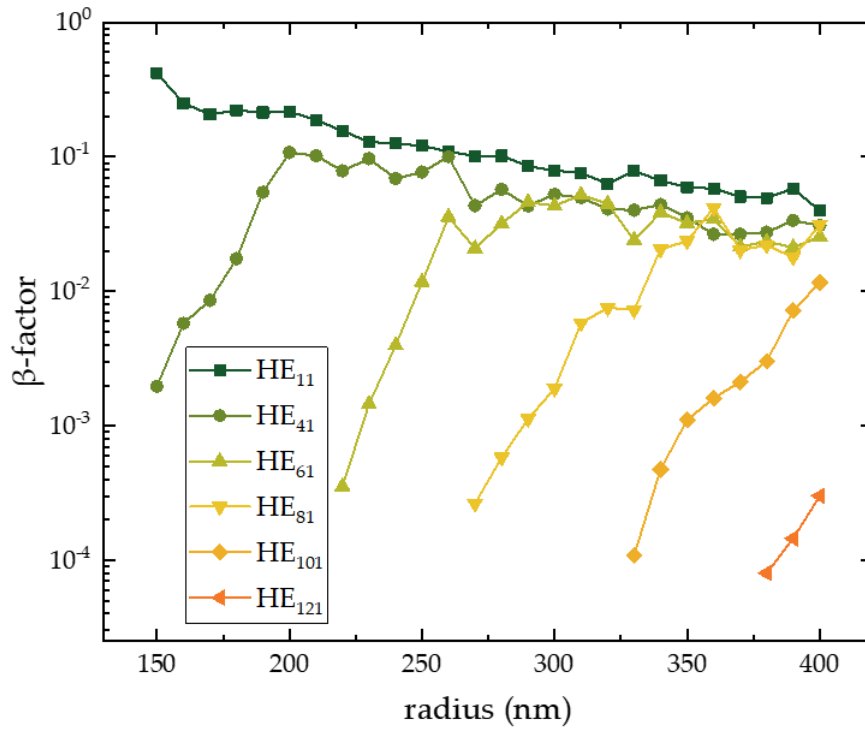
FIGURE 4.5: The spontaneous emission factor β of randomly oriented dipoles to the modes depicted in figure 4.2 in an infinitely long loss-less InP NW as a function of radius *r*. A mode with a β-factor of 1 corresponds to a 100% energy emission from the dipole to that mode.

At open-circuit conditions, randomly distributed dipoles inform us about the average spontaneous emission into certain modes, because charge carrier diffusion allows radiative recombinations anywhere in the NW.[122] In that reasoning, the assumption is made that the emission occurs with equal chance throughout the structure since diffusion of charge carriers is assumed to be random. However, charge carriers may diffuse to locations where the LDOS is high, because the concentration of electrons and holes is relatively low there, but this has not been verified experimentally yet. It is instructive to see what the maximal values of β-factor are for each mode and for each polarization angle. We expect to find that the coupling to a mode is maximal if a dipole is placed on a location where the mode's electric field strength is highest.[129]

From figure 4.3, we see that a NW with a radius $r = 260$ nm allows emission from the two WGMs HE_{41} and HE_{61}. From figure 4.4, we see that these two modes have effective indices in the range that Schmitt *et al.* have measured.[18] Lastly, from figure 4.5, we see that these modes already have respectable β-factors ($\approx 0.05 - 0.10$) for random dipole distributions. For this radius $r = 260$ nm, the *x*-, *y*- and *z*-components of the electric field strengths of these two WGMs (HE_{41} and HE_{61}) as well as the fundamental mode HE_{11} are determined. For each component of the E-field of each mode, a line is drawn from the center to the edge of the NW that crosses the point where the electric field strength is maximal. The β-factor is calculated for dipoles that are placed on points along this line which are polarized in the direction parallel to the E-field component. In that way, we expect to retrieve the maximal coupling for each dipole polarization and mode. The results are shown in figure 4.6.
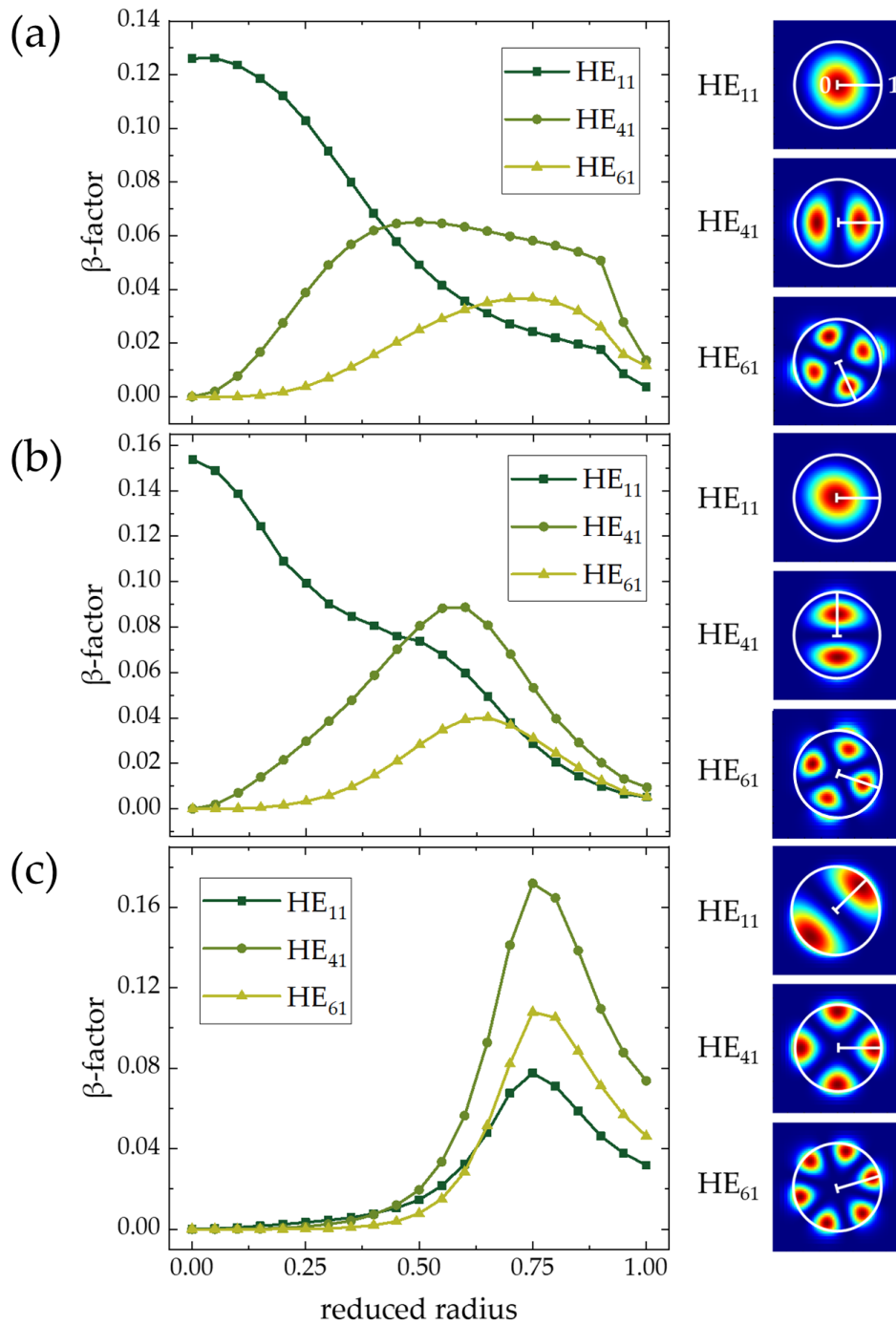
FIGURE 4.6: β-factors of the HE_{11}, HE_{41} and HE_{61} modes for single dipoles with strictly *x*-polarization (a), *y*-polarization (b) and *z*-polarization (c) as a function of the reduced radius inside infinitely long lossless InP NWs. The E-field distribution for each mode and polarization from (*x,y*)-cross-sections of the structure are visualised in the right column, where the white circle indicates the NW circumference. The straight white lines inside the NW indicate where the dipoles are placed from the center to the NW radius. The lines are chosen such that they cross the maximum E-field density of each polarization for each mode.

We introduce a variable called the reduced radius which ranges from 0 to 1, where 0 corresponds to the center of the NW and 1 corresponds to radius *r*. In figure 4.6 (a), we observe negligible emission in the WGMs from dipoles placed in the NW center, where most of the dipole energy is emitted through the fundamental mode. For both WGMs, the β-factor increases along the line and reach a maximum value for the reduced radius that is on top of the maximum E-field. For even higher reduced radii, the coupling to the WGMs drops similarly to the drop in the E-fields, and for the two outermost dipole positions the coupling drops harshly. This harsh interrupting drop for all three modes is attributed to the fact that for those dipole placements, a considerable portion of the dipole energy is directly injected outside of the NW radius. Therefore only a portion of the dipole energy is injected inside the NW and contributes to the β-factor. We see similar behaviour in figure 4.6 (b). The coupling from a centered *y*-polarized dipole to the fundamental mode is slightly higher than for an *x*-polarized dipole, as well as the maximal coupling into the HE_{41} mode. Overall the β-factor more closely scales with the E-field strength.

For the *z*-polarized dipoles shown in figure 4.6 (c), the E-fields are much different compared to the two other polarizations. As we see from the E-field plots, all three modes have negligible E-fields inside the NW core. Therefore we see that the β is minimal there for all three modes. Similarly, they all reach a maximum coupling at the same reduced radius = 0.75, which corresponds well with the E-field distributions. Furthermore, we find that the maximum value of β is higher for both WGMs in the *z*-component plot compared to the *x*- and *y*-component plots, indicating that the coupling from a dipole to the WGMs is highest using a *z*-polarized dipole at a position 0.75 *r*, aligned with the E-field maxima. Note that this is the case for a straight infinite wire, and that in reality the β-factors are different for finite wires.

Overall, the β-factors of maximally 17% are much lower than the spontaneous emission factors reported by other researchers: 68%,[122] 89%,[130] 90%,[129] or even 95%,[85] but these are all for coupling into the fundamental mode HE_{11}. As we've seen in figure 4.5, the β-factor is highest for the fundamental mode, especially for small NW radii. Moreover, these researchers optimized the structure geometry to essentially allow only a single guided mode; the fundamental mode HE_{11}.

4.3   Quality factors of tapered nanowires

So far, only straight NWs have been analyzed. In Chapter 2, we have already discussed the promise of tapered NWs in researches by Schmitt,[18,115,116] Seo,[19,114] Friedler,[85] and Gregersen.[89] Most importantly, we would like to know if the choice of tapering orientation results in different photonic behaviour, like Seo *et al.* have found in their research.[19] Therefore, the Q-factors of tapered NW resonators are simulated. Since the resonances can be hosted throughout the entire structure,[18] and we do not know where the resonance frequencies reside inside the structure prior to the simulation, we make use of a dipole cloud technique.[118] On random locations within the structure, randomly polarized dipoles are placed to best excite all available modes. Similarly, randomly placed time monitors record the electric fields over time, which are used to determine the resonances and their Q-factors numerically according to the theory explained in Chapter 3. The resulting Q-factors are averaged for comparison between the structure geometries. The time monitors use start apodization: a feature which is useful for filtering away short lived transients that occur in the first ≈ 150 fs when studying high Q systems that decay very slowly.

A single InP NC is simulated with a height 2.5 μm, tapering angle 2.4° as a function of the middle radius r_{mid} in the range 60-400 nm. The variable middle radius $r_{\mathrm{mid}} = (r_{\mathrm{top}} + r_{\mathrm{bottom}})/2$ is introduced since the top and bottom radii of a NC are not identical, yet its variable r_{mid} remains the same regardless of NC orientation (normal or inverse) if the NC height is not changed. We have previously pointed out that researchers have placed NW arrays covered in PDMS on a reflective mirror to enhance both the absorption and emission.[24,25] Therefore, simulations where the NC is placed on a mirror while covered in PDMS are also performed. The results of these simulations are shown in figure 4.7.
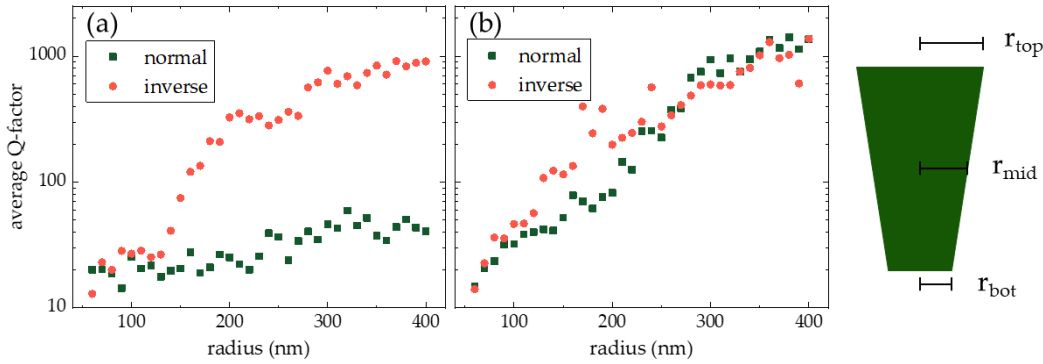

FIGURE 4.7: Average Q-factors of positively/negatively tapered lossless InP NWs (normal/inverse NCs) on a substrate (a) and on a reflective silver mirror (b) as a function of the middle radius r_{mid}. The Q-factors for normal NCs are enhanced when placed on a mirror compared to when they are on a substrate, whereas the Q-factors of inverse NCs are similar in both cases. The middle radius $r_{\mathrm{mid}} = (r_{\mathrm{top}} + r_{\mathrm{bottom}})/2$ is visualised on the right.

We see from figure 4.7 that in general, NCs with a larger radius have a higher Q-factor. This can be attributed to the fact that the effective indices n_{eff} of all modes increase with radius (like we have seen in figure 4.3), thus confining photons better, resulting in a higher cavity photon lifetime τ_{ph} and Q-factor.[13] However, a larger bottom radius increases the transmission to the substrate,[9,117] reducing the photon lifetimes and limiting the Q-factor. As we have seen in figure 2.17, the combined WGM and FP modes inside NCs tend to radiate towards the side with the largest facet radius.[18,19] This is verified by figure 4.7 (a), where we see that the Q-factors for normal NCs are significantly lower than for inverse NCs at large radii. This difference in Q-factors can be attributed to the difference in bottom radius and the resulting losses to the substrate. At low radii, the Q-factor is not only limited by the bottom radius, but also by the top radius. At these low radii, the mode effective indices n_{eff} of the available modes are low, indicating bad photon confinement. Furthermore, wee see from figure 4.7 (b) that the substrate losses of normal NCs can be counteracted by a reflective mirror, indicated by similar Q-factors for both NC orientations at large radii. This becomes even more apparent if the resonance spectra of the setups are compared. For a radius $r_{\mathrm{mid}} = 350$ nm, the resonance spectra of the four distinct setups (normal/inverse NCs on a substrate/mirror) are shown in figure 4.8.
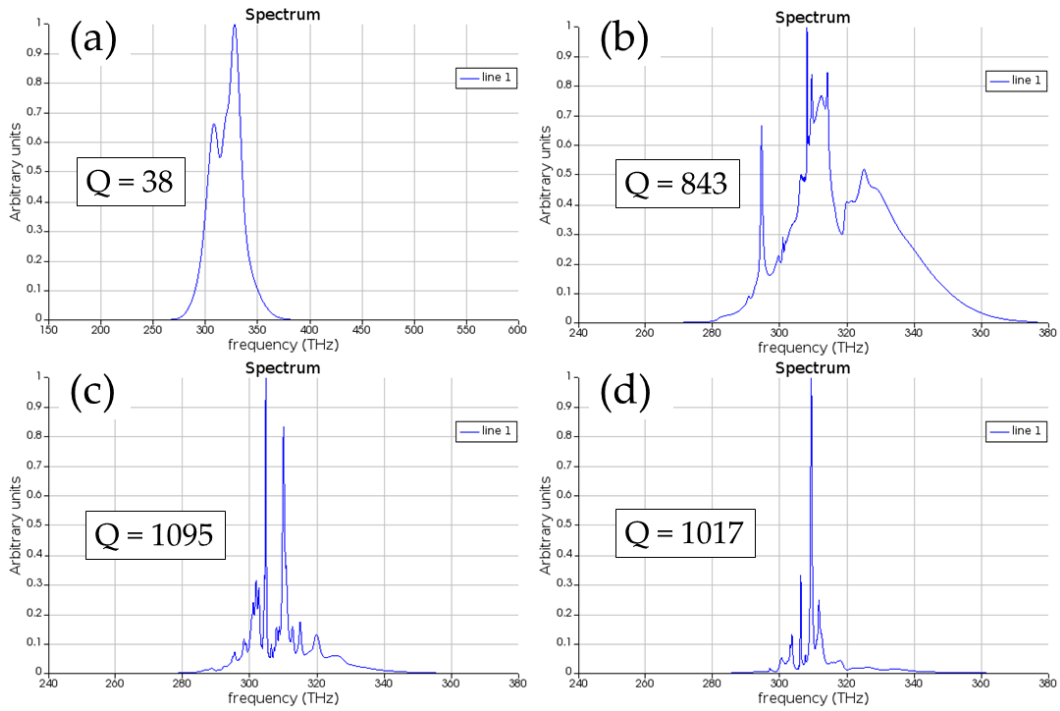
FIGURE 4.8: The resonance spectra of normal (a) and inverse (b) NCs on substrate, and normal (c) and inverse (d) NCs on a mirror with a radius $r_{mid} = 350$ nm. Their average Q-factors from figure 4.7 are displayed.

We observe in figure 4.8 that the spectral shapes differ significantly for the NCs on substrate. Whereas both figures 4.8 (a) and (b) show a relatively broad range of resonance frequencies, the inverse NCs on substrate shows distinct peaks with high Q-factors ($\approx$ 1000). Both 4.8 (c) and (d) show a more narrow bandwidth and even sharper peaks, resulting in slightly higher Q-factors. Note that the resonance frequencies throughout the structures are not fixed, even though the geometries are very similar. This may be an indication of the complex interplay of WGMs and FP modes. Several anomalous high Q-factors are found in the simulations that exceed the average Q-factors by a factor 3-4. We expect these Q-factors to be indicative of resonant WGMs in the structure, but this needs to be verified. Therefore, we take a look at the electric field distributions inside the NCs simulated in figure 4.7 (b). The electric field cross-sections are shown in figure 4.9.

We observe that the normal NC does not show a distinct resonance frequency, but rather a bandwidth of weakly confined frequencies (as we expect from figure 4.8 (a)). More importantly, no resonant WGMs are found inside the structure. However, for the inverse NC a multitude of resonant WGMs are found at discrete heights, similar to results by Schmitt *et al.* (shown in figure 2.17).[18] These high Q WGMs all show a long but less intense branch towards the top facet of the structure, indicating a connection to a FP between the WGM and the top facet. In figure 4.8 (c), we see a resonant HE_{101} mode which resides at a certain height, 'leaking' upwards in such a branch. A second monitor near the top facet verifies that the photons are still mostly confined in the HE_{101} mode at the same initial resonant frequency, where a small portion of the photons has moved radially outward. Most importantly, all of the sharp peaks in the resonance spectra of 4.8 can be assigned to one of these WGMs.
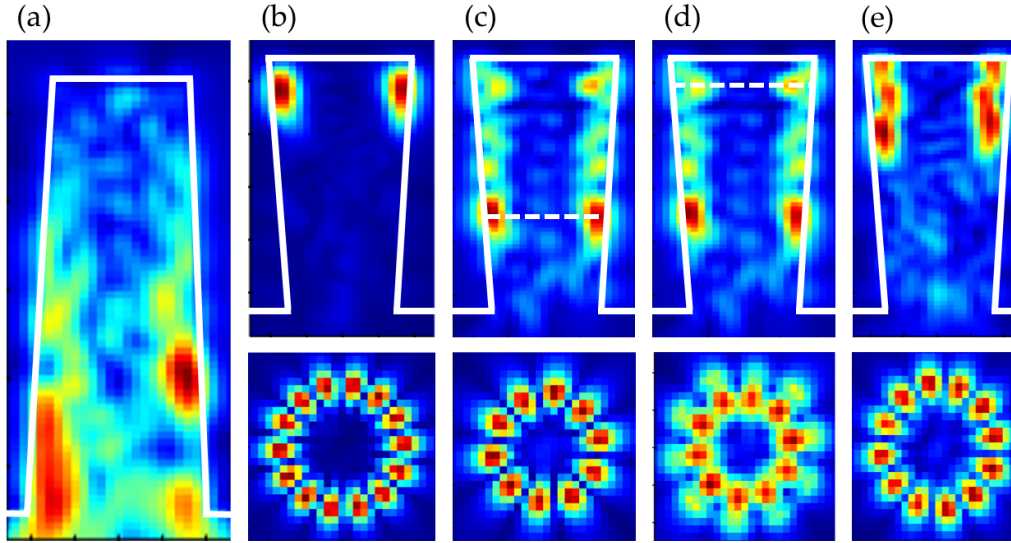
FIGURE 4.9: Electric field distributions inside a normal NC (a) and inverse NC (b)–(e) on a substrate with height 2.5 µm and $r_{mid} = 350$ nm. Thick white lines indicate the structure boundaries. (a) The normal NC with low Q-factor shows no single distinct resonant mode and significant losses to the substrate. (b) An (x,z)-cross-section (top) and (x,y)-cross-section of the inverse NC showing a resonant HE_{141} WGM. (c) and (d) are cross-sections of a resonant HE_{101} WGM. The dashed lines indicate where the (x,y)-cross-sections are placed. The cross-section of (d) shows that the photons move upward through the same HE_{101} WGM, spreading slightly in the outward radial direction. (e) Cross-sections showing a resonant HE_{121} WGM.

Now, it is instructive to investigate the influence of the NC height, because it changes the resonance conditions for the FP modes but should leave the resonance conditions of the WGMs unaffected.[19] The NC height is changed without affecting the tapering angle or transmission to the substrate, to isolate the resonance factors that depend strictly on the NC height. Therefore the Q-factors are now plotted as a function of the bottom radius r_{bot}, because the top radius r_{top} – and through it, the middle radius r_{mid} – changes when varying the NC heights. The results for a range of bottom radii and a range of NC heights (1.5–3.5 µm) are shown in figure 4.10.

We observe that regardless of NC height, the Q-factors of NCs with a small bottom radius are quite low. As mentioned before, this is attributed to the bad confinement of the optical modes at these radii signified by their low mode effective indices. As the bottom (and top) radius increases, the Q-factor also increases, up until a certain radius where the Q-factor either saturates or decreases for larger values. Furthermore, we see that there are no clear advantages or disadvantages for a NC height smaller or greater than 2.5 µm regarding the confinement of light. Note that these simulations are performed with suppressed absorption, while in reality there will be advantages and disadvantages to changing the height of the structure through the absorption coefficient. For example, the absorbance of a NC solar cell increases with the NC length,[22] but NCs cannot be made arbitrarily long. For longer wires in an axial junction NW solar cell, current can only be generated efficiently with very long minority carrier diffusion lengths.[28] This can be realized by increasing the diameter,[117] but this changes the resonance conditions of the structure altogether.
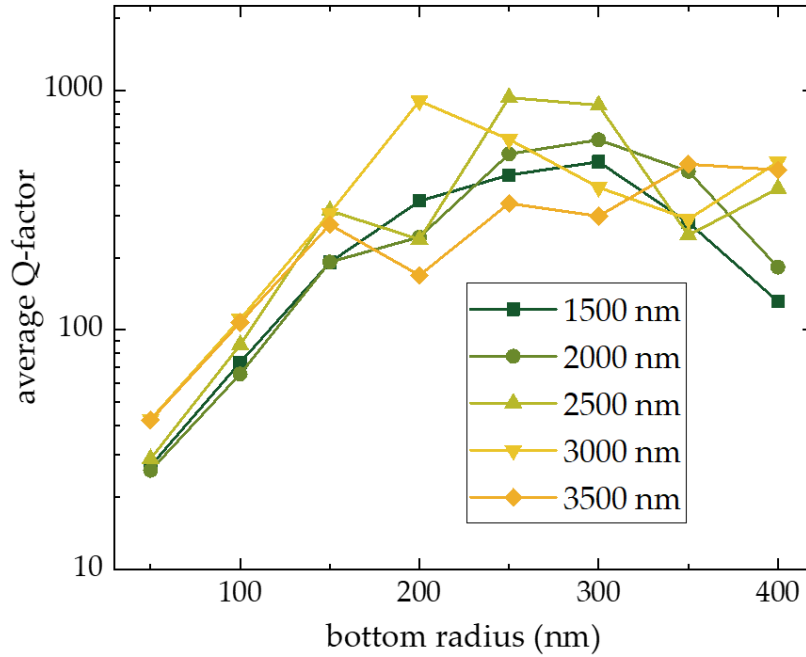
FIGURE 4.10: Average Q-factors of single inverse lossless InP NCs on a substrate as a function of their radius for various NC heights. All NCs have the same tapering angle, and the indicated radius is the bottom radius $r_{bot} < r_{top}$ of the facet meeting the substrate.

In figure 4.10, we observe a maximal average Q-factor for bottom radii in the range 250–300 nm for a NC height of 2.5 μm. This range corresponds to a middle radius in the range of approximately 300–350 nm, which is a range that is interesting for a study of WGMs (as seen in figures 4.3, 4.5 and 4.7). Additionally, the choice of a NC height of 2.5 μm satisifies the dual relation between a high absorptance and a low minority carrier diffusion length.[22,28] The NC absorbs the majority of light in the first 2.5 μm and any increase in length would only decrease the ability to extract useful charge carriers in an operating solar cell using these NCs. So even though the increase in length would increase the total absorptance slightly,[117] the short minority carrier diffusion length would counteract this by decreasing the charge carrier extraction efficiency.

Most importantly, since there is no conclusive (dis-)advantage to both an increase and a decrease in length of the 2.5 μm NCs with regards to the Q-factor of the resonant modes inside, we can rule out the fact that the enhanced emission from NCs depends on the quality of the FP mode. This has already been discussed in section 2.4.3, by hypothesizing that the FP mode need not have a high Q-factor to explain the enhanced emission from the coupled WGM and FP modes in NCs.

4.4 Calculating the photon escape probability

In the calculations of P_{top} and P_{bot} the electric fields and the absorption in the structure need to be integrated over a polar and an azimuth angle range. However, we approximate their value with a finite number of simulation using a finite step-size that is computationally still feasible. Therefore, both θ and ϕ are changed from $0°$ to $85°$ in steps of $5°$. This is done for two polarizations separately, TE and TM plane waves, and for the two directions separately, from the top and from the bottom. This way, one setup requires 1156 simulations for an approximation of the photon escape probability. This is still manageable, but any further increase in angular resolution would require more computational power or time. The absorption inside the structure is obtained by an absorption analysis group, which combines an index monitor and electric field monitor and then calculates the absorbed power P_{abs} using[131]

$$P_{abs} = \frac{\varepsilon_0 \cdot \omega}{2} \int_V \text{Im}\left(\varepsilon(r)\right)\left|E(r)\right|^2 dV \tag{4.3}$$

We performed these simulations for the three setups shown in figure 3.3: the inverse NC, normal NC and a reference planar equivalent. We chose a NC height of 2 µm, middle radius of 250 nm and a NC pitch of 800 nm: these were also the dimensions of our third experimental sample. The photon escape probability is calculated as

$$P_{esc} = \frac{P_{\text{top}}}{P_{\text{top}} + P_{\text{bottom}}}. \tag{4.4}$$

For a source wavelength of $\lambda = 922$ nm, the values of P_{esc} are 0.66, 0.48 and 0.19 for the inverse NC, normal NC and the planar equivalent respectively. Immediately we can conclude that both NC orientations increase the photon escape probability with respect to their planar equivalent. As discussed at great length in Chapter 2, this is expected for NW and NC structures. Moreover, the inverse NC better directs its emission to the top hemisphere than a normal NC does, most probably because of lower energy losses to the substrate. To better understand the obtained values for the photon escape probability, we should observe the effect they have on the overall external radiative efficiency η_{ext}^{PL}. We reiterate equation 2.16:

$$\eta_{ext}^{PL} = \frac{\eta_{int}^{PL}\overline{P_{esc}}}{1 - \eta_{int}^{PL}(1 - \overline{P_{esc}})}, \tag{4.5}$$

which holds for all values of the internal radiative efficiency η_{int}^{PL}. Using the obtained values of the photon escape probabilities of the different structures, the external radiative efficiency is plotted as a function of internal radiative efficiency. The plot is shown in figure 4.11. The current world record for the highest photon escape probability for an InP cell (97%)[132] is added too for comparison. We see that the photon escape probability has a large effect on the external radiative efficiency. Miller and Yablonovitch note[57] that the photon extraction process in a solar cell should be the main focus when pursuing the Shockley-Queisser limit. However, they add that photon extraction is very demanding on material purity, structure geometry and photon management throughout. A structure that is 99% defect free already has half the total efficiency of a structure that is 100% defect free.[57] This should be taken into consideration when leaving simulations behind and entering experimental setups.
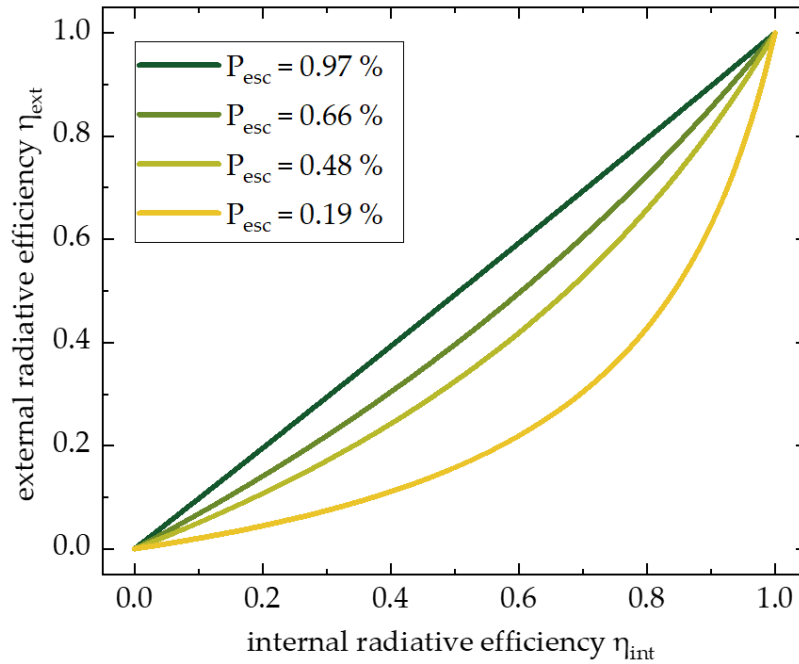
FIGURE 4.11: The external radiative effiency as a function of the internal radiative efficiency for a number of photon escape probabilities. The three lowest values for P_{esc} correspond to the inverse NC, normal NC and planar equivalent simulations, the highest value corresponds to the current world record for an InP cell.[132]

4.5   Absorption in tapered nanowires

In the calculations of the photon escape probabilities, we do not take into account any difference in absorption between different tapered structures. There might be structures that exhibit lower photon escape probabilities than others, but if their overall absorption from incident solar radiation compensates for this, they could still be of interest for photovoltaic applications. The Lorentz reciprocity model that is used to obtain the photon escape probabilities requires absorption inside the cavity to calculate the enhancement of the electric fields inside, as we can see in Appendix B. The InP material with suppressed extinction coefficient was used, since the absorption needed to be kept low for the underlying model to work. This is justified in both Appendix A and B. In reality, the absorption coefficient of InP is significant, especially below and close to the bandgap wavelength. Therefore, it is instructive to investigate the difference in absorption of inverse and normal NCs under different lighting conditions, this time using the realistic (complex) material database values for InP. A similar NC geometry as for the photon escape simulations is used: with a height of 2 μm, middle radius of 250 nm, tapering angle 2.4° and various pitches. The absorption is calculated for incident radiation either with the solar spectrum or with the laser spectrum of our experimental setup ($\lambda = 532$ nm). This is done because these NC geometries have also been fabricated for experimental analysis using the optical setup. The results are shown in figure 4.12.

We observe that the absorption decreases as the pitch increases. This is caused by a decrease of the area coverage of the NC absorption cross-sections (visualised in figure 2.9). For the same reason, we see that the absorption saturates around a pitch of
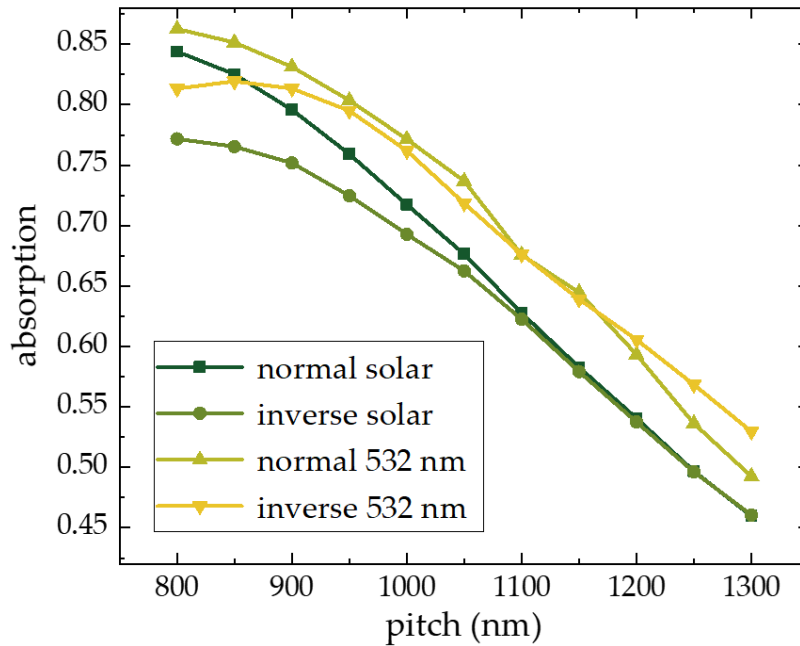
FIGURE 4.12: Simulated absorption of InP NC arrays with a height of 2 μm, middle radius of 250 nm, tapering angle of 2.4° as a function of the NC pitch. The absorption is simulated for the two NC orientations and for two excitation conditions, solar radiation and laser radiation. The absorption is given as a fraction of the incident power.

800 nm, where the individual NCs cover the entire array area with their absorption cross-sections. Furthermore, we observe that the NCs absorb a higher fraction of the source power from a 532 nm laser than from the solar spectrum. A lot of the energy in the solar spectrum is stored in photons with an energy higher than the bandgap of InP, but still a considerable amount of photons are not absorbed by the material. The 532 nm photons all have a higher energy than the bandgap and therefore a larger fraction of them is expected to be absorbed than for the solar radiation.

Most importantly, we see that the absorption is higher for the normal NC orientation than for the inverse NC orientation, most considerably at lower pitches. This is attributed to the top facet reflection, which is in general higher for inverse NCs than for normal NCs because of the difference in top diameter. The increased reflection and lower absorption weigh heavier at lower pitches because the total top facet area constitutes of a larger fraction of the total array area than for larger pitches. As the pitch increases further, the absorption of the NC array approaches the absorption of a planar layer and we lose the benefits of nanophotonic confinement of modes for absorption and emission (the benefits discussed in section 2.3.1).

Lastly, the absorption also depends greatly on the NC radius. Earlier in this Chapter, we have seen that too small diameters do not allow the existence of our modes of interest, and that more modes are allowed the larger the diameter gets. However, a too large top facet significantly increases the reflection. We performed simulations on the same NC geometries as before, now with varying radii and for two different pitches to see their difference. We used the same laser radiation as the previous simulation, because figure 4.12 shows the absorption is highest and because it is also used in the experimental setup. The results are shown in figure 4.13.
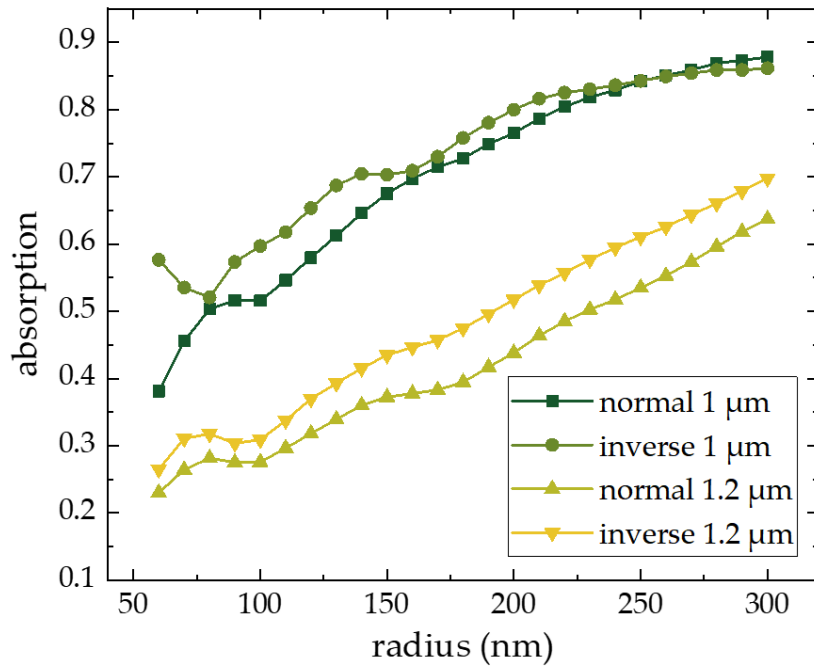
FIGURE 4.13: Absorption of InP NC arrays with a height of 2 μm and tapering angle of 2.4° as a function of the NC middle radius. The absorption is simulated for the two NC orientations and for two pitches, 1 μm and 1.2 μm. The absorption is given as a fraction of the incident power, and the source wavelength is 532 nm.

As expected, the absorption increases as the radius increases. A larger volume of the solar cell consists of the absorbing material InP. For the 1 μm pitch geometry we see that the absorption reaches a saturation for the highest NC radii, whereas for the 1.2 μm pitch geometry we see that the absorption is still increasing. This is because at the highest radius, the 1 μm pitch geometry has already reached its optimal absorption cross-section configuration whereas the 1.2 μm pitch geometry has not (again, as depicted in figure 2.9). Overall, the absorption is lower for the larger pitch, which is in line with the findings of figure 4.12. However, in these simulations the absorption by the inverse NCs was found to be higher than the absorption by the normal NCs, which is most clear for the 1.2 μm pitch geometry. In the next Chapter, NCs with this pitch of 1.2 μm will be measured, and figure 4.13 helps understand the experimental results.

Chapter 5

Photoluminescence measurements

In this section, the results of the experiments performed for this thesis are shown. First, the nanowire sample fabrication and PDMS application and removal are performed for several nanowire geometries. Then, the photoluminescence measurements are performed on those samples, and their spectra are analysed.

5.1 Nanowire array fabrication

The PDMS recipe by Standing *et al.* is optimized for NWs with diameters of 25–100 nm, lengths of 10 μm and pitches ranging from 0.2 to 1.5 μm.[20] These NWs are very needle-like, and more research has been devoted to their applications.[11,25,66] However, for our research we are interested in a different range of parameters. For a coupling between the WGM and FP modes to exist, the NWs have to very pillar-like:[18] the ratio between the diameter and length of the NWs ideally obeys $D/L \geq 0.4$, a geometry which has been researched more often too.[19,64,65] In Chapter 4 we have seen that the minimal diameter for which InP NWs host WGMs is 318 nm: this should therefore be the minimal NW diameter throughout the fabrication and optical characterization. Long Nws with such a width would exhibit a considerable amount of nonradiative recombinations because of a large active volume, but short NWs may not experience enough support from the PDMS layer when they are removed from the substrate. A NW length of 2.5 μm and NW pitch of 1 μm were chosen to maximize absorption while keeping the length below the critical minority carrier diffusion length.[22,28] An image of the sample was obtained using a scanning electron microscope (SEM), which can be seen in figure 5.1 (a).

The sample was covered in PDMS following the aforementioned recipe and we attempted to remove the NWs. However, the transfer yield, the percentage of NWs transferred into the layer of PDMS, was very low. In figure 5.1 (b), an SEM image of the substrate after the attempted PDMS removal can be seen. The NWs could not be removed using a single slicing motion, so instead, a rocking motion was used. This is clearly visible from the SEM images, in which a large part of the NW field can still be seen unaffected. Figure 5.1 (c) and a close-up of that image, figure 5.1 (d), show what had happened at the surface. NWs embedded in PDMS have been removed from the substrate locally, but they have not been transferred into the PDMS layer successfully. The combination of large bottom diameters and short lengths ensured that the NWs experienced too little support from the PDMS when the PDMS removal took place.
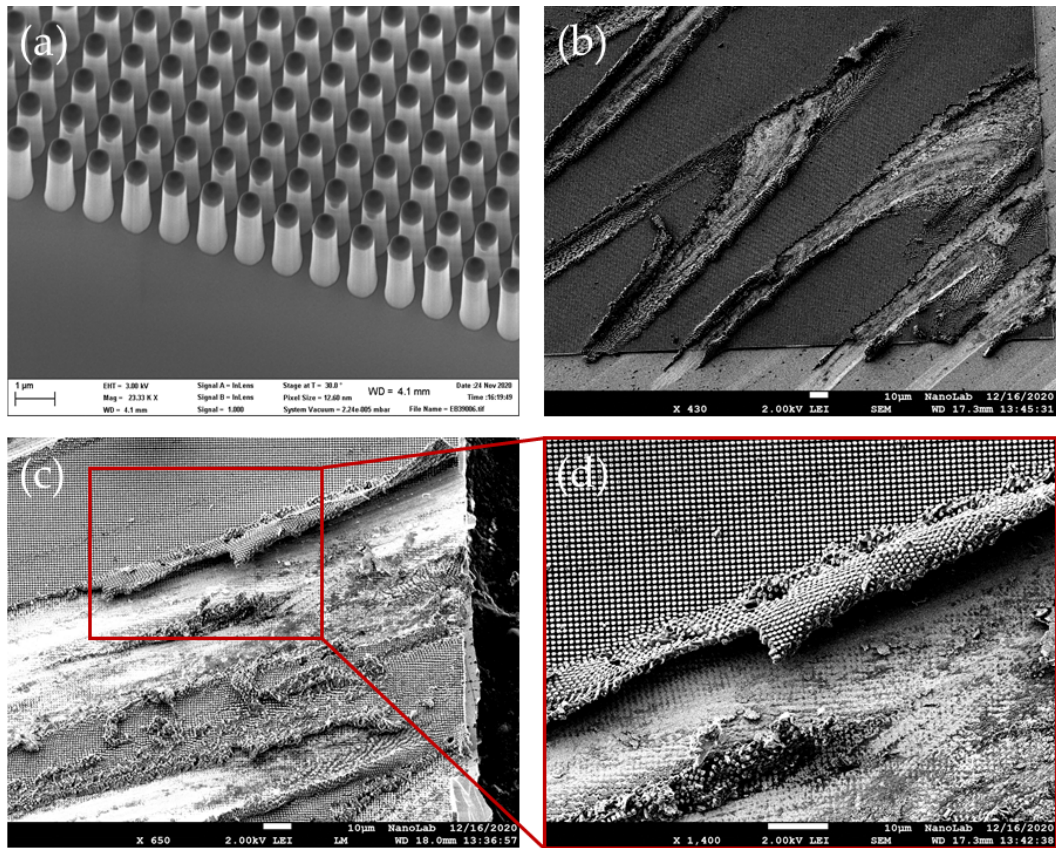
FIGURE 5.1: SEM images of an InP NW array. (a) The NW field with top (bottom) diameter 630 (820) nm, length 2.5 μm and pitch 1 μm. (b) The unsuccessful NW extraction is characterized by a zigzag motion of the razor blade across the surface. (c, d) Close-ups of the NW field after the attempted PDMS removal, indicating that the majority of NWs has not been removed. Upon further inspection, the PDMS keeps the NWs together but it is not strong enough to fully detach the NWs from the substrate.

A second sample was prepared to secure a higher transfer yield from the PDMS removal. This sample was larger than the previous one in every aspect; the top and bottom diameters, NW length and NW pitch were all increased. An SEM image of this sample can be seen in figure 5.2 (a). This sample too was covered in PDMS and we again attempted to remove the NWs from the substrate. For this sample, the transfer yield was close to 100%, as not a single NW could be found on the substrate after the PDMS removal. An SEM image of the substrate can be seen in figure 5.2 (b), where the substrate has been cleaved through the former NW field. Little remains of the PDMS can be seen, and the NWs have been removed successfully with minimal variations in length. This indicates that the PDMS successfully occupied the space between the NWs and it proved sturdy enough to support the NWs once removed. This time, the PDMS removal succeeded using a single slicing motion rather than a rocking motion, which appeared to work better. Fragments of the PDMS layer with embedded NWs were placed on a mirror; some of them in a normally tapered orientation and some in an inversely tapered orientation, as seen from above. An ordinary microscope was used to investigate these fragments and make images of them, which are visualised in figure 5.3.
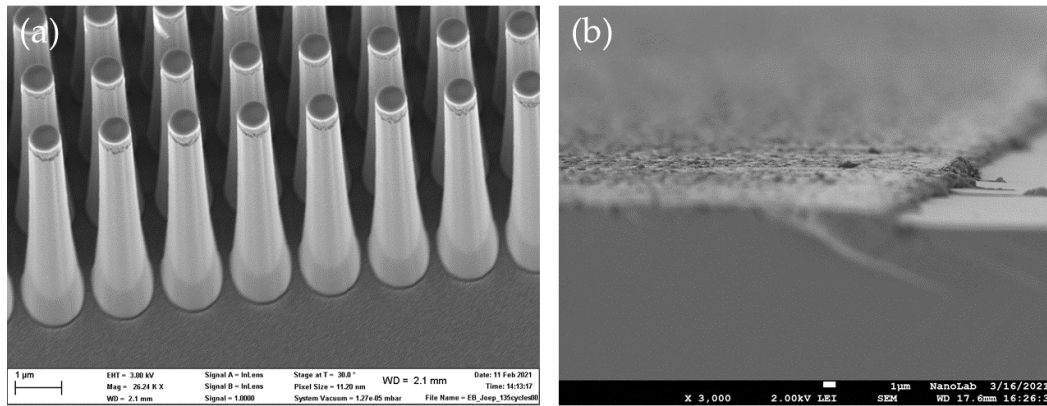
FIGURE 5.2: SEM images of the 7 µm NW array. (a) The NW field with top (bottom) diameter 740 (1290) nm, length 7 µm and pitch 1.5 µm. (b) After the PDMS removal, the NW field was cleaved through the middle, yielding a cross-section where the edge between the former NW field and the substrate is clearly visible. The NW extraction is successful, as there are no NWs left on the substrate.

FIGURE 5.3: Microscope images of the 7 µm NWs in PDMS. (a, b) Top view and close-up of inversely tapered NWs in PDMS. The high transfer yield of the NWs is apparent from the transferred square array inside the PDMS. (c, d) Top view and close-up of normally tapered NWs in PDMS. Part of a square array can be seen.

The square NW arrays can be easily distinguished from the PDMS layer. Figure 5.3 (a) and (b) are top views of inversely tapered NWs and figure (c) and (d) are top views of normally tapered NWs. The distinction can be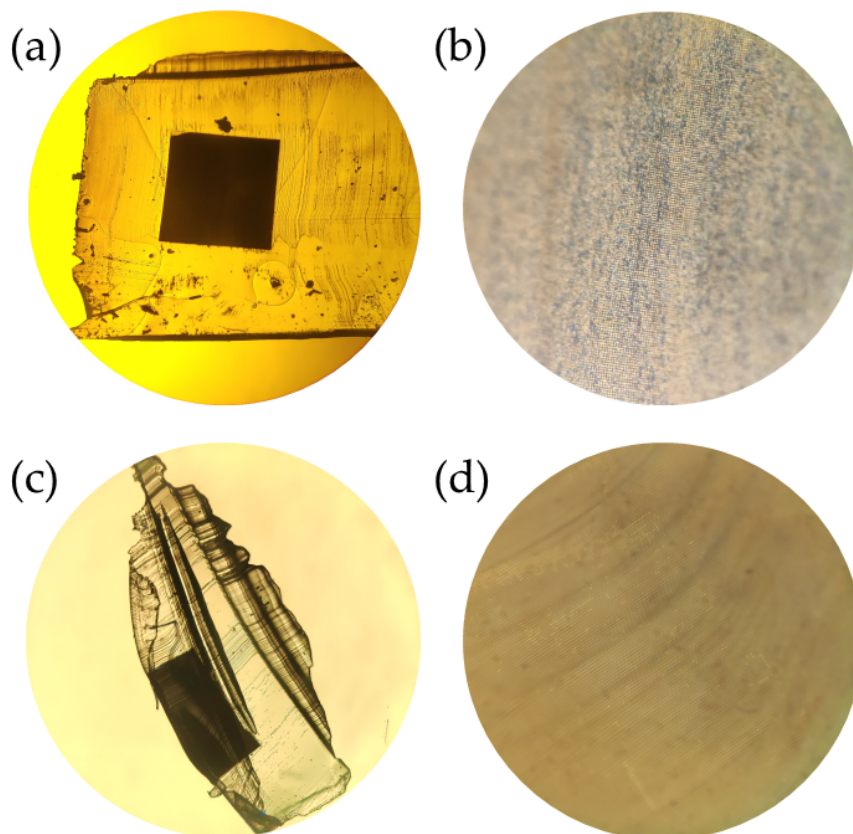 made from the close-ups. In figure 5.3 (b), a direct view of the NW bottom diameters is given, with the PDMS around and underneath the NWs as seen from above. Each dark spot corresponds to a NW because they absorb the backlight, the light regions indicate the regions with PDMS. In figure 5.3 (d), the NW top diameters are visible, but the vision is tempered by the PDMS layer above it. In either case, individual NWs can be distinguished because of their large geometry. These samples are ready to be measured using the optical setup.

A third and last sample was prepared to find the middle ground between the two first samples. We would like to investigate NWs with a length in the range of 2 - 2.5 μm with diameters that allow at least the three lowest order WGMs that can still be extracted from their substrate using the PDMS removal. That's why this third time, three different pitches (0.8, 1 and 1.2 μm) were prepared to obtain the lowest pitch that could still be removed. Note that these are structures whose absorptions have been investigated already, shown in figure 4.12. Pictures of the sample are shown in figure 5.4.
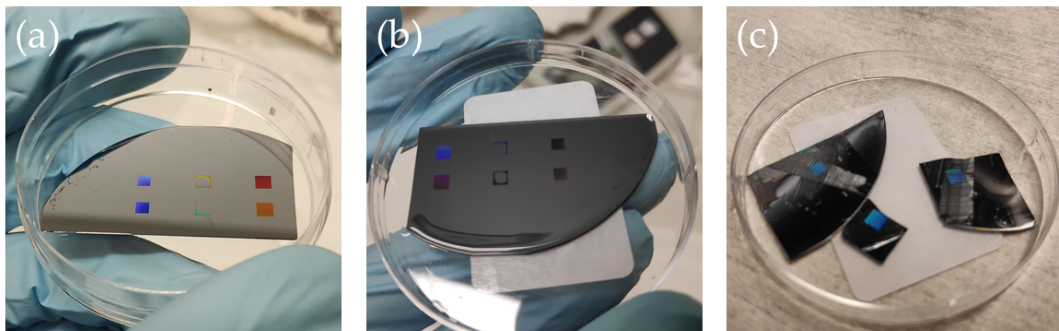

FIGURE 5.4: Photographs of the 2 μm NW samples. (a) Six fields with NWs can be found on the substrate, where the two rows are identical but each column is a different pitch. From left to right, the pitches are 0.8 μm, 1 μm and 1.2 μm. (b) In this picure, before the PDMS curing, it is clear that the arrays with pitch 1 μm show an anomaly in the center of the NW fields. (c) Reflections show that there are still NWs on the substrate for the 1.0 and 1.2 μm pitch NW fields after the PDMS removal.

The sample was again covered in PDMS and we attempted to remove the NWs. The two fields with the smallest pitch (the left column in figure 5.4 (a)) were not successfully transferred into the PDMS. This is attributed to the combination of short NW length, large NW bottom radius and small pitch, resulting in insufficient support from the PDMS. The two fields with the pitch of 1 μm in the middle column were processed in the same way, but there did not seem to be a high density of NWs in the first place. Our colleague who etched the NWs also questioned if there were any wires in the first place, and could not explain what was wrong with the sample. Unfortunately, we have not obtained SEM images for these NWs. Fortunately however, the PDMS removal for the rightmost column, with the NWs with a pitch of 1.2 μm, was successful. The middle and right NW arrays in figure 5.4 (c) correspond to this process. That picture shows that a significant amount of NWs was left at the

substrate, but inside the PDMS, a considerable amount of transferred NWs could be seen too. These PDMS fragments with embedded NWs were again placed on a mirror in both orientations, and they were investigated with a microscope. Microscope images are shown in figure 5.5.
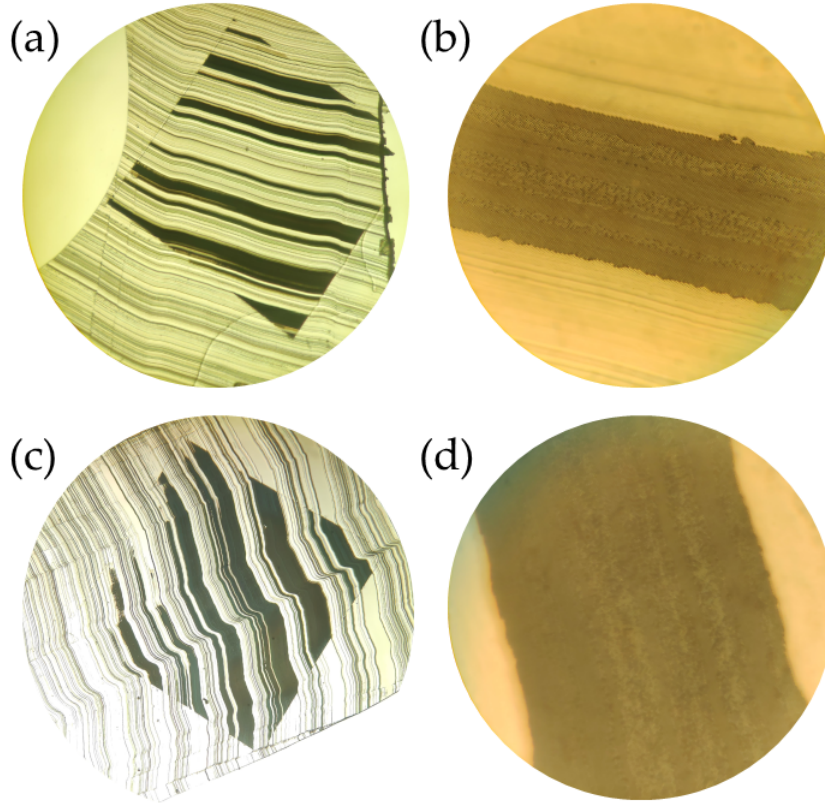

FIGURE 5.5: Microscope images of the 2 μm NWs in PDMS. (a, b) Top view and close-up of inversely tapered NWs. The contours of the square NW array are clearly visible and strips of NWs have been transferred into the PDMS. (c, d) Top view and close-up of normally tapered NWs. Part of a square array can be seen.

Very similarly to the images in figure 5.3, the contours of the square NW arrays can be clearly seen in figure 5.5. The transfer yield for the third sample is clearly lower, depicted by the regions inside the square field that are clear and transparent. The close-ups show that locally, strips of NWs have been extracted with a high yield, ensuring that these samples can be used for examination with the optical setup.

A summary of the fabricated sample geometries is given in table 5.1. Note that the tapering angle slightly varies because of the differences in pitch, length and diameters. In the following section, the sample numbers are indicated.

TABLE 5.1: An overview of the dimensions of the three samples.

Sample no.	d_{bot} (nm)	d_{top} (nm)	length (μm)	pitch (μm)	tapering angle
1	820	630	2.5	1.0	2.2°
2	1290	740	7.0	1.5	2.3°
3	700	530	2.0	0.8-1.0-1.2	2.4°

5.2 Photoluminescence results

It is important to mention that the PL measurements performed for this thesis have produced only preliminary results, and that more time and measurements are required to provide conclusive results. This will be discussed at the end of this section.

The first sample, shown in figure 5.1, was not successfully transmitted into the PDMS after performing the PDMS removal. The SEM-images clearly show that the majority of NWs is still attached to the substrate. Therefore no comparison can be made between these NWs in a normal orientation or inverse orientation. However, the PL of this sample has been measured before the PDMS removal took place, and its PL spectrum serves as a good reference for this section. All the spectra in this section have been normalized to their exposure time to the excitation source. This ensures that a realistic comparison between the different structure geometries and orientations can be made. The PL signal of the first sample is shown in figure 5.6.
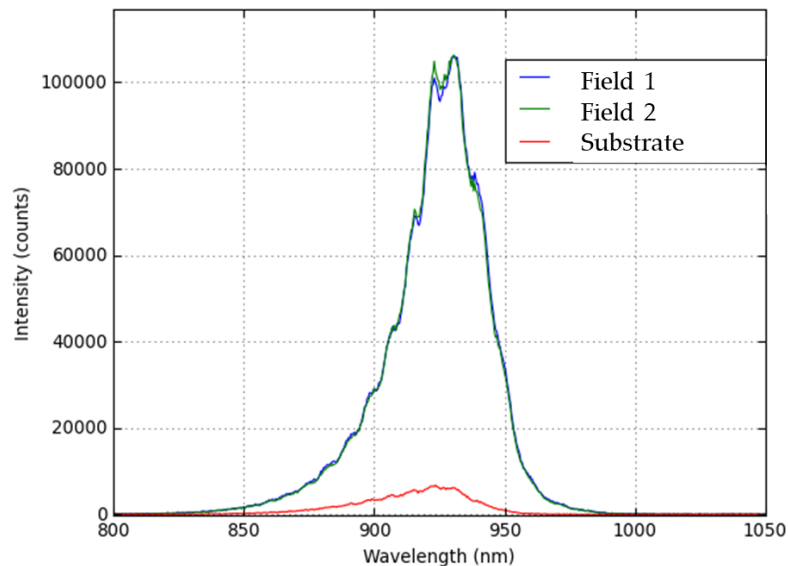

FIGURE 5.6: PL spectrum of the 2.5 µm InP NWs in figure 5.1 (sample no. 1). Fields 1 and 2 correspond to two different NW arrays with the exact same structure geometries, and the substrate signal is the PL signal of the substrate with PDMS on top.

The PL is centered close to the bandgap wavelength of InP at room temperature, $\lambda = 922$ nm. The PL spectra of fields 1 and 2 correspond to different NW arrays with the same structure geometries. The spectrum is relatively broad because the sample is analysed at room temperature. A slight oscillation can be seen in the spectra, especially at wavelengths higher than the bandgap wavelength, which is caused by interference from the back-illuminated CCD and is not attributed to the PL signal of the sample. The PL of the NW arrays is much higher than the PL of the substrate, which is expected because the absorption and emission should be enhanced in the NWs.

The PDMS removal of the second sample, with NWs with a length of 7 µm, was successful so the difference between the inverse and normal orientation could become apparent. The PL spectra of this sample are shown in figure 5.7. This plot shows much different behaviour than the previous sample. First of all, the PL signals of

the NWs in both orientations is very low. Note that the substrate signal is similar in strength to the one of the previous sample. As the PL of any of the NW arrays is expected to be at least higher than the substrate, their low signal could be caused by damage to the NWs. Therefore, a power series measurement was performed at room temperature. The result is shown in figure 5.8.
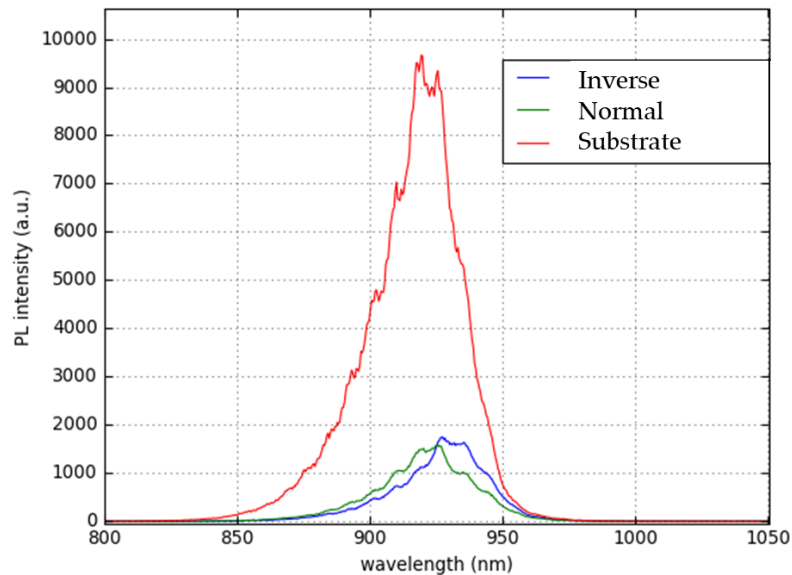
FIGURE 5.7: PL spectrum of the 7 μm InP NWs in figure 5.2 (sample no. 2). The inverse and normal signals correspond to two orientations of the NWs in PDMS on the mirror, and the substrate signal is the PL signal of the substrate with PDMS on top.

FIGURE 5.8: The integrated PL intensity as a function of the excitation laser power for various 7 μm NW samples of InP covered in PDMS (sample no. 2). The integrated intensity is obtained by integrating the PL spectrum over the wavelength range of the CCD for each signal.

In figure 5.8, we have visualized the integrated PL intensity across the entire CCD spectrum as a function of the excitation laser power. Contrary to what we expected, the substrate showed the highest amount of PL, followed by the NW arrays suspended in PDMS, and the two lowest integrated PL intensities were found for the removed NWs in PDMS in normal and inverse orientation respectively. The introduction of a mirror for the normally oriented NWs seems to decrease the overall emission, so the emission of the 7 μm NWs is worse than the substrate. Moreover, both the NWs and the substrate consist of a zincblende crystal structure so their bandgap wavelengths are the same: their separate PL emissions are hard to distinguish. It is therefore instructive to calculate what portion of the incident light the structures in figure 5.8 absorb. We calculate the absorption that occurs solely inside the active region under normally incident laser light with $\lambda = 532$ nm. The absorptions are 86%, 90% and 81% for the NWs normal on substrate, NWs normal on mirror and NWs inverse on mirror respectively. We see that the normally oriented NW absorbs only 4% more of the incident light thanks to the highly reflective mirror. If you take into account the absorption of the substrate underneath the NWs normal on substrate, their total absorption of 86% quickly rises to 96%. Since the absorption and emission are closely related, the differences in absorption between these 7 μm NW setups can explain the order of their integrated PL intensities.

The third sample was analyzed using the optical setup and the integrated PL intensities were again recorded as a function of laser power. The results are shown in figure 5.9. We observe that the overall integrated intensities are generally lower than for the second sample which is attributed to the difference in NW lengths between the samples. Moreover, we see again that the NWs that have been removed from the substrate show lower PL intensities than the NWs that are still attached to the substrate, and the substrate itself. Once more, this is attributed to the fact that the substrate absorbs and emits quite efficiently with respect to the NWs.
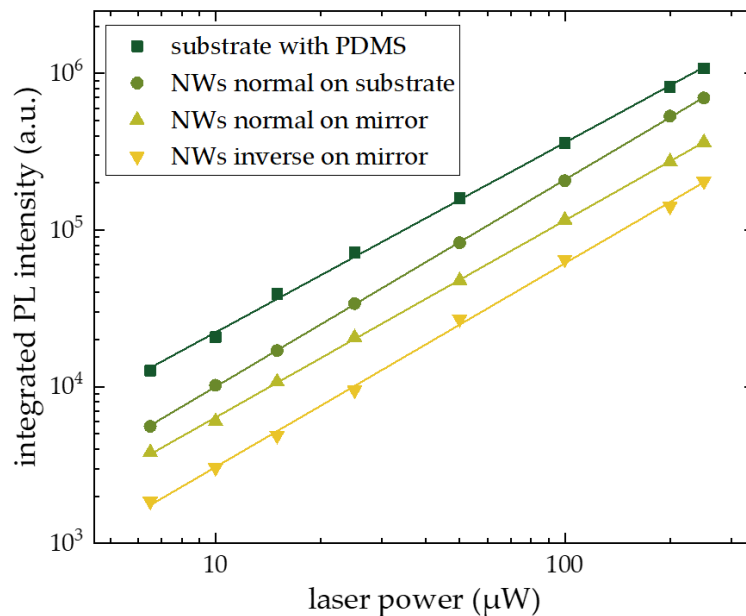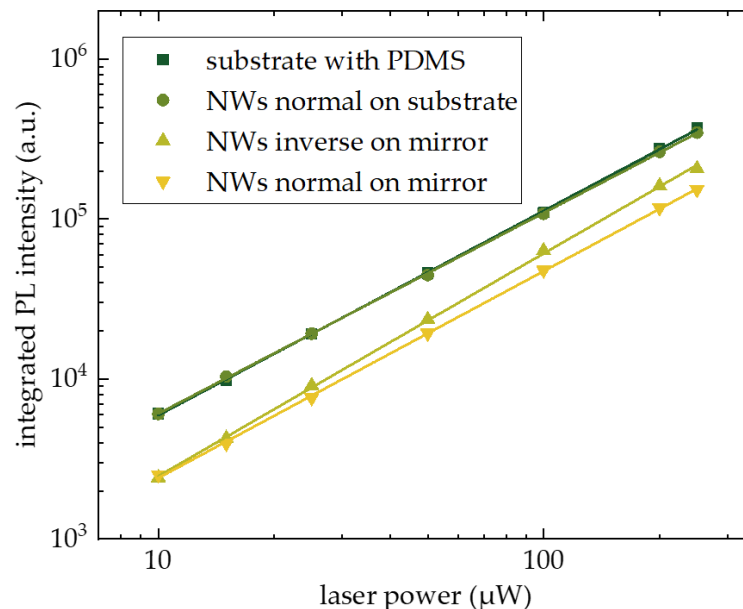

FIGURE 5.9: The integrated PL intensity as a function of the excitation laser power for various 2 μm samples of InP covered in PDMS (sample no. 3). The integrated intensity is obtained by integrating the PL spectrum over the wavelength range of the CCD for each signal.

One distinct difference between the second sample and this third one is the fact that for the third sample, the inverse NWs generally have a higher integrated PL intensity than the normal NWs. This is predicted by results from simulations of the absorption in figure 4.13, where these exact NW geometries with a pitch of 1.2 μm were simulated. The higher absorption of inverse tapered NWs is responsible for a higher PL intensity than the normal tapered NWs. The detailed PL spectra for a single laser power of 200 mW is shown in figure 5.10. In these spectra we see that all of them have a similar shape and center wavelength $\lambda \approx 922$ nm, and we see again the oscillations from the interference of the back-illuminated CCD.
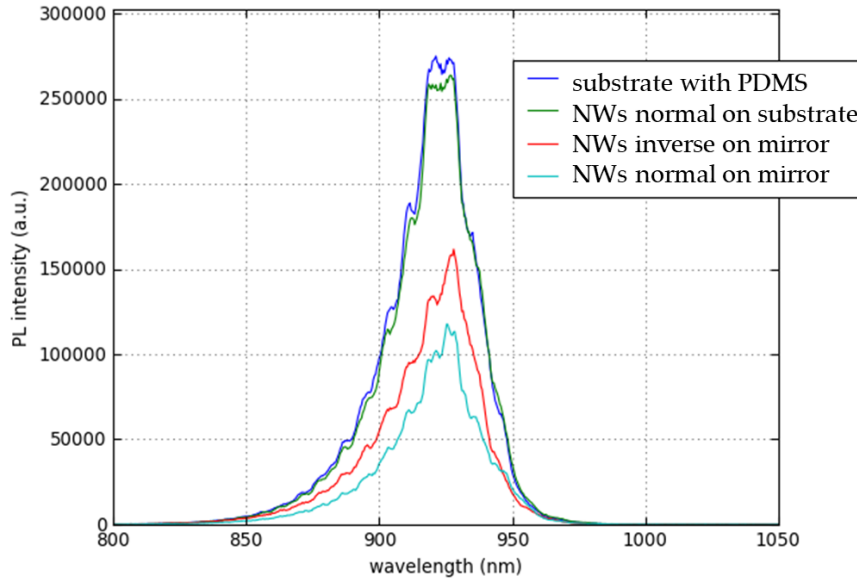

FIGURE 5.10: PL spectra of various configurations of the 2 μm InP NW array sample (sample no. 3) with excitation power 200 mW.

One last feature to verify is the difference between normally and inversely tapered NWs and the role of WGMs in their emission. For the third sample, the power series measurements of the normally and inversely tapered NWs are plotted in figure 5.11. We see that the PL intensity drops as the excitation power decreases for both graphs, but more importantly, we see that they do so with nearly the exact same exponential decay. This conclusion can already be drawn from figure 5.9, where we see that the slopes of the two lines fitting the normal and inverse NW data points are close to each other. Most importantly however, we see no significant difference in the shape of their PL spectra. Whereas other researchers have found very sharp peaks in their PL spectra for inversely tapered NWs,[18,19,85] we do not observe them. This may have several causes.

One may be that during the PDMS removal, the bottom facets of each NW broke from the substrate at a slightly different height, such that the lengths of the NWs embedded in the PDMS are a homogeneous distribution around a certain value. Every slightly different NW length has dramatically different resonant wavelengths, causing them to blur out across the spectrum. Even though the excitation laser spot is small, it will still excite multiple NWs and therefore create a homogeneously distributed PL spectrum. In contrast, Schmitt *et al.* for example excite only a single NW, resulting in very well-defined resonant peaks.[18] Therefore, this research could continue experimentally by investigating the PL of a single tapered NW. This can
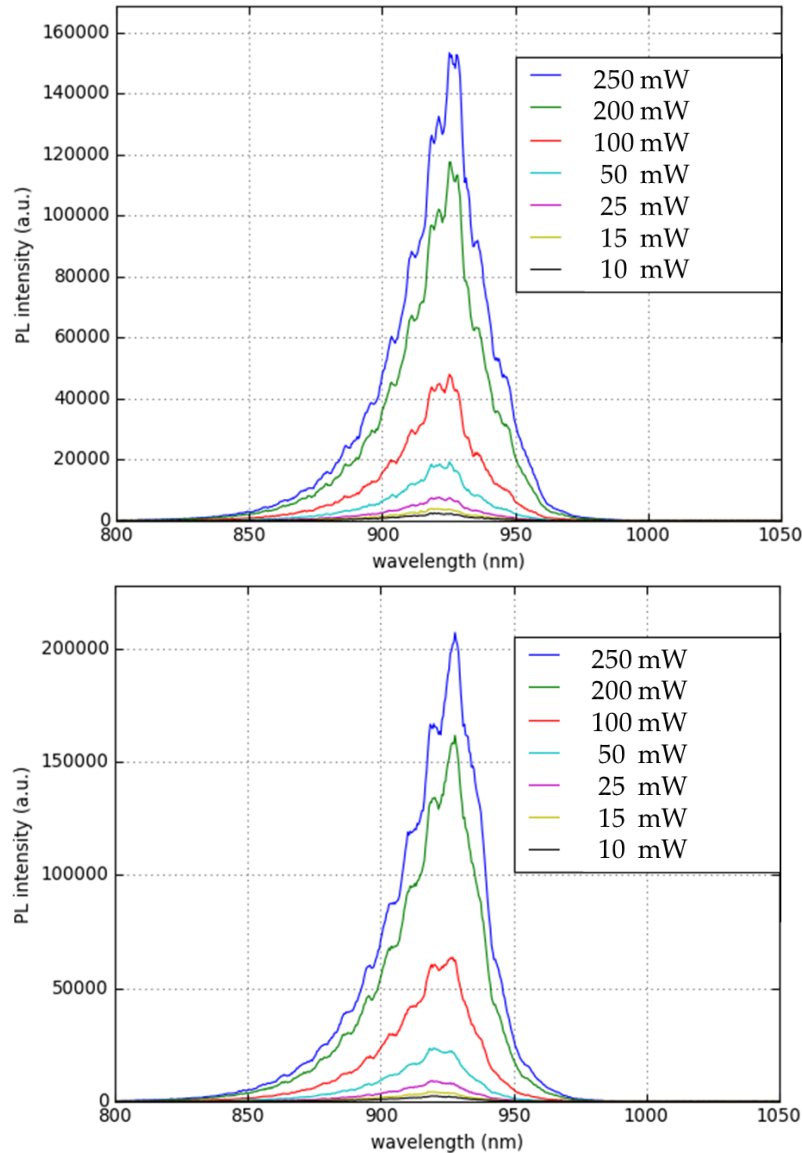
FIGURE 5.11: PL spectra of normally tapered (top) and inversely ta-
pered (bottom) InP NWs with length 2 µm (sample no. 3) as a func-
tion of laser excitation power.

be realized by placing a higher numerical aperture objective in the optical setup
such that the laser spot is focused on a single NW. Another cause for the absence of
resonant peaks could be that the internally radiated photons are emitted predom-
inantly in modes other than WGMs, such as the fundamental mode HE_{11}, that do
not exhibit large Q-factors. We have already seen that the spontaneous emission of
random dipoles favours this mode (figure 4.5). Moreover, the internal radiative effi-
ciency could be too low altogether at room temperature for these structures, and as
a result nonradiative recombinations may be dominant. Therefore, the experimental
research could also continue by examining these tapered NWs at low temperatures.
At low temperatures, the internal radiative efficiency increases and the impact of
modes in structures with a high photon escape probability is more clear.

The impact of the internal radiative efficiency has been intensively studied in a paper by Cavalli *et al.*[133] In particular, the growth during the MOVPE process and the passivation during the PECVD process and the impact of these processes on the final internal radiative effiency are discussed. Although outside the scope of this thesis, the fabrication process has been mentioned once before and could be investigated to best suit the fabricaton of structures that host coupled WGM and FP modes, such as inversely tapered NWs. The top-down etch fabrication process followed by the PDMS removal procedure might leave too much room for error in creating inversely tapered NWs with the purpose of detecting WGM emission. Other methods exist to fabricate them *in situ* on a substrate like Schmitt *et al.*[18] and Seo *et al.*[19] have done. This way, both end facets of the NWs can remain of high quality, unlike the bottom facet of NWs in PDMS that have been removed from the substrate.

Chapter 6

Conclusion

Whispering gallery modes (WGMs) show great promise for the future. Thanks to the sensitivity of their resonant conditions, they are excellent candidates for applications such as biosensing, wavelength tuning, optical coupling and lasing. WGMs exhibit high Q-factors even despite low mode volumes and their resulting enhancement of the spontaneous emission, the Purcell enhancement, ensures their interest in many disciplines. In this thesis, we study the influence of WGMs in nanowire (NW) solar cells. NW solar cells show promise to overcome the principal limits that constrain a solar cell's overall efficiency; most notably, the Shockley-Queisser limit. Using the finite-difference-time-domain (FDTD) method to simulate the photonic behaviour of NW structures, we investigate the significance of WGMs and the effect they have on the external radiative efficiency of the structures.

The primary characteristics of WGMs are determined from simulations of InP NWs. There exist many WGMs in a NW which are named HE_{mn} modes and are characterized by their angular mode number m and radial mode number n. By convention, the fundamental mode of a NW is called the HE_{11} mode. Furthermore, each WGM is characterized by a propagation constant β, which is related to their mode effective refractive index n_{eff}. Simulations of this mode effective index show that it increases towards the refractive index of the InP material if the radius of the NW increases, showcasing enhanced confinement. Consequently, there is a minimal radius where the WGM exists in an unbound mode: a leaky mode. Other researchers have found that WGMs with an effective mode index close to the geometric mean of the material and its environment ($n_{\mathrm{eff}} = 1.9 - 2.3$) are responsible for enhanced spontaneous emission. This conveys the point that the WGMs need not be very well bound within the structure to show enhanced emission.

We show that the spontaneous emission from any WGM from an InP NW is lower than the spontaneous emission from the fundamental HE_{11} mode. The minimal radius for even the lowest order WGMs is large enough for the NWs to host a plethora of other optical modes. Any radiative recombination inside the material results in a photon that will be guided by only one of these modes, and the chances of that mode being a WGM are low if the recombination occurs at a random location. However, we also show that if the recombination occurs strictly at distinct locations inside the NW, the emission from WGMs could be much higher. This is a result of the Purcell enhancement of the WGMs: the high Q-factors and low modal volumes enhance the local density of states (LDOS), which locally increases the availability of band-to-band transitions. If it were possible to attract charge carriers to these areas with a high LDOS to efficiently radiatively recombine there, that would further enlighten the prospects of WGMs, but this has not been shown experimentally yet.

The quality factors of the WGMs are determined using FDTD simulations as well. With the use of a dipole cloud technique, the resonant wavelengths of a range of tapered NW geometries are found. In these tapered NWs, the end facets have different dimensions and therefore show different photonic behaviours. A distinction can be made between positively tapered NWs (normal nanocones, normal NCs) and negatively tapered NWs (inverse NCs). The average Q-factors of inverse NCs is an order of magnitude higher than for normal NCs when they stand on a substrate. This is attributed to large energy losses through the bottom facet to the substrate for normal NCs. This is proven by the fact that the average Q-factors of inverse and normal NCs are essentially equal when they are placed on a mirror, preventing these losses. Furthermore, we find resonances inside the structures with Q-factors nearly 3-4 times larger than these average Q-factors. A further investigation shows that these resonances originate from WGMs at distinct heights inside the inverse NCs that radiate along the vertical direction in a leaky mode. We conclude that a combined mode formation of a high Q-factor WGM and a weakly confined Fabry Perot (FP) mode are responsible for these high Q-factor resonances. To show that the weak confinement of the FP mode does not contribute to the overall Q-factor of these resonances, the Q-factors are calculated and are shown to be independent of the NC heights.

Calculating the photon escape probability in Lumerical is troublesome, since there is no easy tool to perform this calculation accurately and quickly for a periodic structure like a NW or NC array. We make use of the Lorentz reciprocity to lighten up the computational task at hand. The integration over all angles is broken down into increments of 5° and with the method, the emission from the structure into the top and bottom hemispheres is calculated. The photon escape probabilities are then determined to be 38% higher for the inverse NC than for the normal NC configuration, showing that a larger fraction of the total emission of the inverse NC is better directed upwards than the normal NC. This is a step towards reaching the ultimate limit of the solar cell.

In order to experimentally verify our research, we have fabricated three sets of InP NW samples for a characterization of their photoluminescence. These samples are made using a top-down etch approach. One downfall of this method is the fact that inverse NCs can not be fabricated and have to be reconfigured manually. We therefore produce normal NCs and deposit a layer of PDMS on top of the sample. By removing the PDMS layer with the NCs embedded inside, the NCs can be put upside down to obtain inverse NCs. The samples are then characterized using an optical setup to measure their photoluminescence. The production and PDMS removal of the first sample were unsuccessful: the NCs did not experience sufficient support from the PDMS to be removed due to their high bottom diameter and short length. The next sample was therefore designed to secure a higher transfer yield: the NCs were substantially longer and the pitch was increased. A last third sample was fabricated with a reduced NC height, but with various pitches to investigate which ones would still have a significant transfer yield. From these last two samples we obtained fragments of PDMS with embedded NCs that we could further analyze using an optical setup.

The PL signals of these two samples show that the PL signal is strongest from the substrate covered in PDMS – contrary to what we expected. The NC arrays show a respectable PL spectrum that is centered around the bandgap wavelength of InP at room temperature, $\lambda = 922$ nm, and that has a broad wavelength distribution because of this room temperature. From absorption simulations of the two samples,

we find that for the longer NCs the normal configuration absorbs more from incident laser light and that for the shorter NCs the inverse configuration absorbs more. This is verified by the PL measurements, where we find that the emission is larger for longer NCs in the normal configuration and for shorter NCs in the inverse configuration. However, most importantly, we do not see differences in the shapes of the PL signals between normal and inverse configurations. Whereas the theory suggests the availability of high Q-factor resonant coupled WGM and FP modes in inverse NCs, none of such resonant peaks are found in their spectra. This can be attributed to the fact that the PDMS removal procedure may have caused a homogeneous length distribution within the NC array embedded in PDMS, since not every NC will have detached from the substrate in the exact same way. The resulting resonant conditions may be different for every NC, resulting in no distinct strong resonant peak in the PL spectrum. Another explanation is that the fraction of emission from WGMs to the emission from other optical modes could be insufficiently small to be determined from the PL spectrum. The research could have continued with more simulations on the absorption of these structures and new SEM images of the processed samples to verify what exactly happened, but our time had ran out.

In conclusion, we have shown that whispering gallery modes are good candidates for efficient enhancement of the external radiative efficiency of solar cells. They show high Q-factors, local Purcell enhancement for enhanced spontaneous emission and they assist in achieving a higher photon escape probability in inversely tapered NWs. Tapered NW structures that host these modes therefore show promise to experience an enhanced external radiative efficiency. We have not yet conclusively confirmed this behaviour and effects experimentally, but we add that the experimental research could continue by characterizing the behaviour of the modes at low temperatures or by focusing on a single tapered NW. In this thesis we have gained a fundamental understanding into how WGMs behave inside nanowires and we have shown their potent opportunities. This work may therefore be used to propel new research into these modes which will pave the way for their applications in nanophotonic technologies.

Appendix A

FDTD material settings

A.1   The complex dielectric function

In the FDTD solver environment, every structure is assigned the material properties from any of the materials in the already built-in material list or from custom sampled data. The material properties from the material database inside Lumerical have been determined experimentally; most of them come from the "Handbook of Optical Constants of Solids" by Palik,[134] the "CRC Handbook of Chemistry and Physics" by Lide[135] and from the paper "Optical Constants of Noble metals" by Johnson & Christy.[136] Every material contains a list of frequency-dependant complex values of its dielectric constant. The complex dielectric constant $\varepsilon_r(\omega)$ is given by the dielectric function:

$$\varepsilon_r(\omega) = \varepsilon'(\omega) + i\varepsilon''(\omega), \tag{A.1}$$

where $\varepsilon'(\omega)$ and $\varepsilon''(\omega)$ are the real and imaginary part of the electric permittivity respectively. The complex refractive index $n^*(\omega)$ of a material is given by

$$n^*(\omega) = n(\omega) + i\kappa(\omega), \tag{A.2}$$

where $n(\omega)$ and $\kappa(\omega)$ are the real and imaginary part of the refractive index respectively. These quantities are related via

$$n^*(\omega)^2 = \left(n(\omega) + i\kappa(\omega)\right)^2 = \varepsilon_r(\omega) = \varepsilon'(\omega) + i\varepsilon''(\omega). \tag{A.3}$$

We can understand the physical meaning of n and κ by considering an electromagnetic wave travelling through a medium with a complex refractive index n^*. In its most general form, we have a wave travelling in the x-direction with wave vector k_x, angular frequency ω and an electric field strength E_x:

$$E_x = E_{0,x} \cdot \exp\left[i\left(k_x\, x - \omega\, t\right)\right]. \tag{A.4}$$

We now use the definition of the complex wave vector $k^*(\omega)$, which is given by

$$k^* = \frac{2\pi}{\lambda} = \frac{\omega\, n^*}{c} = \frac{\omega\, n}{c} + i\,\frac{\omega\, \kappa}{c}, \tag{A.5}$$

where λ is the wavelength of the electromagnetic wave and c the speed of light in vacuum. Combining equations A.2, A.4 and A.5 yields

$$E_x = E_{0,x} \cdot \exp\left[i\left(\frac{\omega\, n^*}{c}x - \omega\, t\right)\right] = E_{0,x} \cdot \exp\left[i\left(\frac{\omega\,(n+i\kappa)}{c}x - \omega\, t\right)\right]$$

$$E_x = E_{0,x} \cdot \exp\left[\left(\frac{i\,\omega\, n\, x}{c} - \frac{\omega\,\kappa\, x}{c} - i\,\omega\, t\right)\right]. \tag{A.6}$$

The first fraction in the exponent contains the real part of the wave vector, k_x, so we can rearrange to obtain the expression

$$E_x = E_{0,x} \cdot \exp\left[-\frac{\omega\,\kappa\, x}{c}\right]\exp\left[i\,(k_x\, x - \omega\, t)\right]. \tag{A.7}$$

The first exponent is a term decreasing exponentially over a distance x whereas the second exponent is the original expression for a plane wave (equation A.4). Therefore, an electromagnetic wave travelling through a medium with a complex refractive index is whatever it would be for a material with only a real refractive index n times an attenuation factor that decreases the amplitude exponentially as a function of distance x. This attenuation factor tells us about the absorption in the material, whereas the plane wave factor tells us about propagation through the material. From equation A.3 we can isolate and rewrite the real part of the refractive index $n(\omega)$ to

$$n(\omega)^2 = \frac{1}{2}\left(\sqrt{\varepsilon'(\omega)^2 + \varepsilon''(\omega)^2} + \varepsilon'(\omega)\right), \tag{A.8}$$

indicating that the imaginary part of the dielectric function still has an effect on the real refractive index n. However, near the bandgap of InP, $\varepsilon'(\omega)^2 \gg \varepsilon''(\omega)^2$ so that we return to

$$n(\omega)^2 \approx \frac{1}{2}\left(\sqrt{\varepsilon'(\omega)^2} + \varepsilon'(\omega)\right) = \varepsilon'(\omega). \tag{A.9}$$

Therefore, we may omit the imaginary part of the electric permittivity of InP without altering its real valued refractive index $n(\omega)$ significantly. By setting the imaginary part to zero, we neglect the possible re-absorption of emitted light in the emission region.[92, 124] In that way only the underlying diffractive, reflective and interference properties of the nanostructure are investigated. In the weakly absorbing region such an investigation will return a realistic description of the emissive properties.

A.2   The material explorer

The material explorer is a tool built in Lumerical which is used to check the material fits that will be used in the simulation. It plots the values of the real and imaginary parts of the dielectric function provided by the material database and shows the model fit. If the fit for a sampled data material is not good enough, the tolerance, the max coefficient properties and the wavelength range of the source can be edited in the material explorer. Checking the material explorer before running a simulation is

important to see whether the material properties are realistic. The material explorer diagram is visualised in figure A.1.
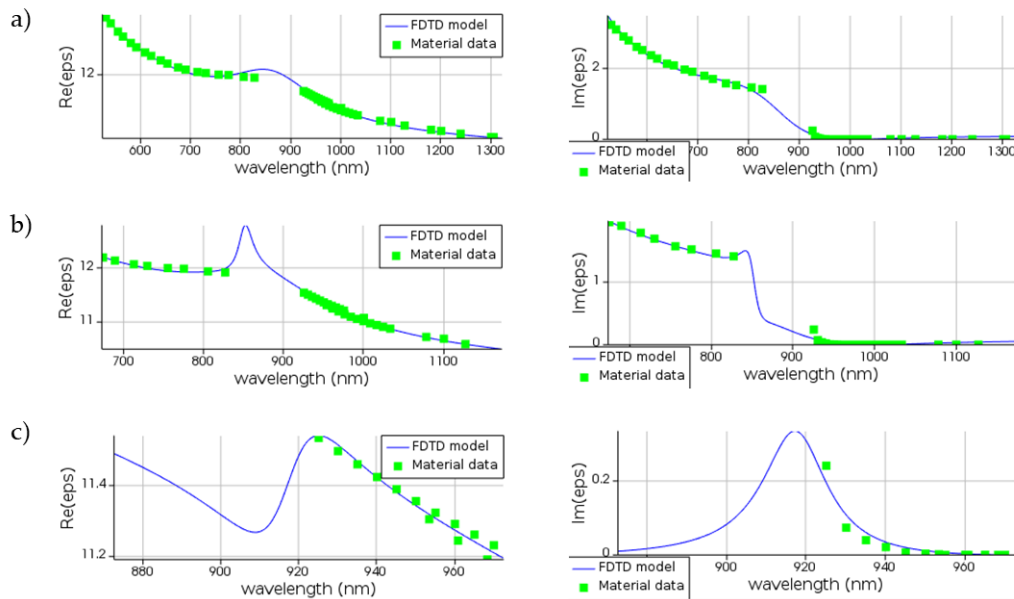

FIGURE A.1: The material explorer plots for InP at a wavelength $\lambda = 922$ nm and bandwidths $\Delta\lambda = 1000$ nm (a), 500 nm (b) and 100 nm (c). Green dots indicate the material database values, the blue line indicates the FDTD model used in the simulation. For shorter bandwidths, the model less accurately covers the material data.

From figure A.1 we can see that for InP, the absorption – which scales with the imaginary part of the dielectric constant $\varepsilon_r(\omega)$ – increases for wavelengths further below the bandgap wavelength $\lambda = 922$ nm, as expected. However, when comparing the three bandwidths, the model fit is considerably worse for the smallest bandwidth (figure A.1(c)) because of missing material data points in the range $\lambda = 825\text{-}925$ nm. Since it is important to have reliable material data in this region, a more accurate data file was acquired. Next to that, a new material data file was generated for reflection and transmission simulations, where absorption is suppressed. The new material explorer plot is visualised in figure A.2.
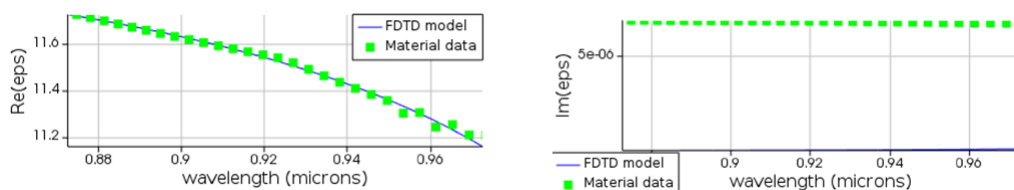

FIGURE A.2: The material explorer plot for the custom material "InP without imaginary part". The full bandwidth of $\Delta\lambda = 100$ nm is correctly modelled and the imaginary part of $\varepsilon_r(\omega)$ is suppressed.

Appendix B

Lorentz reciprocity

B.1 Lorentz reciprocity to obtain P_{top} and P_{bottom}

To model the emission from an unpolarized dipole emitter in an infinite NW array, we cannot simply use a dipole source and periodic boundary conditions in the x-y plane. A dipole inside the unit cell would cause a periodic repetition of this dipole, and the resulting simulation would consider the emission from a periodic array of coherently emitting dipoles.[125] One option to solve this is to model an array with a finite number of NWs and to place a single dipole in the center NW. Then, the number of NWs is increased until the emitted power converges. However, the analysis of a large, finite NW array could become computationally challenging.

The solution we use is based on the Lorentz reciprocity.[137] With this reciprocity, the scattering of an incoming plane wave in the NW array is solved, which can be related to the emission of light from the NW into the direction reverse to the incident direction.[67,124] With plane waves, the periodic (Bloch) boundary conditions can be used for a small unit cell, where the NW pitch is determined by the FDTD region geometry. The only computational challenge remaining is that the plane wave needs to be modelled across all incident polar and azimuth angles for both TE and TM polarisations separately.
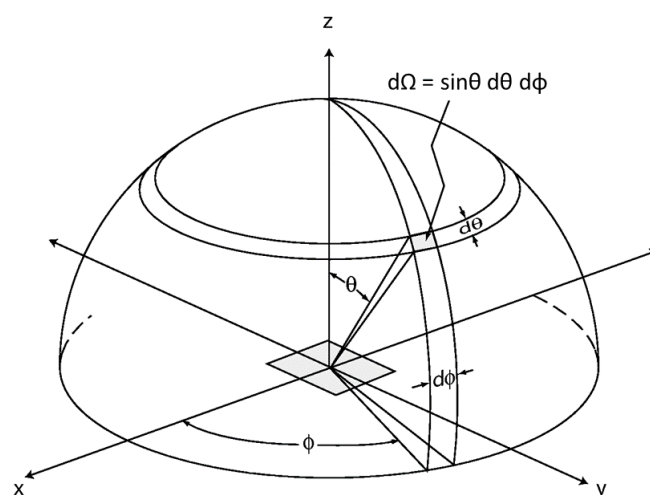

FIGURE B.1: A cartesian coordinate system xyz where the spherical coordinates θ and ϕ describe the solid angle $d\Omega$. Source: EOSC 582 Satellite remote sensing

Below, we consider the calculation for the top hemisphere and TE polarization, but the calculations for the bottom hemisphere and TM polarizations are done likewise. The emitted power $dP_{\text{top},TE}$ into a solid angle $d\Omega$ from the top side of a NW in a direction given by the polar angle θ and azimuth angle ϕ is[124]

$$dP_{\text{top},TE}(r,\lambda,\theta,\phi) = \hbar\,\frac{2\pi c}{\lambda}\,P_{dip}(r,\lambda)\,n(r,\lambda)\,E^2_{enh,\text{top},TE}(r,\lambda,\theta,\phi)\,d\lambda dV d\Omega, \quad \text{(B.1)}$$

where we consider the emitted power from the dipole $P_{dip}(r,\lambda)$ in an infinitesimal wavelength range $d\lambda$ around λ in an infinitesimal volume dV around r. $E^2_{enh,\text{top},TE}$ is the local field enhancement at the location r of the dipole and is given by

$$E^2_{enh,\text{top},TE}(r,\lambda,\theta,\phi) = \frac{|E_{loc,\text{top},TE}(r,\lambda,\theta,\phi)|^2}{|E_{inc,\text{top},TE}(\lambda,\theta,\phi)|^2}. \quad \text{(B.2)}$$

This expression shows the enhancement of emission into specific directions caused by the nanostructure, as a ratio of the electric field intensity $E_{loc,\text{top},TE}$ at the dipole location r and the electric field intensity of the incident plane wave $E_{inc,\text{top},TE}$. The total emitted power from the TE polarized dipole to the top P_{top} is then

$$P_{\text{top}}(r,\lambda) = \int_0^{2\pi} d\phi \int_0^{\pi/2} d\theta \left(dP_{\text{top},TE}(r,\lambda,\theta,\phi) + dP_{\text{top},TM}(r,\lambda,\theta,\phi) \right) \sin(\theta), \quad \text{(B.3)}$$

where $dP_{\text{top},TE}$ and $dP_{\text{top},TM}$ are the TE and TM polarization contributions respectively. Likewise, the total emitted power from the dipole to the bottom P_{bottom} can be calculated. Since the NW arrays in this thesis are always square arrays, they have a rotational symmetry of order 4, which means the azimuth integral need only be integrated from 0 to $\pi/2$:

$$\int_0^{2\pi} d\phi = 4 \cdot \int_0^{\pi/2} d\phi. \quad \text{(B.4)}$$

For calculations of the relative emitted power to the top and bottom of the nanostructures, such as $P_{\text{top}}/(P_{\text{top}} + P_{\text{bottom}})$, equation B.3 is sufficient. For a qualitative analysis however, it is instructive to normalize the values of P_{top} and P_{bottom} to P_{bulk}, which is determined through the same equations assuming $n(r,\lambda) = n_{\text{bulk}}(r,\lambda)$ and $E_{enh} = 1$.[124] P_{bulk} is the power emitted into the top (or bottom) hemisphere from a dipole located in a homogeneous $n = n_{\text{bulk}}$ material. If normalized, a value of 1 for P_{top} corresponds to an equal emitted power to the top as inside an infinitely large bulk sample of n_{bulk}.

B.2 Modeling emission through absorption

To calculate the emitted power to the top P_{top}, we need to determine the electric field distribution E^2_{enh}. This enhanced field distribution can be obtained through the absorption in the structure.[92] Below, we continue the calculations for the top hemisphere and TE polarization, but the calculations for the bottom hemisphere and TM polarization can be done similarly. The absorbed power by a NW from TE polarized incident waves from the top hemisphere $\mathrm{d}P_{abs,\text{top},TE}$ is given by

$$\mathrm{d}P_{abs,\text{top},TE}(\lambda,\theta,\phi) = \mathrm{d}\lambda \int_{V_{NW}} \frac{2\pi c\varepsilon_0}{\lambda} n(r,\lambda)\kappa(r,\lambda)|E_{loc,\text{top},TE}(r,\lambda,\theta,\phi)|^2 \, \mathrm{d}V, \quad \text{(B.5)}$$

where $n(r,\lambda)$ and $\kappa(r,\lambda)$ are the real and imaginary part of the complex refractive index respectively and V_{NW} is the volume of the NW. Note that only (r,λ) where $\kappa(r,\lambda) > 0$ contribute to absorption. Next, the incident power of waves from the top hemisphere is given by

$$\mathrm{d}P_{inc,\text{top},TE}(\lambda,\theta,\phi) = \mathrm{d}\lambda \int_{A_{NW}} \frac{n(\lambda)c\varepsilon_0}{2} \cos(\theta)|E_{inc,\text{top},TE}(\lambda,\theta,\phi)|^2 \, \mathrm{d}A, \quad \text{(B.6)}$$

where A_{NW} is the area of the NW. Now we use the definition of the absorptance A, which is the fraction of incident light that is absorbed by the NW. For TE polarized incident light from the top, the absorptance $A_{\text{top},TE}$ is given by

$$A_{\text{top},TE}(\lambda,\theta,\phi) = \frac{P_{abs,\text{top},TE}(\lambda,\theta,\phi)}{P_{inc,\text{top},TE}(\lambda,\theta,\phi)}. \quad \text{(B.7)}$$

Combining equations B.5–B.7 and assuming we have a periodic nanowire array with a unit cell with a single nanowire volume V_{NW} and a cross-sectional area $A_{\text{cell}} = P^2$, where the NW pitch P is used, we obtain

$$A_{\text{top},TE}(\lambda,\theta,\phi) = \frac{\mathrm{d}\lambda \int_{V_{NW}} \frac{2\pi c\varepsilon_0}{\lambda} n(r,\lambda)\kappa(r,\lambda)|E_{loc,\text{top},TE}(r,\lambda,\theta,\phi)|^2 \, \mathrm{d}V}{\mathrm{d}\lambda \int_{A_{\text{cell}}} \frac{n(\lambda)c\varepsilon_0}{2} \cos(\theta)|E_{inc,\text{top},TE}(\lambda,\theta,\phi)|^2 \, \mathrm{d}A}$$

$$= \frac{4\pi\kappa_{NW}(\lambda) \int_{V_{NW}} \frac{|E_{loc,\text{top},TE}(r,\lambda,\theta,\phi)|^2}{|E_{inc,\text{top},TE}(\lambda,\theta,\phi)|^2} \, \mathrm{d}V}{\lambda \cos(\theta)P^2}$$

$$= \frac{4\pi\kappa_{NW}(\lambda)}{\lambda \cos(\theta)P^2} \int_{V_{NW}} E^2_{enh,\text{top},TE}(r,\lambda,\theta,\phi)\mathrm{d}V. \quad \text{(B.8)}$$

Since $\kappa(r,\lambda) > 0$ only inside the NW volume, the integrals need not be evaluated outside the NW. Assuming a single NW material, $n(r,\lambda) = n(\lambda)$ and $\kappa(r,\lambda) = \kappa(\lambda)$ inside the top integral on the first line. We also use

$$\int_{A_{\text{cell}}} |E_{inc,\text{top},TE}(\lambda,\theta,\phi)|^2 \, \mathrm{d}A = P^2 \int_{V_{NW}} |E_{inc,\text{top},TE}(\lambda,\theta,\phi)|^2 \, \mathrm{d}V, \qquad \text{(B.9)}$$

since the value of E_{inc} is determined at any point in the NW volume. From equation B.8 we find that

$$\int_{V_{NW}} E_{enh,\text{top},TE}^2(r,\lambda,\theta,\phi)\mathrm{d}V = \frac{A_{\text{top},TE}(\lambda,\theta,\phi)\,\lambda\cos(\theta)P^2}{4\pi\,\kappa_{NW}(\lambda)}. \qquad \text{(B.10)}$$

This is the volume integral required we are interested in: substituting equation B.10 into equations B.1 and then B.3 yields

$$P_{\text{top}}(r,\lambda) = C \int_0^{\pi/2} \mathrm{d}\phi \int_0^{\pi/2} \sin(\theta)\cos(\theta)\mathrm{d}\theta \left(A_{\text{top},TE}(r,\lambda,\theta,\phi) + A_{\text{top},TM}(r,\lambda,\theta,\phi)\right),$$

$$\text{with the constant } C = \frac{2\hbar c P_{dip}(r,\lambda)n(r,\lambda)P^2}{\kappa(\lambda)}\mathrm{d}\lambda. \qquad \text{(B.11)}$$

This way, we can calculate the absorption of the periodic NW array for incident waves across a range of incidence direction and polarization, and obtain the power emitted by a dipole at any specified location to the top and bottom.

The assumption is made that $\kappa(\lambda) > 0$ for the NW structure, since otherwise there would be no absorption. However, as explained in Appendix A, for most simulations a non-absorbing material is used based on InP with a suppressed imaginary part. To use the technique described in this Appendix, we consulted research by Anttu *et al.*,[92] who found converging values of P_{top} and P_{bottom} for $\kappa(\lambda) < 10^{-3}$. They notice that this imaginary part should not be decreased indefinitely, since the limited numerical precision of the simulations may not be able to distinguish low absorption values from zero. However, in the FDTD simulations in this report, floating point numbers with an accuracy up to 16 digits are used for data collection, so a value of $\kappa(\lambda) \approx 10^{-8}$ is permitted (which permits the use of the InP material model with suppressed κ, see figure A.2).

Bibliography

[1] M. A. Green, "Commercial progress and challenges for photovoltaics," *Nature Energy*, vol. 1, no. 1, pp. 1–4, 2016.

[2] A. Jäger-Waldau, "Snapshot of photovoltaics—February 2020," *Energies*, vol. 13, no. 4, p. 930, 2020.

[3] M. Kochańczyk, F. Grabowski, and T. Lipniacki, "Super-spreading events initiated the exponential growth phase of COVID-19 with R0 higher than initially estimated," *Royal Society Open Science*, vol. 7, no. 9, p. 200786, 2020.

[4] S. Bhattacharya and S. John, "Beyond 30% conversion efficiency in silicon solar cells: A numerical demonstration," *Scientific Reports*, vol. 9, 08 2019.

[5] R. Cariou *et al.*, "III–V-on-silicon solar cells reaching 33% photoconversion efficiency in two-terminal configuration," *Nature Energy*, vol. 3, no. 4, pp. 326–333, 2018.

[6] A. Polman *et al.*, "Photovoltaic materials: Present efficiencies and future challenges," *Science*, vol. 352, pp. 1–10, Apr. 2016.

[7] D. Bartesaghi *et al.*, "Competition between recombination and extraction of free charges determines the fill factor of organic solar cells," *Nature Communications*, vol. 6, May 2015.

[8] E. C. Garnett *et al.*, "Nanowire solar cells," *Annual Review of Materials Research*, vol. 41, pp. 269–295, 2011.

[9] J. Haverkort *et al.*, "Fundamentals of the nanowire solar cell: optimization of the open circuit voltage," *Applied Physics Reviews*, vol. 5, Sept. 2018.

[10] W. Shockley and H. J. Queisser, "Detailed balance limit of efficiency of p-n junction solar cells," *Journal of Applied Physics*, vol. 32, no. 3, pp. 510–519, 1961.

[11] L. Tsakalakos *et al.*, "Silicon nanowire solar cells," *Applied Physics Letters*, vol. 91, no. 23, p. 233117, 2007.

[12] M. Brongersma, Y. Cui, and S. Fan, "Light management for photovoltaics using high-index nanostructures," *Nature materials*, vol. 13, pp. 451–60, 04 2014.

[13] S. Yang, Y. Wang, and H. Sun, "Advances and prospects for whispering gallery mode microcavities," *Advanced Optical Materials*, vol. 3, no. 9, pp. 1136–1162, 2015.

[14] A. Hochbaum and P. Yang, "Semiconductor nanowires for energy conversion," *Chemical Reviews*, vol. 110, pp. 527–46, 10 2009.

[15] A. P. Alivisatos, "Semiconductor clusters, nanocrystals, and quantum dots," *Science*, vol. 271, no. 5251, pp. 933–937, 1996.

[16] M. Law, J. Goldberger, and P. Yang, "Semiconductor nanowires and nanotubes," *Annual Review of Materials Research*, vol. 34, no. 1, pp. 83–122, 2004.

[17] L. Rayleigh, "CXII. The problem of the whispering gallery," *The London, Edinburgh, and Dublin Philosophical Magazine and Journal of Science*, vol. 20, no. 120, pp. 1001–1004, 1910.

[18] S. W. Schmitt *et al.*, "Observation of strongly enhanced photoluminescence from inverted cone-shaped silicon nanostructures," *Scientific Reports*, vol. 5, no. 1, p. 17089, 2015.

[19] M. Seo *et al.*, "Weakly tapered silicon nanopillar resonators with spatially well-separated whispering gallery modes for Si-based lasers," *ACS Applied Nano Materials*, vol. 2, no. 8, pp. 4852–4858, 2019.

[20] A. Standing *et al.*, "High yield transfer of ordered nanowire arrays into transparent flexible polymer films," *Nanotechnology*, vol. 23, no. 49, pp. 1–6, 2012.

[21] K. T. Fountaine *et al.*, "Near-unity unselective absorption in sparse inp nanowire arrays," *ACS Photonics*, vol. 3, no. 10, pp. 1826–1832, 2016.

[22] N. Anttu *et al.*, "Absorption of light in InP nanowire arrays," *Nano Research*, vol. 7, pp. 816–823, 06 2014.

[23] J. M. Spurgeon *et al.*, "Repeated epitaxial growth and transfer of arrays of patterned, vertically aligned, crystalline Si wires from a single Si(111) substrate," *Applied Physics Letters*, vol. 93, no. 3, p. 032112, 2008.

[24] A. Cavalli *et al.*, "Nanowire polymer transfer for enhanced solar cell performance and lower cost," *Nano-Structures & Nano-Objects*, vol. 16, pp. 59 – 62, 2018.

[25] M. Reimer *et al.*, "Bright single-photon sources in bottom-up tailored NWs," *Nature Communications*, vol. 3, p. 737, 03 2012.

[26] T. Soga, "Chapter 1 - fundamentals of solar cell," in *Nanostructured Materials for Solar Energy Conversion* (T. Soga, ed.), pp. 3 – 43, Amsterdam: Elsevier, 2006.

[27] A. Thomason, "A traditional solar cell." https://www.researchgate.net/figure/ Fig11-A-traditional-solar-cell-source-c-aaron-thomason-srpnet.com_fig5_320179480. Accessed: 2021-04-19.

[28] T. Fuyuki *et al.*, "Photographic surveying of minority carrier diffusion length in polycrystalline silicon solar cells by electroluminescence," *Applied Physics Letters*, vol. 86, no. 26, p. 262108, 2005.

[29] O. D. Miller *et al.*, "Strong internal and external luminescence as solar cells approach the Shockley-Queisser limit," *IEEE Journal of Photovoltaics*, vol. 2, 7 2012.

[30] H. C. Casey, B. I. Miller, and E. Pinkas, "Variation of minority-carrier diffusion length with carrier concentration in GaAs liquid-phase epitaxial layers," *Journal of Applied Physics*, vol. 44, no. 3, pp. 1281–1287, 1973.

[31] A. Darbandi and S. P. Watkins, "Measurement of minority carrier diffusion lengths in GaAs nanowires by a nanoprobe technique," *Journal of Applied Physics*, vol. 120, no. 1, p. 014301, 2016.

[32] U. Stutenbaeumer and E. Lewetegn, "Comparison of minority carrier diffusion length measurements in silicon solar cells by the photo-induced open-circuit voltage decay (OCVD) with different excitation sources," *Renewable Energy*, vol. 20, no. 1, pp. 65–74, 2000.

[33] C. Kittel, *Introduction to Solid State Physics*. Wiley, 8 ed., 2004.

[34] R. N. Hall, "Recombination processes in semiconductors," *Proceedings of the IEE-Part B: Electronic and Communication Engineering*, vol. 106, no. 17S, pp. 923–931, 1959.

[35] D. Neamen, *Semiconductor Physics And Devices*. USA: McGraw-Hill, Inc., 3 ed., 2002.

[36] M. A. Green, *Solar cells: operating principles, technology and system applications*. University of New South Wales Kensington, N.S.W, 1986.

[37] M. Green *et al.*, "Solar cell efficiency tables (version 57)," *Progress in Photovoltaics: Research and Applications*, vol. 29, no. 1, pp. 3–15, 2021.

[38] W. Shockley, "The theory of p-n junctions in semiconductors and p-n junction transistors," *The Bell System Technical Journal*, vol. 28, no. 3, pp. 435–489, 1949.

[39] H. Bayhan and M. Bayhan, "A simple approach to determine the solar cell diode ideality factor under illumination," *Solar Energy*, vol. 85, no. 5, pp. 769 – 775, 2011.

[40] A. Nussbaum, "Generation-recombination characteristic behavior of silicon diodes," *Physica Status Solidi (a)*, vol. 19, no. 2, pp. 441–450, 1973.

[41] E. Faulkner and M. Buckingham, "Modified theory of the current/voltage relation in silicon p–n junctions," *Electronics Letters*, vol. 4, pp. 359–360(1), August 1968.

[42] R. N. Hall, "Power rectifiers and transistors," *Proceedings of the IRE*, vol. 40, no. 11, pp. 1512–1518, 1952.

[43] C. Sah *et al.*, "Carrier generation and recombination in p-n junctions and p-n junction characteristics," *Proceedings of the IRE*, vol. 45, no. 9, pp. 1228–1243, 1957.

[44] R. N. Hall, "Silicon photovoltaic cells," *Solid-State Electronics*, vol. 24, no. 7, pp. 595 – 616, 1981.

[45] K. Ukoima and E. Agwu, "Three-diode model and simulation of photovoltaic (PV) cells," vol. 5, pp. 108–116, 06 2019.

[46] V. Khanna *et al.*, "A three diode model for industrial solar cells and estimation of solar cell parameters using PSO algorithm," *Renewable Energy*, vol. 78, pp. 105–113, 2015.

[47] O. S. Elazab *et al.*, "Parameter estimation of three diode photovoltaic model using grasshopper optimization algorithm," *Energies*, vol. 13, no. 2, p. 497, 2020.

[48] A. Harrag and Y. Daili, "Three-diodes PV model parameters extraction using PSO algorithm," *Rev. Energies Renouvelables*, vol. 22, no. 1, pp. 85–91, 2019.

[49] J. Kennedy and R. Eberhart, "Particle swarm optimization," in *Proceedings of ICNN'95 - International Conference on Neural Networks*, vol. 4, pp. 1942–1948 vol.4, 1995.

[50] H. Queisser, "Detailed balance limit for solar cell efficiency," *Materials Science and Engineering: B*, vol. 159, pp. 322–328, Mar. 2009.

[51] L. C. Hirst and N. J. Ekins-Daukes, "Fundamental losses in solar cells," *Progress in Photovoltaics: Research and Applications*, vol. 19, no. 3, pp. 286–293, 2011.

[52] T. Markvart, "The thermodynamics of optical étendue," *Journal of Optics A: Pure and Applied Optics*, vol. 10, p. 015008, Dec. 2007.

[53] U. Rau, U. Paetzold, and T. Kirchartz, "Thermodynamics of light management in photovoltaic devices," *Phys. Rev. B*, vol. 90, p. 035211, 07 2014.

[54] R. T. Ross, "Some thermodynamics of photochemical systems," *The Journal of Chemical Physics*, vol. 46, pp. 4590–4593, June 1967.

[55] V. Ganapati, M. A. Steiner, and E. Yablonovitch, "The voltage boost enabled by luminescence extraction in solar cells," *IEEE Journal of Photovoltaics*, vol. 6, 7 2016.

[56] Y. Cui *et al.*, "Boosting solar cell photovoltage via nanophotonic engineering," *Nano Letters*, vol. 16, pp. 6467–6471, Oct. 2016.

[57] O. D. Miller and E. Yablonovitch, "Photon extraction: the key physics for approaching solar cell efficiency limits," in *Active Photonic Materials V* (G. S. Subramania and S. Foteinopoulou, eds.), vol. 8808, pp. 18 – 27, International Society for Optics and Photonics, SPIE, 2013.

[58] G. Kästner and U. Gösele, "Stress and dislocations at cross-sectional heterojunctions in a cylindrical nanowire," *Philosophical Magazine*, vol. 84, no. 35, pp. 3803–3824, 2004.

[59] M. T. Borgström *et al.*, "Nanowires with promise for photovoltaics," *IEEE Journal of Selected Topics in Quantum Electronics*, vol. 17, no. 4, pp. 1050–1061, 2011.

[60] L. Francaviglia *et al.*, "Anisotropic-strain-induced band gap engineering in nanowire-based quantum dots," *Nano Letters*, vol. 18, no. 4, pp. 2393–2401, 2018.

[61] L. Balaghi *et al.*, "Widely tunable GaAs bandgap via strain engineering in core/shell nanowires with large lattice mismatch," *Nature Communications*, vol. 10, p. 2793, 06 2019.

[62] L. Gagliano *et al.*, "Twofold origin of strain-induced bending in core–shell nanowires: the GaP/InGaP case," *Nanotechnology*, vol. 29, p. 315703, May 2018.

[63] R. Paniagua-Domínguez, G. Grzela, J. G. Rivas, and J. A. Sánchez-Gil, "Enhanced and directional emission of semiconductor nanowires tailored through leaky/guided modes," *Nanoscale*, vol. 5, pp. 10582–10590, 2013.

[64] C. E. Hofmann *et al.*, "Enhancing the radiative rate in III-V semiconductor plasmonic coreshell nanowire resonators," *Nano Letters*, vol. 11, no. 2, pp. 372–376, 2011.

[65] Z. Fan *et al.*, "Ordered arrays of dual-diameter nanopillars for maximized optical absorption," *Nano Letters*, vol. 10, no. 10, pp. 3823–3827, 2010.

[66] O. L. Muskens *et al.*, "Design of light scattering in nanowire materials for photovoltaic applications," *Nano Letters*, vol. 8, no. 9, pp. 2638–2642, 2008.

[67] S. Diedenhofen *et al.*, "Strong geometrical dependence of the absorption of light in arrays of semiconductor nanowires," *ACS Nano*, vol. 5, no. 3, pp. 2316–2323, 2011.

[68] B. M. Kayes *et al.*, "27.6% conversion efficiency, a new record for single-junction solar cells under 1 sun illumination," in *2011 37th IEEE Photovoltaic Specialists Conference*, pp. 04–08, 2011.

[69] K. Yoshikawa *et al.*, "Silicon heterojunction solar cell with interdigitated back contacts for a photoconversion efficiency over 26%," *Nature Energy*, vol. 2, p. 17032, 03 2017.

[70] M. Wanlass, "Systems and methods for advanced ultra-high-performance InP solar cells," 3 2017.

[71] D. van Dam *et al.*, "High-efficiency nanowire solar cells with omnidirectionally enhanced absorption due to self-aligned indium–tin–oxide mie scatterers," *ACS Nano*, vol. 10, no. 12, pp. 11414–11419, 2016.

[72] J. Krepelka, "Maximally flat antireflection coatings," *Jemná Mechanika A Optika*, vol. 37, pp. 53–56, 1992.

[73] I. Moreno, J. J. Araiza, and M. Avendano-Alejo, "Thin-film spatial filters," *Opt. Lett.*, vol. 30, pp. 914–916, Apr 2005.

[74] K.-C. Kim, "Effective graded refractive-index anti-reflection coating for high refractive-index polymer ophthalmic lenses," *Materials Letters*, vol. 160, pp. 158–161, 2015.

[75] J. Zhu *et al.*, "Optical absorption enhancement in amorphous silicon nanowire and nanocone arrays," *Nano Letters*, vol. 9, no. 1, pp. 279–282, 2009.

[76] Y. Tang *et al.*, "Vertically aligned p-type single-crystalline GaN nanorod arrays on n-type Si for heterojunction photovoltaic cells," *Nano Letters*, vol. 8, pp. 4191–4195, Dec. 2008.

[77] D. Callahan, J. Munday, and H. Atwater, "Solar cell light trapping beyond the ray optic limit," *Nano letters*, vol. 12, pp. 214–8, 12 2011.

[78] E. Garnett and P. Yang, "Light trapping in silicon nanowire solar cells," *Nano Letters*, vol. 10, no. 3, pp. 1082–1087, 2010.

[79] E. Yablonovitch, "Statistical ray optics," *J. Opt. Soc. Am.*, vol. 72, pp. 899–907, Jul 1982.

[80] L. Cao *et al.*, "Engineering light absorption in semiconductor nanowire devices," *Nature materials*, vol. 8, pp. 643–7, 09 2009.

[81] L. Cao *et al.*, "Semiconductor nanowire optical antenna solar absorbers," *Nano Letters*, vol. 10, no. 2, pp. 439–445, 2010.

[82] C. F. Bohren and D. R. Huffman, *Absorption and scattering of light by small particles*. John Wiley & Sons, 2008.

[83] T. Wriedt, *Generalized multipole techniques for electromagnetic and light scattering*. Elsevier, 1999.

[84] A. B. Evlyukhin, C. Reinhardt, and B. N. Chichkov, "Multipole light scattering by nonspherical nanoparticles in the discrete dipole approximation," *Physical Review B*, vol. 84, no. 23, p. 235429, 2011.

[85] I. Friedler *et al.*, "Solid-state single photon sources: the nanowire antenna," *Opt. Express*, vol. 17, pp. 2095–2110, Feb 2009.

[86] C. F. Bohren, "How can a particle absorb more than the light incident on it?," *American Journal of Physics*, vol. 51, no. 4, pp. 323–327, 1983.

[87] P. Krogstrup *et al.*, "Single-nanowire solar cells beyond the Shockley–Queisser limit," *Nature Photonics*, vol. 7, no. 4, pp. 306–310, 2013.

[88] T. Kirchartz *et al.*, "Impact of photon recycling on the open-circuit voltage of metal halide perovskite solar cells," *ACS energy letters*, vol. 1, no. 4, pp. 731–739, 2016.

[89] N. Gregersen *et al.*, "Controlling the emission profile of a nanowire with a conical taper," *Opt. Lett.*, vol. 33, pp. 1693–1695, Aug 2008.

[90] R. Daendliker, "Concept of modes in optics and photonics," in *Sixth International Conference on Education and Training in Optics and Photonics* (J. J. Sanchez-Mondragon, ed.), vol. 3831 of *Society of Photo-Optical Instrumentation Engineers (SPIE) Conference Series*, pp. 193–198, June 2000.

[91] A. W. Snyder and J. Love, *Optical waveguide theory*. Springer Science & Business Media, 2012.

[92] N. Anttu, "Modifying the emission of light from a semiconductor nanowire array," *Journal of Applied Physics*, vol. 120, no. 4, p. 043108, 2016.

[93] A. Ghatak, "Leaky modes in optical waveguides," *Optical and Quantum Electronics*, vol. 17, pp. 311–321, 1985.

[94] J. Hu and C. R. Menyuk, "Understanding leaky modes: slab waveguide revisited," *Adv. Opt. Photon.*, vol. 1, pp. 58–106, Jan 2009.

[95] V. S. Ilchenko and A. B. Matsko, "Optical resonators with whispering-gallery modes-part II: applications," *IEEE Journal of Selected Topics in Quantum Electronics*, vol. 12, no. 1, pp. 15–32, 2006.

[96] A. N. Oraevsky, "Whispering-gallery waves," *Quantum Electronics*, vol. 32, pp. 377–400, may 2002.

[97] E. M. Purcell, "Proceedings of the American Physical Society: Spontaneous emission probabilities at radio frequencies," *Phys. Rev.*, vol. 69, pp. 674–674, Jun 1946.

[98] K. J. Vahala, "Optical microcavities," *Nature*, vol. 424, no. 6950, pp. 839–846, 2003.

[99] E. A. Muljarov and W. Langbein, "Exact mode volume and purcell factor of open optical systems," *Phys. Rev. B*, vol. 94, p. 235438, Dec 2016.

[100] U. Jahn *et al.*, "Influence of localization on the carrier diffusion in GaAs(Al,Ga)As and (In,Ga)(As,N)GaAs quantum wells: A comparative study," *Phys. Rev. B*, vol. 73, p. 125303, Mar 2006.

[101] Y. Ding *et al.*, "Nanowires/microfiber hybrid structure multicolor laser," *Opt. Express*, vol. 17, pp. 21813–21818, Nov 2009.

[102] M. Saito *et al.*, "Tunable whispering gallery mode emission from a microdroplet in elastomer," *Opt. Express*, vol. 16, pp. 11915–11919, Aug 2008.

[103] V. D. Ta, R. Chen, and H. D. Sun, "Tuning whispering gallery mode lasing from self-assembled polymer droplets," *Scientific reports*, vol. 3, p. 1362, 2013.

[104] R. Chen *et al.*, "Bending-induced bidirectional tuning of whispering gallery mode lasing from flexible polymer fibers," *ACS Photonics*, vol. 1, no. 1, pp. 11–16, 2014.

[105] S. K. Y. Tang *et al.*, "Continuously tunable microdroplet-laser in a microfluidic channel," *Opt. Express*, vol. 19, pp. 2204–2215, Jan 2011.

[106] M. R. Foreman, J. D. Swaim, and F. Vollmer, "Whispering gallery mode sensors," *Adv. Opt. Photon.*, vol. 7, pp. 168–240, Jun 2015.

[107] F. Vollmer and S. Arnold, "Whispering-gallery-mode biosensing: Label-free detection down to single molecules," *Nature methods*, vol. 5, pp. 591–6, 08 2008.

[108] C. Grivas *et al.*, "Single-mode tunable laser emission in the single-exciton regime from colloidal nanocrystals," *Nature Communications*, vol. 4, no. 2376, pp. 1–9, 2013.

[109] L. Cai, J. Pan, and S. Hu, "Overview of the coupling methods used in whispering gallery mode resonator systems for sensing," *Optics and Lasers in Engineering*, vol. 127, p. 105968, 2020.

[110] C. C. Lam, P. T. Leung, and K. Young, "Explicit asymptotic formulas for the positions, widths, and strengths of resonances in mie scattering," *J. Opt. Soc. Am. B*, vol. 9, pp. 1585–1592, Sep 1992.

[111] W. van Roosbroeck and W. Shockley, "Photon-radiative recombination of electrons and holes in germanium," *Phys. Rev.*, vol. 94, pp. 1558–1560, Jun 1954.

[112] C. Santori *et al.*, "Indistinguishable photons from a single-photon device," in *Conference on Lasers and Electro-Optics/Quantum Electronics and Laser Science Conference*, p. QME3, Optical Society of America, 2003.

[113] E. K. Lau *et al.*, "Enhanced modulation bandwidth of nanocavity light emitting devices," *Optics Express*, vol. 17, no. 10, pp. 7790–7799, 2009.

[114] K. Seo *et al.*, "Multicolored vertical silicon nanowires," *Nano Letters*, vol. 11, no. 4, pp. 1851–1856, 2011.

[115] S. W. Schmitt, K. Schwarzburg, and C. Dubourdieu, "Direct measurement and analytical description of the mode alignment in inversely tapered silicon nanoresonators," *Scientific reports*, vol. 9, no. 1, pp. 1–7, 2019.

[116] S. W. Schmitt *et al.*, "All-silicon polarized light source based on electrically excited whispering gallery modes in inversely tapered photonic resonators," *APL Materials*, vol. 8, no. 6, p. 061110, 2020.

[117] N. Anttu, "Geometrical optics, electrostatics, and nanophotonic resonances in absorbing nanowire arrays," *Opt. Lett.*, vol. 38, pp. 730–732, Mar 2013.

[118] D. M. Sullivan, *Electromagnetic simulation using the FDTD method.* John Wiley & Sons, 2013.

[119] J. B. Schneider, "Understanding the finite-difference time-domain method," *School of electrical engineering and computer science Washington State University*, vol. 181, 2010.

[120] A. Taflove and S. C. Hagness, "Computational electromagnetics: the finite-difference time-domain method," *Artech House*, vol. 3, 2000.

[121] K. Yee, "Numerical solution of initial boundary value problems involving Maxwells̀ equations in isotropic media," *IEEE Transactions on Antennas and Propagation*, vol. 14, no. 3, pp. 302–307, 1966.

[122] K. Korzun *et al.*, "Nanowire solar cell above the radiative limit," *Advanced Optical Materials*, vol. 9, no. 2, p. 2001636, 2021.

[123] S. Spillane, T. Kippenberg, O. Painter, and K. Vahala, "Ideality in a fiber-taper-coupled microresonator system for application to cavity quantum electrodynamics," *Physical review letters*, vol. 91, no. 4, p. 043902, 2003.

[124] N. Anttu, "Connection between modeled blackbody radiation and dipole emission in large-area nanostructures," *Opt. Lett.*, vol. 41, pp. 1494–1497, Apr 2016.

[125] C. Xu, R. Biswas, and K.-M. Ho, "Enhanced light emission in semiconductor nanowire arrays," *Optics Communications*, vol. 287, pp. 250–253, 2013.

[126] D. S. Engstrom and Y.-A. Soh, "Controlling the silicon nanowire tapering angle in dense arrays of silicon nanowires using deep reactive ion etching," *Journal of Vacuum Science & Technology B*, vol. 31, no. 2, p. 021806, 2013.

[127] M. Liu, J. Sun, and Q. Chen, "Influences of heating temperature on mechanical properties of polydimethylsiloxane," *Sensors and Actuators A: Physical*, vol. 151, no. 1, pp. 42 – 45, 2009.

[128] K. Namassivayane *et al.*, "Characterization of silicon nanowire by use of full-vectorial finite element method," *Applied optics*, vol. 49, pp. 3173–81, 06 2010.

[129] J. M. Gérard *et al.*, "Enhanced spontaneous emission by quantum boxes in a monolithic optical microcavity," *Phys. Rev. Lett.*, vol. 81, pp. 1110–1113, Aug 1998.

[130] T. Lund-Hansen *et al.*, "Experimental realization of highly efficient broadband coupling of single quantum dots to a photonic crystal waveguide," *Phys. Rev. Lett.*, vol. 101, p. 113903, Sep 2008.

[131] K.-H. Brenner, "Aspects for calculating local absorption with the rigorous coupled-wave method," *Optics express*, vol. 18, no. 10, pp. 10369–10376, 2010.

[132] O. Semyonov, A. Subashiev, Z. Chen, and S. Luryi, "Radiation efficiency of heavily doped bulk n-inp semiconductor," *Journal of Applied Physics*, vol. 108, no. 1, p. 013101, 2010.

[133] A. Cavalli, J. E. Haverkort, and E. P. Bakkers, "Exploring the internal radiative efficiency of selective area nanowires," *Journal of Nanomaterials*, vol. 2019, 2019.

[134] E. D. Palik, *Handbook of Optical Constants of Solids*, vol. 1-3. Academic press, 1998.

[135] D. R. Lide, *CRC Handbook of Chemistry and Physics*, vol. 85. CRC press, 2004.

[136] P. B. Johnson and R. W. Christy, "Optical constants of the noble metals," *Physical review B*, vol. 6, no. 12, p. 4370, 1972.

[137] J. Mertz, "Radiative absorption, fluorescence, and scattering of a classical dipole near a lossless interface: a unified description," *J. Opt. Soc. Am. B*, vol. 17, pp. 1906–1913, Nov 2000.